

2007

## Characterization of interfacial interactions between nanoclay and polymer matrix

Karl Dietrich Amo  
*San Jose State University*

Follow this and additional works at: [https://scholarworks.sjsu.edu/etd\\_theses](https://scholarworks.sjsu.edu/etd_theses)

---

### Recommended Citation

Amo, Karl Dietrich, "Characterization of interfacial interactions between nanoclay and polymer matrix" (2007). *Master's Theses*. 3458.  
DOI: <https://doi.org/10.31979/etd.mxj9-9z8m>  
[https://scholarworks.sjsu.edu/etd\\_theses/3458](https://scholarworks.sjsu.edu/etd_theses/3458)

This Thesis is brought to you for free and open access by the Master's Theses and Graduate Research at SJSU ScholarWorks. It has been accepted for inclusion in Master's Theses by an authorized administrator of SJSU ScholarWorks. For more information, please contact [scholarworks@sjsu.edu](mailto:scholarworks@sjsu.edu).

CHARACTERIZATION OF INTERFACIAL INTERACTIONS BETWEEN  
NANOCLAY AND POLYMER MATRIX

A Thesis

Presented to

The Faculty of the Department of Chemical and Materials Engineering  
San Jose State University

In Partial Fulfillment

of the Requirements for the Degree

Master of Science

by

Karl Dietrich Amo

December 2007

UMI Number: 1452071

### INFORMATION TO USERS

The quality of this reproduction is dependent upon the quality of the copy submitted. Broken or indistinct print, colored or poor quality illustrations and photographs, print bleed-through, substandard margins, and improper alignment can adversely affect reproduction.

In the unlikely event that the author did not send a complete manuscript and there are missing pages, these will be noted. Also, if unauthorized copyright material had to be removed, a note will indicate the deletion.

**UMI**<sup>®</sup>

---

UMI Microform 1452071

Copyright 2008 by ProQuest LLC.

All rights reserved. This microform edition is protected against unauthorized copying under Title 17, United States Code.

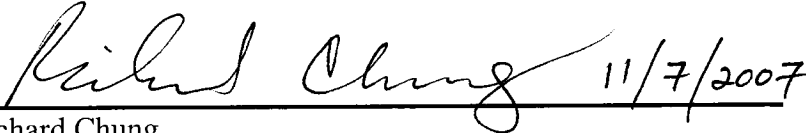
ProQuest LLC  
789 E. Eisenhower Parkway  
PO Box 1346  
Ann Arbor, MI 48106-1346

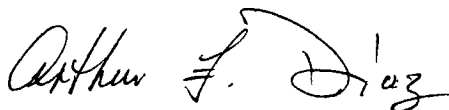
© 2007


Karl Dietrich Amo

ALL RIGHTS RESERVED

APPROVED FOR THE DEPARTMENT OF CHEMICAL AND  
MATERIALS ENGINEERING

 11/7/2007  
\_\_\_\_\_  
Dr. Richard Chung

  
\_\_\_\_\_  
Dr. Arthur Diaz

  
\_\_\_\_\_  
Dr. Yigal Blum, SRI International

APPROVED FOR THE UNIVERSITY

 11/19/2007  
\_\_\_\_\_

## ABSTRACT

### CHARACTERIZATION OF INTERFACIAL INTERACTIONS BETWEEN NANOCLAY AND POLYMER MATRIX

by Karl Dietrich Amo

Polymer-clay nanocomposites are composed of nanometer-thick platelets of montmorillonite dispersed in the polymer matrix. Montmorillonite loadings of a few percent can simultaneously increase stiffness and strength, heat-distortion temperature, and vapor-barrier and fire-retardant properties.

Montmorillonite is negatively charged. In nature, the negative charge is balanced with sodium ions. The sodium can be exchanged with organic cations, which allow montmorillonite to be dispersed into polymers. Different polymers require modification of montmorillonite with specific organic cations.

Atomic force microscopy was employed as a tool for improving interfacial bonding between polymers and organically-modified-montmorillonites (OMMTs). Techniques were developed for coating three polymers onto mica substrates and three OMMTs onto colloidal probes. Force measurements at the interface using the colloidal-probe technique revealed that probes-coated-with-OMMT and substrates-coated-with-polymer produced data with significantly less scatter than the opposite configuration. Factors affecting force measurements were identified.

## ACKNOWLEDGEMENTS

Dr. Yigal Blum of SRI International provided access to a Nano-R® atomic force microscope. He also arranged for the analysis of the coatings of some probes using a scanning electron microscope. Dr. Brent MacQueen provided training on the Nano-R™ and came to the aid of the investigator when technical problems arose.

Pacific Nanotechnology, Inc. provided technical support for the Nano-R™, mounted probes for free, and made helpful suggestions on how to scan a small sphere that was mounted on the end of a probe.

Mr. Robert Cormia provided access to the Nano-R™ at Foothill College when the atomic force microscope at SRI International was down.

Membrane Technology & Research, Inc. provided leave from full-time employment, a laboratory, solvents, a scanning electron microscope, and moral support.

Dr. Richard Chung, the advisor for this study, arranged access to the atomic force microscopes at SRI International and Foothill College. He provided funds for probes and Cloisite® samples. He was also gave encouragement in the face of slow progress and provided a stopping point for the study.

## TABLE OF CONTENTS

List of Figures .....	x
List of Tables .....	xvi
1. INTRODUCTION .....	1
1.1 History of Polymer-Clay Nanocomposites .....	1
1.2 Introduction to Clays.....	2
1.3 Introduction to Intercalation and Exfoliation.....	5
1.4 Introduction to Analytical Tools and Topic.....	6
2. LITERATURE REVIEW .....	7
2.1 General Pattern of Papers.....	7
2.2 Factors Affecting Interfacial Interactions .....	8
2.2.1 Morphology: Intercalation versus Exfoliation.....	8
2.2.2 Polymer .....	13
2.2.3 Clay .....	14
2.2.4 Organic Cation .....	17
2.2.5 Processing .....	21
2.3 Research Direction and Justification .....	23
2.3.1 Tool Choice: Atomic Force Microscopy .....	24
2.3.2 Hydrophobic Interactions and the Colloidal Probe Technique.....	24
2.3.3 Interaction Forces of Montmorillonite and Organic Polycation.....	26
2.3.4 Organoclay Solubility .....	29
2.3.5 Quantitative Equivalence between Polymer Films and Nanocomposites.....	30



2.3.6 Models of Adhesive Interaction.....	30
2.3.7 Factors that Impact Adhesion Force Measurements.....	31
2.3.8 Correlations of Adhesive Force .....	32
2.4 Conclusion of Literature Review.....	33
3. HYPOTHESIS, OBJECTIVES, AND ETHICS.....	35
3.1 Research Hypothesis.....	35
3.2 Experimental Objectives.....	36
3.2.1 Organoclays and Polymers .....	36
3.2.2 Solvents.....	36
3.2.3 Probes and Substrates .....	37
3.2.4 Coating Methods.....	37
3.2.5 Confirmation of Coatings on Colloidal Probes.....	37
3.2.6 Environmental Factors .....	38
3.2.7 Placement Option for Organoclay and Polymer Coatings.....	38
3.2.8 Adhesive Force Experiments .....	39
3.3 Ethics.....	39
4. MATERIALS AND METHODS.....	41
4.1 Organoclays and Polymers .....	41
4.2 Solvent Selection for OMMTs and Polymers.....	43
4.3 Probes and Substrates .....	46
4.3.1 Contact Probes .....	46
4.3.2 Colloidal Probes .....	46

4.3.3 Tip Characterization Grating .....	51
4.3.4 Mica Substrates .....	51
4.4 Atomic Force Microscopy .....	51
4.4.1 Description of the Nano-R™ Atomic Force Microscope .....	51
4.4.2 Environmental Cell .....	55
4.4.3 Reverse Imaging of Particles on Colloidal Probes .....	56
4.4.4 Imaging of Coatings on Mica Substrates .....	61
4.4.5 Force/Distance Curve Technique.....	62
4.5 Coating Colloidal Probes and Substrates.....	70
4.5.1 Coating Colloidal Probes with Organoclays.....	71
4.5.2 Coating Colloidal Probes with Polymers.....	71
4.5.3 Colloidal Probe Coating Simulation Technique .....	72
4.5.4 Pretreating with Silane Coupling Agents.....	73
4.5.5 Coating Substrates with Organoclays .....	75
4.5.6 Coating Substrates with Polymers .....	76
4.6 Safety Precautions.....	77
5. RESULTS AND DISCUSSION .....	78
5.1 Solvent Tests on Organoclays.....	78
5.2 Solvent Tests on Polymers.....	82
5.3 OMMT Coating Experiments on Mica Substrates.....	83
5.4 Polymer Coating Experiments on Mica Substrates .....	86
5.5 OMMT Coating Experiments on Colloidal Probes .....	91

5.6 Polymer Coating Experiments on Colloidal Probes .....	106
5.7 OMMT Placement Option Experiments .....	110
5.7.1 Force/Distance-Curves Experiment with OMMT on the Probe .....	111
5.7.2 Force/Distance-Curves Experiment with PMMA on the Probe .....	118
5.7.3 Interpretation of the Results of the Placement Option Experiments.....	126
5.8 Environmental Factors .....	128
5.9 Adhesive Force Experiments .....	129
5.9.1 Exploratory Experiment One .....	130
5.9.2 Exploratory Experiment Two .....	134
5.9.3 Exploratory Experiment Three .....	135
5.9.4 Interpretation of Results.....	144
5.10 Suggestions for Future Work.....	146
6. CONCLUSIONS.....	148
REFERENCES .....	141
APPENDIX A: MODIFIED SWELLING TEST RESULTS ON CLOISITE® 30B.....	156

## LIST OF FIGURES

Figure 1. Silicate sheet.....	2
Figure 2. Smectite structure .....	4
Figure 3. TEM image showing arrangement of layered silicates in the injection molding direction (arrow), and perpendicularly oriented lamellae .....	9
Figure 4. Three models of deformation of stacked polymer-silicate layers .....	10
Figure 5. Nanostructured network in an inorganic-organic nanocomposite.....	11
Figure 6. Type A, B, and C interfacial interactions in polymer-clay nanocomposites .....	12
Figure 7. Comparison of tensile strengths and moduli .....	18
Figure 8. The Cloisite® selection chart of Southern Clay Products, Inc.....	21
Figure 9. Measured long range interaction force as a function of distance between a hydrophobic glass sphere and silica plates of various hydrophobicities as they approached each other in water.....	25
Figure 10. AFM images of PDDACl self-assembled onto a silicon wafer (top) and montmorillonite self-assembled onto a PDDACl-coated silicon wafer (bottom) .....	27
Figure 11. MikroMasch CSC12 probe mounted on a PNI substrate with silver epoxy. Image magnified 6.5 times.....	50
Figure 12. Stage components of PNI Nano-R™ atomic force microscope.....	53
Figure 13. Probe exchange position of Nano-R™ scanner head, showing the probe mount .....	54
Figure 14. Light lever system for measuring the deflection of a probe cantilever .....	55
Figure 15. Representation of 5-micron diameter spheres over TGT1 grating, to scale.....	57

Figure 16. Scan Image window in the Nano-R™ SPM Cockit software, obtained by scanning a colloidal probe with a five-micron-diameter sphere over a TGT1 tip characterization grating.....	58
Figure 17. Line analysis on Z(SEN) data using NanoRule+, for determining the diameter of a borosilicate particle on a coated colloidal probe. ....	61
Figure 18. Roughness measurement in NanoRule+, using Z(SEN) scan data obtained from a nylon 6 coating on mica.....	62
Figure 19. Force/distance curve between a colloidal probe and a flat surface, showing representations of a colloidal probe as it first approaches a surface until it retracts. ....	64
Figure 20. Plot of the retraction portion of force/distance curve data, including calculation of the adhesive force $F_{adh}$ using two methods. ....	67
Figure 21. Force/distance retraction curves showing the dependence of Z(ERR), and the independence of Z(GHT), on laser spot distance from the probe end.....	69
Figure 22. Sealed and coated pipette tip under a visible-light microscope .....	73
Figure 23. Stainless steel vessel used to apply silane coupling agents to colloidal probes and borosilicate pipettes via vapor deposition.....	74
Figure 24. Dispersions of 320 ppm Cloisite® 30B, 25A, and 20A in <i>n</i> -methyl-2-pyrrolidone.....	80
Figure 25. Dispersions of 320 ppm Cloisite® 25A in chloroform; 1,1,1-trichloroethane; <i>n</i> -methyl-2-pyrrolidone; and dimethylacetamide.....	80
Figure 26. Dispersions of 320 ppm Cloisite® 20A in chloroform, <i>n</i> -methyl-2-pyrrolidone, dimethylacetamide, dimethylformamide, and tetrahydrofuran.....	81
Figure 27. Visible-light photograph of a mica substrate with a dried Cloisite® 25A coating.....	83
Figure 28. Three-dimensional image of a 10.2 μm AFM scan of Cloisite® 20A coating made by drop casting a 3,200 ppm dispersion in chloroform at 22° C in air.....	85

Figure 29. Three-dimensional images of 10.2 $\mu\text{m}$ AFM scans of smooth polymer coatings on mica substrates.....	90
Figure 30. SEM image showing an uneven coating of Cloisite® 25A on the borosilicate particle of a new probe dip-coated in a 320 ppm Cloisite® 25A – chloroform solution.....	92
Figure 31. SEM image of gold-sputtered colloidal probe before it was dip-coated.....	93
Figure 32. SEM image of probe after dip-coating in 320 ppm Cloisite® 25A – NMP .....	94
Figure 33. SEM image of probe after dip-coating in 3,200 ppm Cloisite® 25A – NMP .....	95
Figure 34. SEM image of probe after dip-coating in 32,000 ppm Cloisite® 25A – NMP .....	96
Figure 35. SEM image of a probe after sputtering it with gold, dip coating it in 3,200 ppm Cloisite® 25A – NMP solution, drying it, and sputtering it with gold again.....	97
Figure 36. SEM image of a new probe – a blank.....	97
Figure 37. EDX spectrum of a colloidal probe sputtered with gold, dip coated in 32,000 ppm Cloisite® 25A – NMP solution, and sputtered again with gold .....	98
Figure 38. EDX spectrum of a blank – a new colloidal probe.....	99
Figure 39. EDX images of a colloidal probe sputtered with gold, dip coated in 32,000 ppm Cloisite® 25A – NMP solution, and sputtered again with gold .....	100
Figure 40. AFM contrast-brightness displays of Z(SEN) on the left Z(ERR) on the right, obtained by reverse imaging the colloidal probe shown in Figure 35 (first sputtered with gold and then dip-coated in 32,000 ppm Cloisite® 25A – NMP solution) .....	101
Figure 41. Contrast-brightness displays of Z(SEN) on the left and Z(ERR) on the right obtained by reverse imaging the blank colloidal probe shown in Figure 36 via AFM.....	101

Figure 42. SEM image showing a rough coating of Cloisite® 25A on the borosilicate particle of a new probe dip-coated in a 10 % Cloisite® 25A – NMP solution .....	103
Figure 43. SEM image showing a lack of a visible coating of Cloisite® 25A on most of the borosilicate particle of a new probe first sputtered with gold and then dip-coated in a 10 % Cloisite® 25A – NMP solution.....	103
Figure 44. SEM image obtained on a Hitachi S-2300 showing a thick coating of PMMA on a colloidal probe that was first silane-treated with APTES and then dip-coated in a 10 % PMMA – toluene solution.....	107
Figure 45. SEM image obtained on a Leica Leo 435 showing a coating of PMMA on the borosilicate particle of the same colloidal probe shown in Figure 44 .....	108
Figure 46. EDX spectrum of the colloidal probe silane-treated with APTES and dip coated in 10% PMMA – toluene solution.....	109
Figure 47. SEM image showing a colloidal probe that was sputter coated with gold and then dip-coated a 10% PMMA – toluene solution.....	110
Figure 48. Three-dimensional images of 2.2 $\mu\text{m}$ and 0.7 $\mu\text{m}$ AFM scans of borosilicate particle on colloidal probe when it was new, before it was coated with Cloisite® 20A.....	112
Figure 49. Three-dimensional images of 2.2 $\mu\text{m}$ and 0.7 $\mu\text{m}$ AFM scans of borosilicate particle on colloidal probe after silane treating it with APTES and dip coating it in a 3,200 Cloisite® 20A – chloroform solution.....	112
Figure 50. Force/distance retraction curves and corresponding peak-width values obtained between a colloidal probe coated with Cloisite® 20A and a mica substrate coated with PMMA.....	116
Figure 51. Normal probability plot of the peak-width values shown in Figure 50.....	117
Figure 52. Three-dimensional images of 2.2 $\mu\text{m}$ and 0.7 $\mu\text{m}$ AFM scans of borosilicate particle on colloidal probe when it was new, before it was coated with PMMA.....	119
Figure 53. Three-dimensional images of 2.2 micron and 0.7 micron AFM scans of borosilicate particle on colloidal probe after silane treating it with APTES and dip coating it in a 1 % PMMA – toluene solution .....	120

Figure 54. Three-dimensional images of a 7.3 $\mu\text{m}$ scan (left) and a 1.5 $\mu\text{m}$ AFM scan (right) of the cantilever of a colloidal probe in an area visibly coated with PMMA.....	121
Figure 55. Three-dimensional representation of Z(ERR) obtained from a 10.2 $\mu\text{m}$ scan of a mica substrate coated with Cloisite® 20A using a colloidal probe coated with PMMA.....	122
Figure 56. Force/distance retraction curves and corresponding peak-width values obtained between a colloidal probe coated with PMMA and a mica substrate coated with Cloisite® 20A .....	123
Figure 57. Force/distance retraction curves and corresponding peak-width values obtained between a colloidal probe coated with PMMA and a mica substrate coated with Cloisite® 20A .....	124
Figure 58. Force/distance retraction curves and corresponding peak with values obtained between a colloidal probe coated with PMMA and a mica substrate coated with Cloisite® 20A .....	125
Figure 59. Force/distance retraction curves and corresponding peak-width values obtained between a colloidal probe coated with Cloisite® 20A and a mica substrate coated with PE-MA.....	131
Figure 60. Force/distance retraction curves and corresponding peak-width values obtained between a colloidal probe coated with Cloisite® 20A and a mica substrate coated with PE-MA.....	132
Figure 61. Three-dimensional representation of Z(SENS) obtained from a 10.2 $\mu\text{m}$ scan of a mica substrate coated with PE-MA using a colloidal probe coated with Cloisite® 20A .....	133
Figure 62. Force/Distance Curve window of the Nano-R®'s SPM Cockpit software, between a colloidal probe coated with Cloisite® 25A and a smooth coating of PEMA on a substrate.....	135
Figure 63. Force/distance retraction curves and corresponding peak-width values obtained between a colloidal probe silane treated with EPPMS and a mica substrate coated with PMMA.....	137
Figure 64. Force/distance retraction curves and corresponding peak-width values obtained between a colloidal probe silane treated with EPPMS and a mica substrate coated with PMMA.....	138



Figure 65. SPM Cockpit Force/Distance Curve window, showing a poor-quality force/distance curve .....	139
Figure 66. Force/distance retraction curves and corresponding peak-width values obtained between a colloidal probe silane-treated with EPPMS and coated with Cloisite® 25A and a mica substrate coated with PMMA .....	140
Figure 67. Contrast-brightness display of Z(ERR) on the left and line analysis of Z(SEN) on the right of a 10.2 $\mu\text{m}$ scan of a colloidal probe silane-treated with EPPMS and dipped in NMP, and then used to obtain force/distance curves with a PMMA-coated substrate.....	142
Figure 68. Contrast-brightness display of Z(ERR) on the left and line analysis of Z(SEN) on the right of a 5.1 $\mu\text{m}$ scan of a colloidal probe silane-treated with EPPMS and dip-coated in 3,200 ppm Cloisite® 25A, and then used to obtain force/distance curves with a PMMA-coated substrate. ....	143

## LIST OF TABLES

Table 1.	Selected properties of nanocomposites of Nylon-6 and clay minerals.....	15
Table 2.	Organic modifiers and concentrations in grades of Cloisite®.....	41
Table 3.	Quantity and characteristics of colloidal probes in the order that the probes were purchased.....	47
Table 4.	Results of Modified Solvent Swelling tests on Cloisite® 30B, 25A, and 20A, with thickness of swollen OMMTs measured in millimeters .....	79
Table 5.	Solvent test results on polymers, giving test temperature and time for dissolution of 1 wt% mixtures, and stability of the solutions at room temperature .....	82
Table 6.	Root mean square roughness of ten-micron scans of Cloisite® coatings on mica substrates, determined by atomic force microscopy.....	84
Table 7.	Polymer solution drop casting experiments on mica substrates, including percent area estimates of glassy surface on each coating, and roughness measurements of ten-micron scans over glassy areas by AFM.....	87
Table 8.	Effect of Cloisite® 20A concentration and APTES treatment on coating quality of dipped lengths of borosilicate pipettes, from the first experiment.....	105
Table 9.	Effect of Cloisite® 25A and 30B concentration and EPPMS treatment on amount coated on dipped-lengths of borosilicate pipettes, from the second experiment .....	105
Table 10.	Effect of Cloisite® 25A and 30B concentration and EPPMS treatment on amount coated on dipped-lengths of borosilicate pipettes, from the third experiment.....	105
Table 11.	Effect of PMMA concentration and APTES treatment on coating coverage of dipped lengths of borosilicate pipettes.....	106
Table 12.	Z(ERR) values recorded from force/distance retraction curves, obtained between a colloidal probe coated with Cloisite® 20A and a mica substrate coated with PMMA.....	115

## CHAPTER ONE INTRODUCTION

### 1.1 History of Polymer-Clay Nanocomposites

In the early 1980s, Toyota Central Research Laboratories in Japan began to work on polymer-clay nanocomposites. They developed the first known polymer-clay nanocomposite – a nanocomposite consisting of nylon 6 and montmorillonite clay. At a clay loading of 5%, this nanocomposite exhibited a 40% increase in tensile strength over unfilled nylon 6. The flexural modulus increased 68%, and the heat distortion temperature rose from 65° C to 152° C. The impact strength decreased by only 10% [1]. These characteristics extended the use of nylon in engine compartments of automobiles.

In 1993, workers at Cornell University in New York reported a versatile technique for synthesizing polymer-clay nanocomposites. The technique consists of mixing modified clay directly into melted polymer. Up until that time, the known techniques consisted of mixing clay with monomer and polymerizing *in situ*, or diluting the polymer in solvent prior to mixing with clay. The new technique increased the viability of synthesizing nanocomposites with many engineering polymers. This advancement motivated vigorous research [2].

Significant efforts have been made to develop new polymer-clay nanocomposites for various applications, as the technology is applicable to a wide range of polymers. The efforts have met with some success. In 1999, Principia Partners (an industrial business consulting firm) reported that the global market for clay-polymer nanocomposites totaled two million pounds of nanoclay-nylon, which was produced by Ube Industries of Japan

for automotive applications and by Unitika of Japan for packaging applications [3]. In 2006, BCC Research reported that the market in 2005 was 5.5 million pounds [4]. In 2005, Noda *et al.* summarized polymer/clay nanocomposite research in the past decade as being focused on formulating and compounding different polymer-clay nanocomposites, measuring material properties, and characterizing microstructure [5].

## 1.2 Introduction to Clays

Clays are a class of minerals consisting of mainly silica ( $\text{SiO}_2$ ) and alumina ( $\text{Al}_2\text{O}_3$ ). A basic structural component in clays is the silicate sheet, consisting of silicon-oxygen six-membered rings. It has the repeat formula  $\text{Si}_2\text{O}_5^{2-}$ ; it extends in two dimensions indefinitely. See Figure 1.

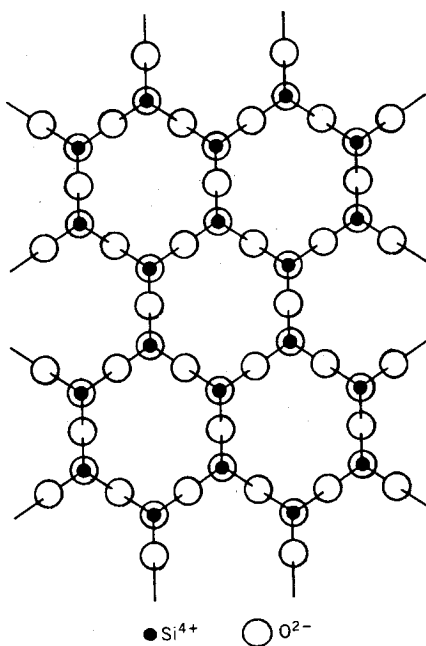


Figure 1. Silicate sheet [6]. Reprinted with permission from John Wiley & Sons, Inc.

The oxygen atom valences within the rings are satisfied by being bonded to two silicon atoms. There are also unbonded oxygen atoms projecting upward out of the plane of the silicate sheet; they are shown as being immediately above the silicon atoms.

In the common clay minerals the kaolinites, the unbonded oxygen atoms are made electrically neutral by a sheet of gibbsite located directly above the silicate sheet. A gibbsite sheet consists of aluminum hydroxide six-membered rings. It has a repeat formula of  $\text{Al}_2(\text{OH})_4^{2+}$ . The unbonded oxygen atoms of the silicate sheet project upward into the gibbsite sheet, creating a bridge between the two sheets. The two sheets are bonded through the shared oxygen atoms, forming a composite unit layer. The unit formula is  $\text{Al}_2\text{Si}_2\text{O}_5(\text{OH})_4$ .

Kaolinites consist of many unit layers sandwiched together; the unit layers are attached by hydrogen bonds. The layers can stack in several orientations relative to each other, yielding the four minerals in the kaolin group.

Minerals of other groups consist of different composite unit layers. If one gibbsite sheet is chemically condensed between two silicate sheets, then a mineral of the smectite group is formed. The unit formula is  $\text{Al}_2\text{Si}_4\text{O}_{10}(\text{OH})_2$ . See Figure 2.

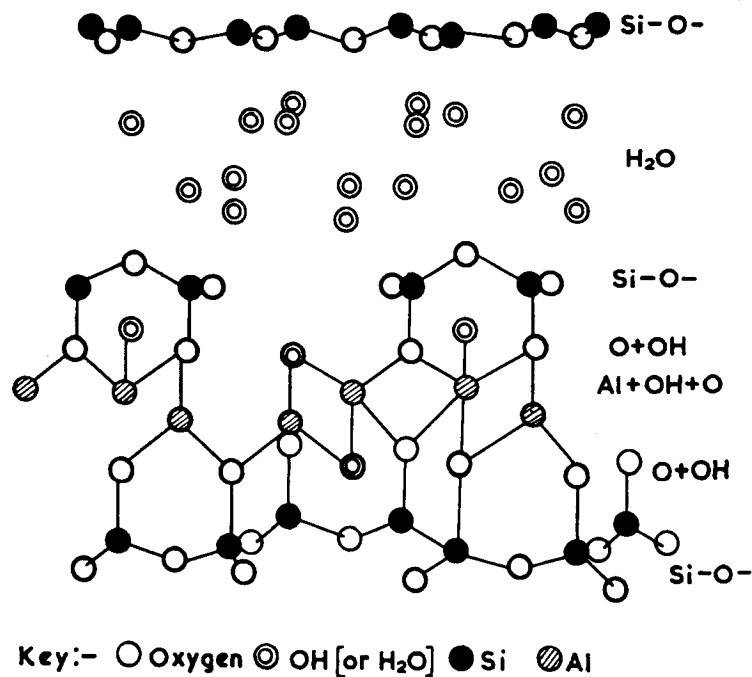


Figure 2. Smectite structure [7]. Reproduced with the kind permission of Springer Science and Business Media.

The smectite group has special properties which allow it to form nanocomposites with polymers. Like the kaolinites, the unit layers of the smectites are stacked on top of each other. Unlike the kaolinites though, the layers of the smectites are bonded by van der Waals forces. There are no hydrogen atoms available to form hydrogen bonds because the atoms at the layer interfaces consist only of silicon and oxygen. Van der Waals forces are significantly weaker. Therefore, the unit layers of the smectites can be more easily separated than those of the kaolinites.

In naturally occurring smectites, some of the trivalent aluminum atoms are missing. They are replaced by divalent metal atoms, such as magnesium, lithium, and silicon. This replacement results in an overall negative charge in the structure. (If the substituting metal atom is magnesium, then the mineral is montmorillonite.) The

negative charge is balanced by cations, such as  $\text{Na}^+$ , situated between the unit layers. These cations are bonded relatively weakly. They can be exchanged with other cations. In addition, water molecules are present between the unit layers. Some of the water is adsorbed by the charged surface, and some of it is held by the cations as water of hydration.

### 1.3 Introduction to Intercalation and Exfoliation

The weak bonds between the unit layers and the exchangeability of the cations between the unit layers make the smectites useful for synthesizing nanocomposites. The unit layers are approximately 1 nm thick; the space between the unit layers constitutes a gap 0.3 nm thick [8]. The gap is known as a van der Waals gap, gallery, or interlayer. It is ordinarily hydrophilic, but it can be made organophilic by exchanging the metal cations with various organic cation molecules, such as alkylammonium salts.

Modifying a smectite with organic cation molecules increases the space between the unit smectite layers. The increased space coupled with the interlayer being organophilic makes it possible for organic solvents, monomers, and melted polymer to diffuse into the interlayer. When this happens, the space between the smectite unit layers increases as organic molecules diffuse in. If polymer penetration results in a finite expansion that retains well-ordered multilayers consisting of alternating polymer and smectite layers, then the resulting clay-polymer nanocomposite is said to be intercalated. If extensive polymer penetration results in delamination, it is said to be exfoliated. In the exfoliated state, a nanocomposite consists of individual nanometer-thick clay unit layers

suspended in a polymer matrix. Complete exfoliation usually results in the greatest enhancement of properties.

#### 1.4 Introduction to Analytical Tools and Topic

Common tools used in research on polymer-clay nanocomposites include wide-angle x-ray diffraction, and transmission electron microscopy. These tools are used to determine the degree of intercalation and exfoliation. Other tools are used to measure macroscopic properties; they are often the same tools used to measure the properties of unmodified polymers. Macroscopic properties of greatest interest are usually properties that are enhanced by the incorporation of nanoclay into a polymer matrix. These properties include strength and toughness, gas barrier, heat/dimensional stability, and flame retardant properties. Others tools used to characterize nanocomposites include small-angle x-ray diffraction, scanning electron microscopy, differential scanning calorimetry, Fourier-transform infrared spectroscopy, and atomic force microscopy [9].

The improvements in strength and toughness due to the presence of exfoliated clay in a polymer are functions of the interfacial interactions between the modified clay and the polymer matrix. The functions are somewhat opposing. Polymer-clay adhesion allows the transfer of stress to the reinforcing clay particles, which increases the tensile strength. However, polymer-clay bonds can absorb energy by breaking and forming microvoids; the formation of microvoids during deformation increases toughness (impact strength). Therefore, the study of the interfacial bonding strength and related interaction characteristics between nanoclay and a polymer matrix may yield insights into optimizing performance [10].



## CHAPTER TWO LITERATURE REVIEW

### 2.1 General Pattern of Papers

Few papers in the literature of polymer-clay nanocomposites specifically address interfacial bonding strength and related interaction characteristics. In the majority of papers, the topic is usually, at most, mentioned in the introduction to help explain the impressive properties of polymer-clay nanocomposites, or mentioned in a discussion section to explain phenomena and/or to suggest that improved bonding between the polymer matrix and nanoclay may enhance the specific property of interest.

The focus of many reported studies is achieving regular intercalated structures or complete exfoliation of a smectite clay in a polymer. These papers follow the pattern of describing a particular combination of polymer, clay, and organic cation used to modify the clay, and a process used to combine the materials to produce the nanocomposite. The reports usually include x-ray diffraction spectra and transmission-electron-microscopy (TEM) images that confirm the desired intercalated or exfoliated structures. The papers go on to provide data showing the benefit that the nanocomposite affords over pristine or conventionally-filled polymer – be it in improved strength, gas barrier, heat/dimensional stability, or flame retardant properties.

Papers that report improved mechanical properties are generally more applicable to the topic of bonding strength and related interaction characteristics. The reinforcing effect of nanoclay is usually reported in terms of tensile strength for characterization of strength, tensile modulus for stiffness, percent strain-at-break for toughness (the correct

toughness parameter would be impact strength), and sometimes the rheological properties of storage and loss moduli.

## 2.2 Factors Affecting Interfacial Interactions

A review of the literature reveals the existence of several types of interfacial interactions, and a variety of effects. The types of interactions and effects present in a specific polymer-nanoclay system depend on many factors. The characteristics of interfacial bonding in a specific polymer-nanoclay system depend on morphology, the type of clay, the type of polymer, type of organic cation, and the processing technique used. The resulting interfacial interactions have effects. Some of the effects are the measurable benefit that the nanocomposite affords over pristine or conventionally filled polymer. Other effects may not produce any apparent benefit, but their measurement and analysis may yield insight into the character of the interfacial interactions.

### 2.2.1 Morphology: Intercalation versus Exfoliation

The greatest morphological difference among polymer-clay nanocomposites is intercalation versus exfoliation. This difference results in different interactions between the nanoclay and the polymer matrix. Kim *et al.* reported on the influence of intercalated montmorillonite on the deformation process of polyamide-12 nanocomposite [11]. They prepared ultra-thin sections of the nanocomposite, and applied uniaxial stress to the sections while photographing them with a transmission electron microscope (TEM).

The nanocomposite contained dispersed but highly-oriented and regularly intercalated montmorillonite, which Kim *et al.* referred to as silicate layers. TEM images

showed that the silicate layers were oriented in the direction of shear caused by injection molding the nanocomposite. The TEM image (shown in Figure 3) also revealed that the lamellae of the polyamide matrix (semi-crystalline) were oriented perpendicularly to the polymer/silicate interface, *i.e.* in planes lying normal to the injection molding direction.

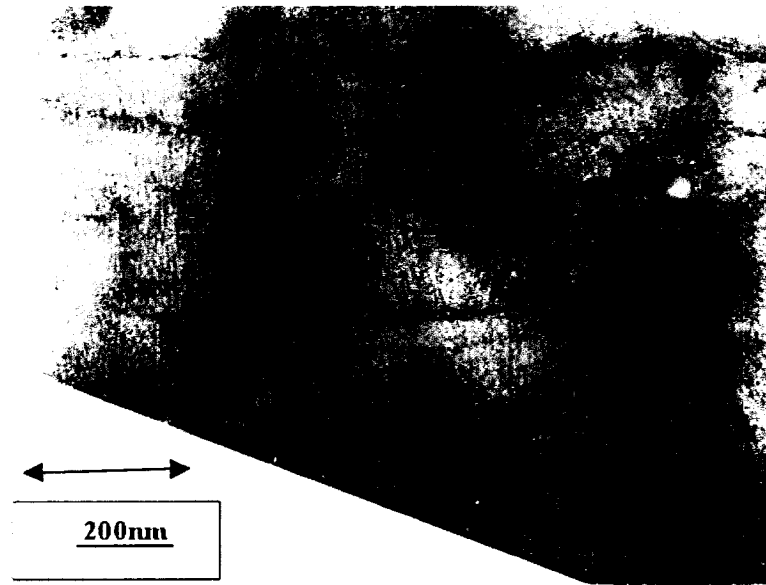


Figure 3. TEM image showing arrangement of layered silicates in the injection molding direction (arrow), and perpendicularly oriented lamellae [11]. Reprinted with permission. Copyright 2001Elsevier.

Kim *et al.* speculated that the ordering is a result of the crystallization process, and that the edges of the layered silicates act as nucleation sites for lamellae formation.

Photographs taken by TEM during the application of uniaxial stress applied in the same direction as the injection-molding shear revealed microvoids developing inside the stacked silicate layers during plastic deformation. The microvoids did not propagate into the adjacent lamellae. The formation of microvoids allowed relief of localized stresses. Strong ionic interaction between the lamellae at the edges of the silicate layers prevented the initiation of a fracture process, enhancing toughness. As microvoids grew, the

localized strain was transferred to the polymer matrix. Consequently, stiffness was enhanced.

Uniaxial stress was applied in other directions. In every case, microvoids formed inside the stacked silicate layers. The results clearly indicated that the bonds between the silicate layers were weaker than the bonds between the edges of the silicate layers and the adjacent lamellae. The authors produced three models of the micromechanical deformation process, which are represented in Figure 4.

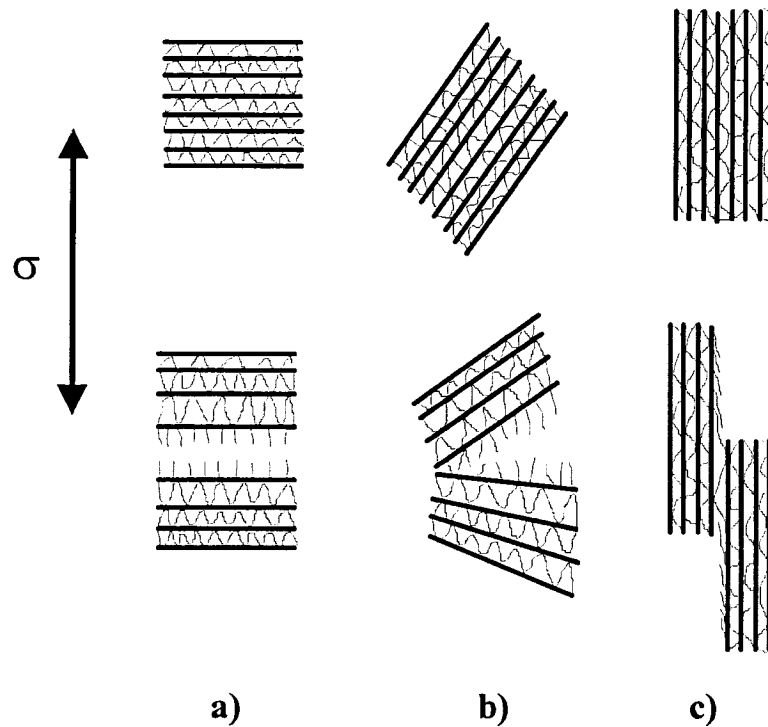


Figure 4. Three models of deformation of stacked polymer-silicate layers [11]. Reprinted with permission. Copyright 2001 Elsevier.

The results led Kim *et al.* to propose a new class of polymeric materials: nanostructured networks in inorganic-organic nanocomposites. See Figure 5.

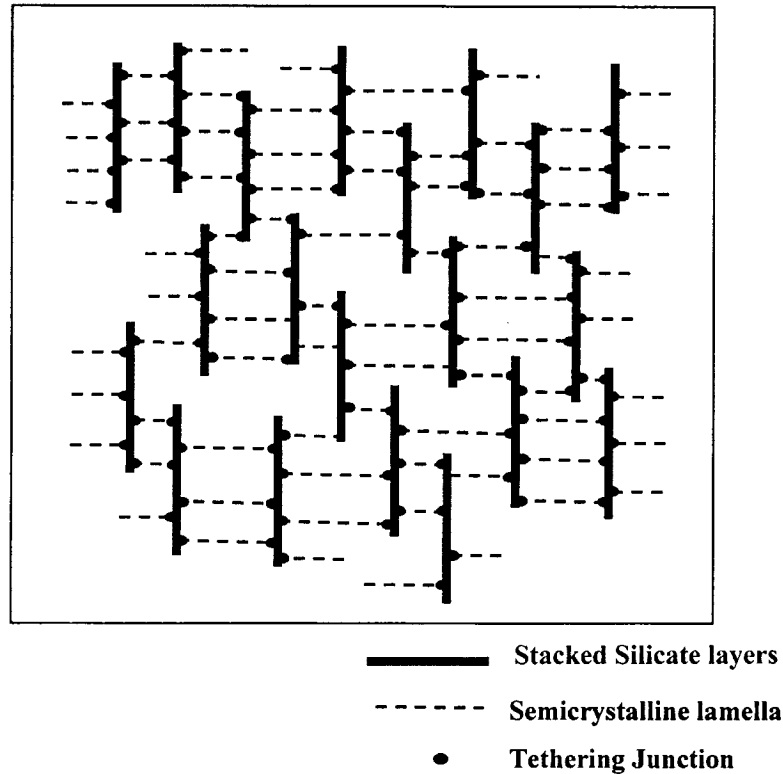


Figure 5. A nanostructured network in an inorganic-organic nanocomposite [11]. Reprinted with permission. Copyright 2001 Elsevier.

The structure represented in Figure 5 consists of finely and uniformly dispersed stacked-silicate-layers that are aligned perpendicularly to lamellae, with the edges of the silicate layers strongly bonded to the lamellae. Kim *et al.* claimed that a nanocomposite tailored to produce such a structure would result in a material showing simultaneous enhancement of stiffness and toughness.

Shi *et al.* proposed a model for the interfacial interactions occurring between exfoliated organically-modified montmorillonite and a rubbery epoxy [12]; Figure 6 illustrates three types of interactions that may occur.

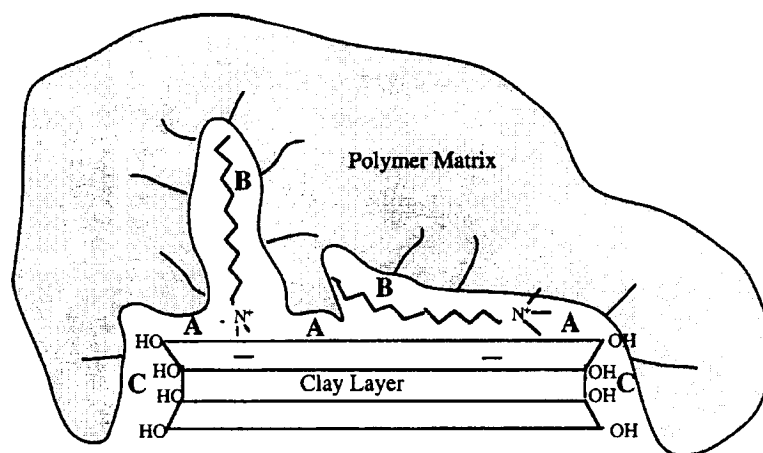


Figure 6. Type A, B, and C interfacial interactions in polymer-clay nanocomposites [12]. See text for further discussion of each type. Reprinted with permission. Copyright 1996 American Chemical Society.

Shi *et al.* described the interactions occurring at the polymer-organoclay interface as being complex. The types of interactions or bonding were designated A, B, and C. Interaction A is the binding or adsorption of polymer to the chemically-inert siloxane oxygen atoms located on the basal surfaces of the silicate layers. Interaction B occurs where the organic end of the organic cations dissolves into the polymer matrix. Interaction C occurs where the hydroxides at the edges of silicate layers bind with the polymer matrix.

The interaction model provided by Shi *et al.* for their exfoliated montmorillonite-epoxy system is significantly different than the model provided by Kim *et al.* for their structured, intercalated montmorillonite-polyamide system. Comparing the models suggests that the model interactions for the exfoliated nanocomposite (Shi *et al.*) are more basic in that the interactions described are localized to a clay layer and the surrounding polymer matrix. In contrast, the model for a structured, intercalated nanocomposite (Kim *et al.*) is larger in scale, involving both clay structures (stacked silicate layers) and

polymer structures (lamella). In addition, the model for a structured, intercalated nanocomposite includes void formation; the model for an exfoliated nanocomposite does not.

### 2.2.2 Polymer

The two polymer-clay interaction models described above were developed from studies of nanocomposites containing different polymers. The type of polymer in a nanocomposite matters; it can affect the strength of interaction between the clay and the polymer. Lim *et al.* reported the melting point depressions for organically-modified montmorillonite (OMMT) in three polymers: poly(ethylene oxide) (PEO), poly(methyl methacrylate) (PMMA), and a 50/50 blend of miscible PEO and PMMA [13]. They calculated Flory-Huggins interaction parameters from the melting-point-depression data. For PMMA/OMMT, the value was  $-13.87 \text{ cal/cm}^3$ . For PEO/OMMT, the value was  $-0.35 \text{ cal/cm}^3$ . These values indicate that OMMT has a stronger association for PMMA than PEO. These results are consistent with x-ray diffraction data. X-ray diffraction data showed that the layer thickness of intercalated PMMA/OMMT was greater than the layer thickness of PEO/OMMT, pointing to a better association or interaction between PMMA and OMMT.

Data from a study by Loo *et al.* suggests that the interaction between exfoliated montmorillonite and nylon 6 is strong. They studied deformation behavior of exfoliated montmorillonite in a nylon 6 [14]. Pellets from UBE Industries of grade 1022B nylon 6 homopolymer and grade 1022C5 nylon 6 containing 5 wt% montmorillonite clay (polymerized *in situ*) were dissolved in 2,2,2-trifluoroethanol and then spun cast to

produce films of 6-micron thickness. Infrared spectra of both films were taken; the spectra were analyzed to determine which peaks corresponded to Si-O stretching modes. Infrared spectra of the nanocomposite film were then taken at increments of increasing strain.

Analysis revealed peak frequency shifts in the Si-O stretching modes, indicating changes in silicate structure arising from deformation of silicate layers. In their paper, Loo *et al.* stated that work was underway to compare the FTIR results to computer simulations of clay-layer deformation. It does not appear that results of this work have been published yet. There is sufficient information, though, to conclude that there is a transfer of strain from the polymer matrix to the nanoclay, and that the bonds between the exfoliated montmorillonite layers and nylon 6 are sufficiently strong to transfer enough stress to measurably deform the silicate structure. This specific case can be extended to a general conclusion that interactions between polymers and nanoclays can be strong.

### 2.2.3 Clay

Usuki *et al.* compared the mechanical properties of four nylon 6 nanocomposites consisting of different clay minerals [15]. The minerals were montmorillonite, saponite, hectrite, and synthetic mica, with cation exchange capacities of 120, 100, 50, and 100 meq / 100 grams, respectively. The content of clay mineral in each nanocomposite was 5 wt%. Transmission electron micrographs (TEMs) were taken to confirm that the clay in each nanocomposite was exfoliated. As shown in Table 1, the tensile strength and heat distortion temperature of the nanocomposite containing montmorillonite were superior to pristine nylon 6.



Table 1. Selected properties of nanocomposites of nylon-6 and clay minerals [15].

Properties	Montmorillonite	Mica	Saponite	Hectrite	Pristine Nylon 6
Tensile strength, MPa, at 23 °C	97.2	93.1	84.7	89.5	68.8
Heat distortion temperature, °C	152	145	107	93	65
Heat of fusion, J/g	61.1	57.2	51.5	48.4	70.9

Usuki *et al.* used a differential scanning calorimeter to measure the crystallinity of the four nanocomposites and pristine nylon 6. The heat of fusion of the pristine nylon 6 was the highest; that of the nanocomposite containing montmorillonite was the second highest. Among the nanocomposites, the heat-of-fusion values correlated with heat distortion temperatures; the higher heat-of-fusion values corresponded to higher heat distortion temperatures. Usuki *et al.* surmised that montmorillonite interacted the most strongly with nylon 6, resulting in better mechanical reinforcement and less decrease in crystallinity compared to the other nanocomposites studied.

The cation exchange capacities of the clay minerals that Usuki *et al.* used were not all the same. Wang *et al.* showed that higher cation exchange capacity can result in a reduced improvement in tensile strength [16]. They prepared nanocomposites synthesized via *in situ* polymerization of epoxy resins containing montmorillonite and magadiite modified with the organic cation  $\text{CH}_3(\text{CH}_2)_{17}\text{NH}_2\text{CH}_3$ . The magadiite, a synthesized silicic acid, had a higher cation exchange capacity than the montmorillonite. Thus, it contained more of the organic cation. (Values for the cation exchange capacities were not given.) At low clay loadings, the nanocomposites had similar tensile strength and tensile modulus. At clay loadings of greater than 5 wt%, the nanocomposite

containing montmorillonite had higher tensile strength and tensile modulus. Wang *et al.* attributed the effect to greater organic-modifier content in the magadiite, which contributed to greater dangling chain formation. Dangling chains have a plasticizing effect, weakening the epoxy and thereby compromising the reinforcement effect of exfoliated clay.

The mechanism for dangling chain formation was reported by Lan *et al.* [17]. The acidity of organic cations causes some of the epoxy resin that intercalates into a modified clay to self-polymerize. This phenomenon serves to warn that interactions between polymers, clay, and organic cations are varied and complex. It suggests keeping the cation exchange capacity constant in a study unless the effects of changes in cation exchange capacity are being studied.

There is information regarding the issue of reduction of crystallinity due to the presence of clay in polymers other than nylon 6. Gopakumar *et al.* studied the physical properties of a nanocomposite consisting of exfoliated montmorillonite in polyethylene [18]. They reported that the presence of exfoliated clay resulted in a significant reduction of the degree of crystallinity and an increase in polymer crystallization rates. They attributed the decrease in degree of crystallinity to a reduction in the mobility of crystallizable chain segments. They noted that reduced crystallinity is expected to have a deleterious effect on tensile strength, thereby counteracting some of the reinforcement afforded by the presence of the nanoclay.

#### 2.2.4 Organic Cation

The model by Shi *et al.* for describing the interfacial interactions of an exfoliated clay layer in a polymer matrix was described above. Shi *et al.* also probed the relative importance of type A and B interfacial interactions by varying the length of the straight-chain organic ends of the alkylammonium cations used to modify the montmorillonite. They achieved exfoliation of modified montmorillonite in a rubbery epoxy (subambient glass transition temperature) with the alkylammonium cations  $\text{CH}_3(\text{CH}_2)_2\text{NH}_3^+$  (3-carbon atom chain) and  $\text{CH}_3(\text{CH}_2)_{17}\text{NH}_3^+$  (18-carbon atom chain). They measured the tensile strengths and tensile moduli of the nanocomposite containing the short-chain organic cation (designated 3A-mont-3x) and the nanocomposite containing the long-chain organic cation (designated 18A-mont). Comparisons of the tensile strengths and tensile moduli are shown in Figure 7.

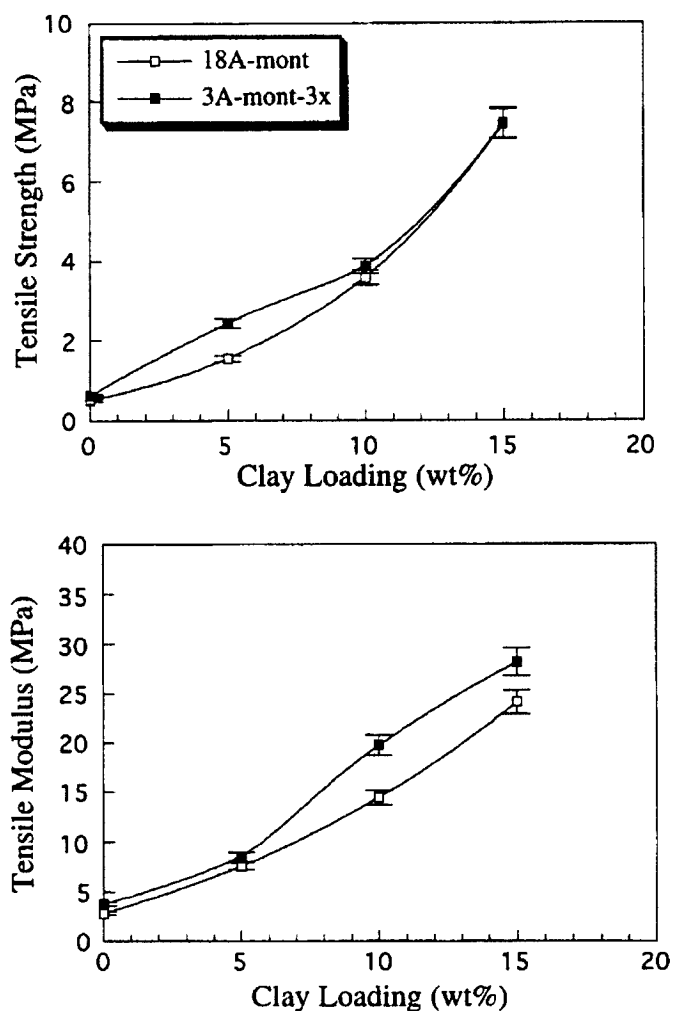


Figure 7. Comparison of tensile strengths and moduli [12]. Reprinted with permission. Copyright 1996 American Chemical Society.

The two exfoliated clays provided similar reinforcement. The authors noted that the nanocomposite containing 3A-mont-3x had slightly higher strength and stiffness than the nanocomposite containing 18A-mont. They stated that these results strongly suggest that the type A (polymer to silicate) interaction is more important than the type B (polymer to organic cation) interaction. They stated that substantial contributions from type B van der Waals interactions between the polymer and the alkyl chain of the alkylammonium cations were precluded because the strength and stiffness did not

improve with increasing length of the alkyl chain. They surmised that nanocomposites consisting of montmorillonite without organic cations would be similarly reinforced if such nanocomposites were possible to make.

Tanaka *et al.* reported the molecular modeling predictions of binding energy in montmorillonite – nylon 6,6 nanocomposites obtained using a Cerius2® simulator (Accelrys Inc.) [19]. The model incorporates the type A (polymer to silicate) and type B (polymer to organic cation) interactions described by Shi *et al.* Type C (polymer to silicate edge) interaction is ignored. The model was used to predict the individual binding energies of montmorillonite, nylon 6,6, and twelve alkylammonium cations. The main result of the work was the prediction that smaller alkylammonium cations provide for stronger overall interactions than larger ones. In addition, a simulation that excluded all alkylammonium cations provided the strongest bond between the clay and nylon 6,6. These results are in agreement with the conclusions of Shi *et al.*

Fermeglia *et al.* followed the approach of Tanaka *et al.* They performed molecular mechanics/dynamics computer simulations to explore the atomic scale structure and predict the binding energies of nanocomposites consisting of montmorillonite and nylon 6 with several different quaternary ammonium cations [20]. Their results confirmed the results of Tanaka *et al.*; the overall binding energy was greater with smaller alkyl ammonium cations. Their results additionally showed that the substitution of hydrogen atoms with polar groups, such as –OH and –COOH, on the alkylammonium cation increased overall binding energy. Also, their dynamics studies indicated that the hydrocarbon chains of the alkylammonium cations flattened onto the montmorillonite

surface and covered much of it. By doing so, the alkylammonium cations shielded the interactions between the nylon 6 and the montmorillonite. The larger the alkylammonium cation, the greater the surface area it covered. The greater the surface covered, the greater the shielding effect became.

Organic cations play an important role. At the very least, they have the function of allowing polymers and clays to be processed into nanocomposites. This fact is underscored by the fact that Southern Clay Products, a major supplier of montmorillonite for producing nanocomposites, sells six grades of organically-modified montmorillonite, called Cloisite® [21]. All the grades contain montmorillonite of the same cation exchange capacity, but vary in the amount or type of organic cation used to modify the clay. Figure 8 shows the grades of Cloisite® arranged on the vertical axis according to their hydrophobicity. They are arranged on the horizontal axis according to their appropriateness for use according to the hydrophobicity of polymer. Not surprisingly, the more hydrophobic grades of Cloisite® are recommended for use with more hydrophobic polymers.

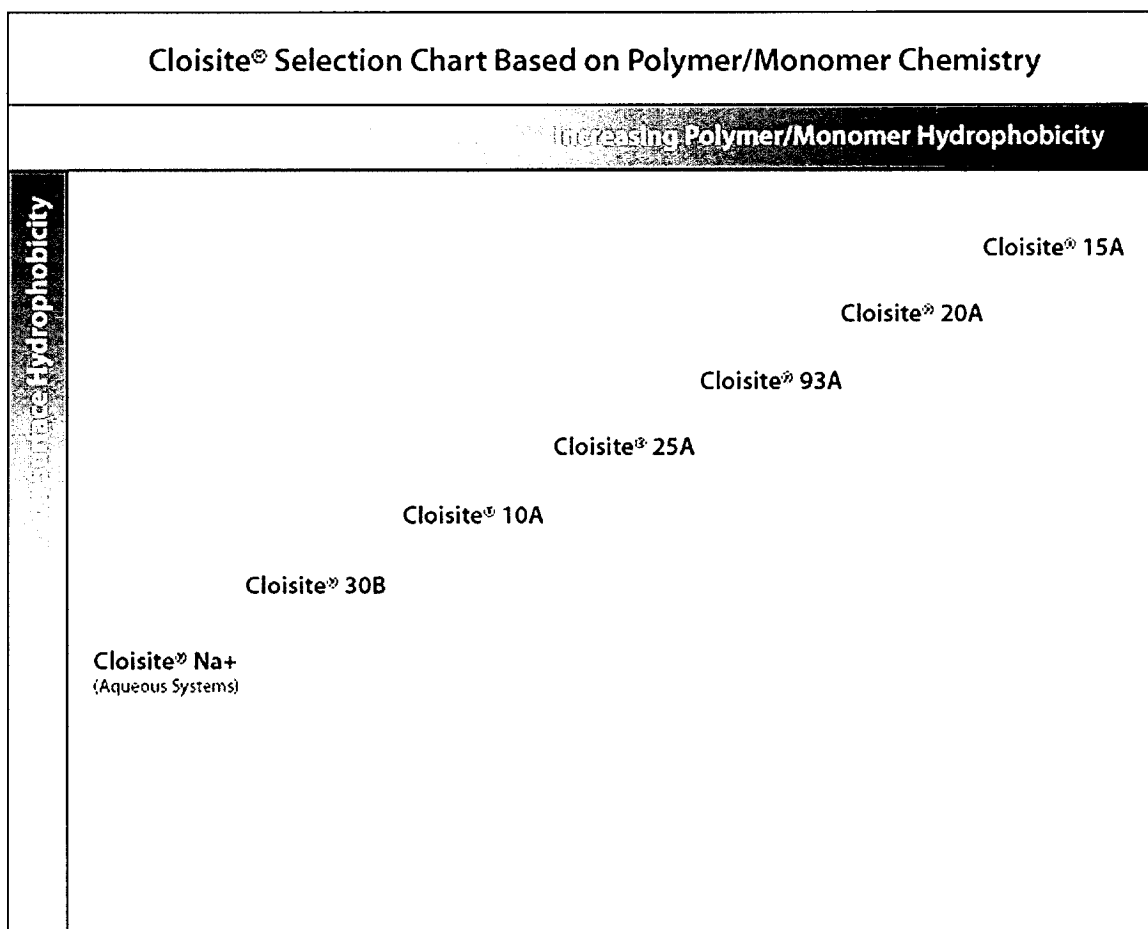


Figure 8. The Cloisite® selection chart of Southern Clay Products, Inc. [21]. Reprinted with permission.

### 2.2.5 Processing

There are at present two principal methods being used commercially to produce polymer-clay nanocomposites: *in situ* polymerization and melt compounding. *In situ* polymerization is applicable to relatively few engineering polymers, such as nylon, polyurethane, and epoxy. This method requires a liquid monomer that can diffuse into the galleries of the organic-modified clays and react with the organic cations present there. The monomers and organic cations interact, resulting in polymerization and

subsequent expansion of the interlayer volumes to form a nanocomposite with intercalated or exfoliated morphology. The rate of polymerization inside the galleries relative to the rate outside the galleries determines the extent of intercalation and exfoliation [8]. The rate of polymerization within the galleries themselves is determined by the ability of the organic cation to catalyze polymerization (in the case of epoxies) or to itself partake in a condensation reaction to form polymer chains (in the case of nylons).

Melt compounding has broader application. It involves mixing, often under high shear, of melted polymer with modified clay. The organic modifier facilitates the diffusion of melted polymer into the galleries. If the combination of changes in entropy and enthalpy due to further diffusion of melted polymer into the galleries is favorable, then the galleries expand to produce nanocomposite. More favorable changes in entropy and enthalpy favor exfoliation of the clay [22]. The extent of intercalation and/or exfoliation is often dependent on the amount of shear produced and the type of organic cation used to modify the clay.

Nylon can be combined with clay to produce nanocomposites by both *in situ* polymerization and melt compounding. A world patent issued to Goettler *et al.* claims that nylon 6 – montmorillonite nanocomposite produced by *in situ* polymerization has superior mechanical properties over the same type of nanocomposite produced by melt intercalation [23]. This claim suggests that the type of process used to produce a nanocomposite affects the properties of the product. The results of each process are not directly comparable if the processes require the clay to be modified with different kinds of organic cations.



VanderHart *et al.* studied montmorillonite – nylon 6 nanocomposites using nuclear magnetic resonance (NMR) [24]. The nanocomposites were produced by melt compounding in a twin-screw extruder. The purpose of the study was to check the feasibility of using NMR to determine the quality of dispersion of nanoclay in a polymer matrix. A surprising result of their work was evidence that the organic cation present on the clay decomposed during processing. In a subsequent study, Davis *et al.* found that nylon 6 also degraded during melt compounding. Dried nylon 6 compounded with dried organoclay degraded much more than dried nylon 6 that was extruded alone [24]. These results have implications: decomposition of an organic cation and/or a polymer during processing will probably affect the resulting interfacial interaction characteristics between the polymer and nanoclay after processing.

From the above reviews, the reader should appreciate how much the factors of morphology, the type of clay, the type of polymer, type of organic cation, and processing interrelate. All these factors can and do affect the interactions between polymer and clay in nanocomposites.

### 2.3 Research Direction and Justification

As described above, the factors that affect the interactions between polymer and nanoclay are many. The factors also interrelate. In studying such a system, good experimental technique involves exerting good control over the factors and limiting the number of factors that are varied in a particular study.

### 2.3.1 Tool Choice: Atomic Force Microscopy

The tools of differential scanning calorimetry, thermal gravimetric analysis, and atomic force microscopy were considered as means of studying the interactions between polymer and nanoclay. Research directions were considered for each of these tools. In the end, the research direction involving the use of atomic force microscopy (AFM) seemed to offer the best control over the many factors that affect the interactions between polymers and nanoclay. It appeared to offer a means to directly measure the interactions between polymers and clays.

A search of the literature suggested that AFM had not yet been used to study interactions between polymers and organically-modified montmorillonite. The literature, though, gave justification for such a study and gives suggestions how it might be done.

### 2.3.2 Hydrophobic Interactions and the Colloidal Probe Technique

Yoon *et al.* used AFM to measure the long-range interactions between glass spheres and silica plates in water [26]. The hydrophobicities of the surface of glass spheres of 30-50 micron diameter and silica plates were varied using solutions containing octadecyltrichlorosilane. The glass spheres were attached to the end of cantilever probes using epoxy. The hydrophobicities of the silica plates were assessed by measuring water contact angles. The hydrophobicities of the glass spheres were assumed to be the same as the silica plates treated using the same octadecyltrichlorosilane solution.

Force measurements using atomic force microscopy were conducted for glass spheres and silica plates of similar and dissimilar hydrophobicities. Figure 9 shows the

measured forces of attraction ( $F/R$ , where  $R$  is the radius of the sphere) as a function of approach distance ( $H$ ) between a glass sphere with a water contact angle of  $109^\circ$  and silica plates with water contact angles ranging from  $0^\circ$  to  $109^\circ$ .

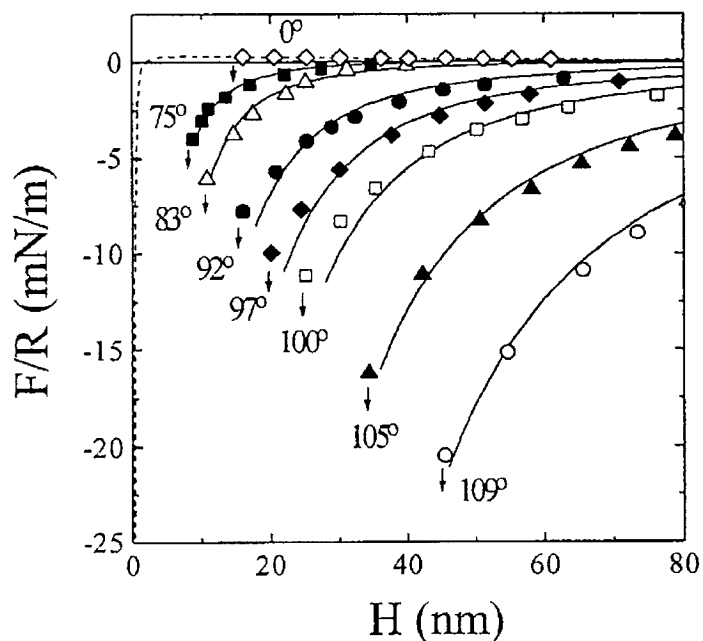


Figure 9. Measured long-range interaction force as a function of distance between a hydrophobic glass sphere and silica plates of various hydrophobicities as they approached each other in water [26]. Reprinted with permission. Copyright 1997 Elsevier.

The most hydrophobic glass sphere ( $109^\circ$  water contact angle) and the least hydrophobic silica plate ( $0^\circ$  water contact angle) showed very little interaction. In contrast, the silica plate with the same hydrophobicity ( $109^\circ$  water contact angle) as the glass sphere showed significant interaction.

The method that Yoon *et al.* used to measure interaction forces is known as the “colloidal probe technique.” The name derives from the fact the technique uses an AFM probe with a small particle attached to it. The word “colloidal” is a misnomer, in that the

particles that are usually attached to probes are usually greater than one micron in diameter – larger than a colloid. Nevertheless, the technique is useful. When the particle on a probe interacts with a surface, the atomic force microscope detects the interaction. The detected interaction can be measured, and can be converted into a force. The results of Yoon *et al.* suggest that the colloidal probe technique can be used to measure and compare the interactions between organically-modified montmorillonite and polymers of similar and dissimilar hydrophobicities.

### 2.3.3 Interaction Forces of Montmorillonite and Organic Polycation

Szücs *et al.* used the colloidal probe technique to measure the interaction forces between a montmorillonite and the polycation polydiallyldimethylammonium chloride (PDDACl) in water [27]. For sample preparation, PDDACl was self-assembled from aqueous solution onto flat silicon wafers and onto twelve-micron diameter silicon spheres epoxied to AFM probes. Depending on the experiment, the montmorillonite from aqueous solution was then self-assembled onto either the PDDACl-coated spheres or onto the PDDA-coated wafers; it did not self-assemble directly onto silicon. See Figure 10 for typical images of PDDACl and montmorillonite coatings on wafers. Szücs *et al.* reported root-mean-square (RMS) roughness values for the surfaces shown in Figure 10 as being 0.57 nm RMS for PDDACl and 1.23 nm RMS for monomorillonite. Interactions were measured between PDDACl-coated wafers and montmorillonite-coated spheres, and alternatively between montmorillonite-coated wafers and PDDACl-coated spheres.

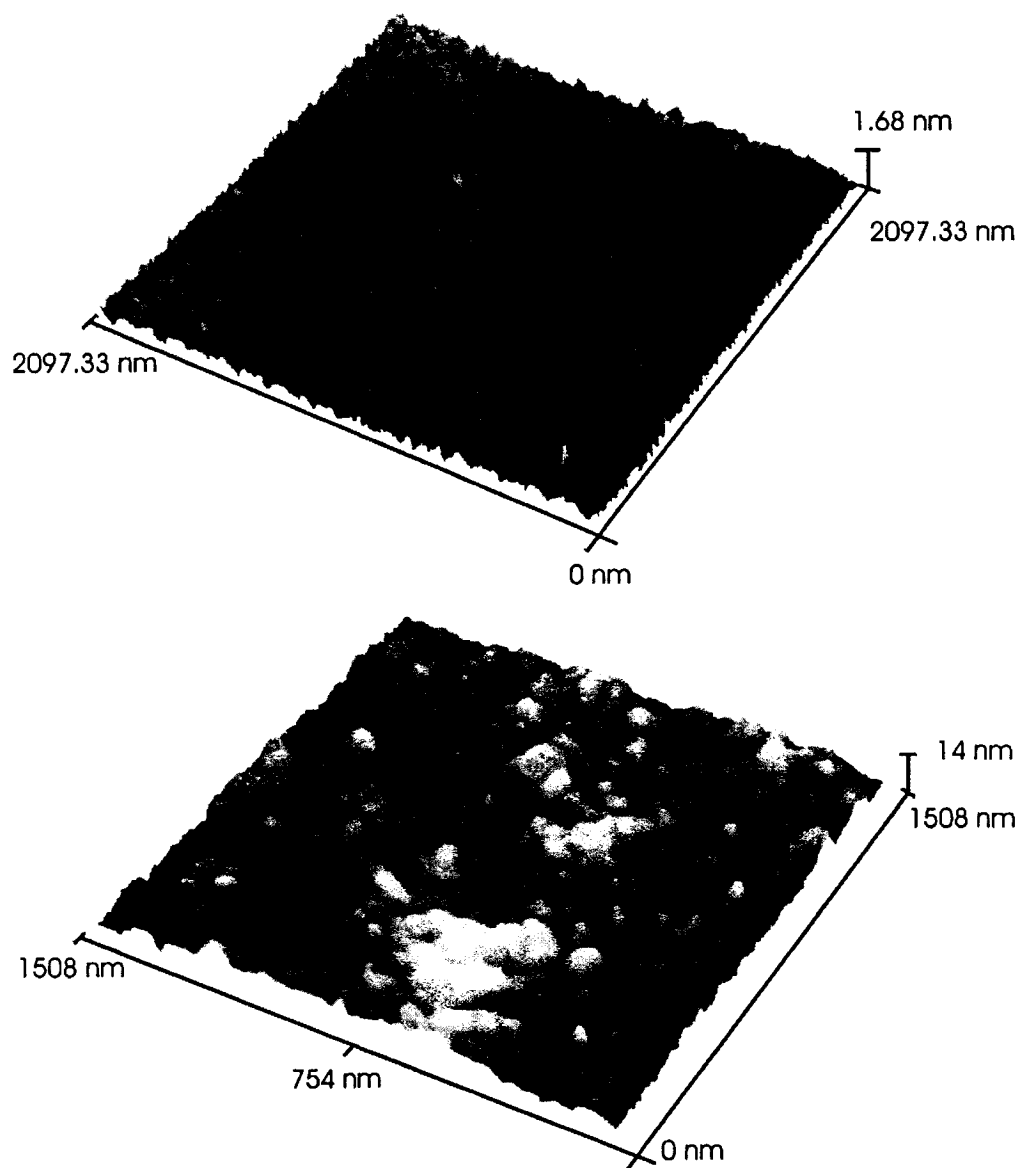


Figure 10. AFM images of PDDACl self-assembled onto a silicon wafer (top) and montmorillonite self-assembled onto a PDDACl-coated silicon wafer (bottom) [27]. Reprinted with permission. Copyright 2001 American Chemical Society.

Szücs *et al.* endeavored to measure the long-range interaction, but due to problems with data interpretation they only reported where the interaction began. They reported that the interaction began at 125 nm for an approaching PDDA-coated wafer and

a montmorillonite-coated sphere, and began at 156 nm for an approaching montmorillonite-coated wafer and a PDDACl-coated sphere.

Szücs *et al.* obtained a value for the adhesive forces by continuing the approach of coated wafer and sphere until they came into physical contact, and then measuring the force required to separate them. For a PDDA-coated wafer and a montmorillonite-coated wafer, they reported an adhesive force of -65 mN/m, where the force in milliNewtons is normalized to the radius of the silicon sphere on a probe in meters. They reported that the adhesive value for a montmorillonite-coated wafer and PDDACl-coated sphere was -70 mN/m, but that the latter combination of wafer and sphere produced data that was less reproducible.

Szücs *et al.* also measured the adhesive forces between silicon and silicon, between silicon and PDDA, between PDDACl and PDDACl, and between montmorillonite and montmorillonite. They wrote that the adhesive force between montmorillonite and PDDACl was the strongest one measured, which was expected since montmorillonite and PDDACl are oppositely charged.

The technique of Szücs *et al.* appears applicable to polymers and organically-modified clays if they can be dissolved in solvents, and then coated onto flat substrates and onto spheres attached to AFM probes. Polymers and organically-modified clays may not coat directly onto spheres and substrates; spheres and/or substrates may need to be coated with another material first. Their observation regarding the reproducibility of data suggests that coating organically-modified clay onto probes may be preferable to coating it onto substrates. Also, Szücs *et al.* had more success measuring adhesive forces than

long-range forces, but adhesive forces are probably of more interest in studying the interaction of nanoclay and polymer in nanocomposites. Long-range forces may be of more interest in studying polymer-clay interactions during intercalation and exfoliation, for improving the production of nanocomposites.

#### 2.3.4 Organoclay Solubility

Ho *et al.* attempted to correlate published data on Hansen's solubility parameters of solvents with estimates of the Hansen's solubility of Cloisite® 15A [28]. The solubility parameter estimate was based on the group contribution method of the functional groups present on the organic cation present in the clay. They used small-angle neutron scattering and wide-angle X-ray scattering to measure the dispersion of Cloisite® 15A in fourteen solvents that had Hansen's solubility parameters similar to the value estimates. They found two solvents that exfoliate Cloisite® 15A. The solvents are trichloroethylene and chloroform.

Two references were found relating to the dispersion of Cloisite® 25A in solvents. Lee *et al.* reported that they dispersed the organoclay in chloroform in preparation for making a polymer-clay nanocomposite [29]. Chang *et al.* reported that they dispersed the organically-modified montmorillonite (OMMT) in dimethylacetamide (DMAC) before casting it on glass plates [30].

The reported facts that Cloisite® 15A and Cloisite® 25A can be dispersed in solvents suggest that these OMMTs can probably be coated onto AFM probes and substrates. If they can be coated, then perhaps they can be studied using the colloidal probe technique.

### 2.3.5 Quantitative Equivalence between Polymer Films and Nanocomposites

A paper by Bansal *et al.* proposes that polymer nanocomposites in which the polymer and nanofillers do not interact are quantitatively equivalent to free-standing, planar polymer films, and that polymer nanocomposites in which the polymer and nanofillers do interact are quantitatively equivalent to polymer films that are sandwiched between hard walls [31]. They used differential scanning calorimetry to measure glass transition temperatures of silica-polystyrene nanocomposites containing treated and untreated silica fillers. To show quantitative equivalence, they compared the glass transition temperatures of the nanocomposites to the glass-transition temperature of free-standing and capped polystyrene films.

The proposal of quantitative equivalence gives some credence to the approach of studying the interaction of polymers and clays in polymer-clay nanocomposites by the colloidal probe technique. The work of Bansal *et al.* suggests that the nano-scale interactions in polymer nanocomposites can be studied at a larger scale, such as the micron-sized scale of the colloidal probe technique.

### 2.3.6 Models for Adhesive Interaction

Huguet and Barthel describe two models that predict the adhesive interaction between a sphere and a flat surface [32]. They are the Johnson-Kendall-Roberts (JKR) model and the Derjaguin-Muller-Toporov (DMT) model. Both models assume that the sphere and flat surface deform elastically. The force required to pull a sphere off a flat surface is a function of the sphere radius  $R$  and an adhesion work term  $W$ .

$$\text{JKR model: } F = -(3/2)\pi RW \quad \text{Equation 1}$$



$$\text{DMT model: } F = -2\pi RW$$

Equation 2

The pull-off force predicted by the DMT model is 33% greater in magnitude than the pull-off force predicted by the JKR model. The DMT model includes interactions outside the contact zone. Huguet and Barthel describe the two models as the limits of a continuous transition between insignificant and significant non-contact interaction forces. Reitsma *et al.* described the JKR model as being used with larger spheres and elastic materials, and the DMT model being used with smaller spheres and rigid materials [33]. Both models are used to analyze results obtained from the colloidal probe technique.

### 2.3.7 Factors that Impact Adhesion Force Measurements

In a review article on the colloidal probe technique for measuring adhesion, Kappl and Butt named various factors for which the JKR and DMT models do not account [34].

The factors are

- loading force under which a probe and substrate are contacted,
- contact time between a probe and a substrate,
- humidity,
- temperature, and
- surface roughness of the probe and substrate.

Kappl and Butt described the effects of the factors. Loading force can produce non-elastic deformations, which increase contact area. Contact time is related to viscoelasticity of polymers, which is a time-dependent phenomenon that causes contact area and adhesive force to increase with time. Humidity can produce a meniscus of water, resulting in strong capillary forces. At a temperature slightly above the glass-transition temperature of a polymer, the measured adhesive force can be significantly increased by the optimum combination of viscoelasticity and ability to form intimate

contact. Surface roughness results in reduced contact area, reducing the measured adhesive force.

While the atomic force microscopy offers a way to control the factors of morphology, processing, organic cation, clay, and polymer while exploring the interfacial interactions, the colloidal probe technique introduces the factors described by Kappl and Butt. One response to the complications introduced by the colloidal probe technique is to minimize the effect of some factors (such as humidity and surface roughness) and to keep constant the effect of other factors (such as loading force, contact time, and temperature).

#### 2.3.8 Correlations of Adhesive Force

Lee *et al.* measured the rates of fouling of natural organic matter onto a reverse osmosis membrane operating under various solution chemistries [35]. They also used the colloidal probe technique to determine the adhesion force between bulk foulants in the solutions and foulants that had deposited on the membrane. They found a strong, positive correlation between measured fouling rates and measured adhesive forces.

Young *et al.* reported that they used the colloidal probe technique to study the aerosolization of drugs in dry powder inhalers used in drug delivery [36]. They measured the cohesive forces between micronized drug particles of three drug systems, as a function of relative humidity. They compared the measured forces with *in vitro* aerosolization data from a previous study. Through linear regression analysis, they found a correlation with  $R^2$  greater than 0.80. They concluded that the colloidal probe technique is a powerful tool for predicting the *in vitro* aerosolization performance of pharmaceutical aerosols.

In the case of nanocomposites composed of polymers and organically-modified montmorillonite (OMMT), a simple question is whether the adhesive force measured between an OMMT and a polymer is higher if the polymer is one which can be processed with the OMMT to form a nanocomposite. In other words, does an adhesive force measured using the colloidal probe technique positively correlate to the empirically known suitability or non-suitability of an OMMT for forming a nanocomposite with a specific polymer? If so, can the colloidal probe technique be used as a predictive tool in developing new or improved polymer-clay nanocomposites?

#### 2.4 Conclusion of Literature Review

The reviewed literature shows that the properties of organoclay-polymer nanocomposites are affected by morphology, type of clay, type of polymer, type of organic cation, and processing. Additionally, the factors interrelate in that a change in one factor causes or necessitates a change in others. The interrelationship makes the interactions between nanoclay and polymer difficult to study. Atomic force microscopy appears to provide a way to limit the number of factors that are varied in an experiment, using the colloidal probe technique.

The colloidal probe technique has been used to measure interactions between spheres and plates of similar and differing hydrophobicities; the spheres with similar hydrophobicities gave the strongest interactions. The technique has been used to measure the adhesive force between spheres and wafers coated with water-soluble montmorillonite and a polycation. Since solvents have been identified that disperse the organically-modified montmorillonites Cloisite® 15A and Cloisite® 25A, these

organoclays can probably be coated onto probes. Grades of Cloisite® and polymers vary in hydrophobicity. Therefore, the adhesive forces measured between a grade of Cloisite® and several polymers of differing hydrophobicity might vary.

An important question is whether the adhesive force would be greatest with the polymer with which the Cloisite® is known to form a nanocomposite. If the answer is affirmative with several grades of Cloisite®, then the adhesive force measured using the colloidal probe technique can be correlated to the empirically-known suitability of polymer-Cloisite® pairs for forming nanocomposites.

## CHAPTER THREE HYPOTHESIS, OBJECTIVES, AND ETHICS

The hypothesis is presented. Experimental objectives that have the purpose of testing the hypothesis are described. Ethics for performing the work are discussed.

### 3.1 Research Hypothesis

The hypothesis is that the colloidal probe technique can be used on an atomic force microscope (AFM) to study the interfacial interactions between organically-modified montmorillonites (OMMTs) and polymers, and that the adhesive forces measured between different sets of OMMTs and polymers can be positively correlated to the known compatibility of each set for processing into nanocomposites.

This research hypothesis poses two direct questions, and leads to a third, indirect, question:

Question 1. Can the colloidal probe technique be used on an AFM to study the interfacial interactions between organically-modified montmorillonites (OMMTs) and polymers?

Question 2. If the colloidal probe technique is used on an AFM to measure the adhesive force between different sets of OMMTs and polymers, then do the adhesive forces correlate to the known compatibility of some of the sets for processing into nanocomposites?

Question 3. If the adhesive forces correlate to the known compatibility, then what is the value of the colloidal probe technique as a tool for predicting the suitability of OMMTs and polymers, for the development of new or improved polymer-clay nanocomposites?

The first question relates to technical feasibility – whether there are technical challenges which prevent the colloidal probe technique from being used in this application. The second question can only be answered after the first question is answered in the affirmative, and after actually measuring adhesive forces between different OMMT –

polymer pairs. An affirmative answer to the second question would lead to the third question, which relates to economic feasibility – whether the colloidal probe technique can be recommended as a labor-saving or knowledge-enhancing tool for the development of polymer-clay nanocomposites.

### 3.2 Experimental Objectives

The experimental objectives were pursued in order to confirm the hypothesis and evaluate the AFM as a predictive tool, or if the hypothesis was not confirmed, to describe the problems encountered. Eight objectives are described in the sections that follow.

#### 3.2.1 Organoclays and Polymers

The first objective was to select and obtain three OMMTs of varying hydrophobicities and three polymers of varying hydrophobicities. Another requirement was that each OMMT had to be known to form a nanocomposite with one of the three polymers. Three of each were chosen for the purpose of addressing the second question posed by the research hypothesis. Three OMMTs and three polymers resulted in nine possible OMMT-polymer pairs, three of which are able to form a nanocomposite. The number of OMMTs and polymers was limited to three in order to allow a full matrix of nine correlation experiments to be performed.

#### 3.2.2 Solvents

The second objective was to identify and select solvents to disperse the selected OMMTs and to dissolve the selected polymers. The purpose of solvents was to make

dispersions of the OMMTs and solutions of the polymers for coating OMMTs and polymers onto colloidal probes and substrates.

### 3.2.3 Probes and Substrates

The third objective was to identify and obtain two types of AFM probes - conventional AFM probes for scanning the surface of coatings, and colloidal probes for measuring adhesive forces. Both types of probes needed to be compatible with the AFM with which they were used. Colloidal probes also needed to be compatible with solvents present in solutions used to coat the probes.

The objective also included selecting substrates to be compatible with the AFM and the solvents. The key elements for such selection were that the substrates be smooth, suitable in size for the AFM, and unaffected by the solvents.

### 3.2.4 Coating Methods

The fourth objective was to develop techniques for coating OMMTs and polymers onto colloidal probes and substrates. When the research study was proposed, the decision was made to use dispersions of OMMTs and solutions of polymers to coat probes and substrates. The idea was to deposit coatings by wetting the surfaces of probes and substrates and allowing the solvents to evaporate.

### 3.2.5 Confirmation of Coatings on Colloidal Probes

The fifth objective was to confirm the presence of coatings on colloidal probes. In this research study, the presence of a coating of OMMT or a polymer on a colloidal probe was a prerequisite to using the colloidal probe to measure the interaction between

an OMMT and a polymer. The main tools used to confirm the presence of coatings were atomic force microscopy and scanning electron microscopy. Scanning electron microscopy was destructive to the organic molecules in the coatings; therefore it could only be performed after a colloidal probe was used to measure interactions, or in an experiment in which the purpose was to develop a coating technique. Atomic force microscopy was nondestructive. It could be used to confirm the presence of a coating between the time that a probe was coated and the time it was used to measure adhesive interactions.

### 3.2.6 Environmental Factors

The sixth objective was to identify and mitigate the environmental factors that impact the measurement of interaction between OMMT and polymer on an AFM. Some factors affect the properties of the materials on a macroscopic scale, *i.e.* temperature. Other factors are created by the use of the colloidal probe technique, and are localized in their effect at the point of measurement, such as surface roughness.

### 3.2.7 Placement Option for Organoclay and Polymer Coatings

As described in Chapter Two Literature Review, an option exists as to where OMMTs and polymers are placed for interaction measurements. OMMTs can be coated onto colloidal probes and polymers can be coated onto substrates, or polymers can be coated onto colloidal probes and OMMTs can be coated onto substrates. The objective was to choose the combination that is easier to do and/or produces higher-quality interaction data.



### 3.2.8 Adhesive Force Experiments

The final objective was to perform adhesive force measurements between OMMTs and polymers using coated colloidal probes and substrates. If the measurements were repeatable and reproducible, then adhesive forces were to be measured between the three OMMTs and three polymers, for a total of nine measurements. The purpose of the nine measurements was to look for a correlation between measured adhesive forces and the known compatibility of some of the OMMT-polymer pairs for processing into nanocomposites. If adhesive force measurements between OMMTs and polymers were not repeatable and reproducible, then the technical challenges preventing the reliable measurement of interactions between OMMTs and polymers were to be described.

### 3.3 Ethics

The investigation of the colloidal probe technique as a tool to study the interactions between organoclays and polymers might lead to faster development of more and/or better polymer-clay nanocomposites. It might indirectly encourage the adoption of polymer-clay nanocomposites as engineering materials by increasing the number of polymer-clay nanocomposites available to product designers. Widespread use of the nanocomposites in products, though, might result in harm if the nanocomposites or their residues pollute the environment. Polymer-clay nanocomposites might cause harm through a mechanism that is not currently understood. An example of a class of materials which was later found to cause environmental harm is chlorofluorocarbons. Chlorofluorocarbons were used as refrigerants, but they were later found to deplete ozone

in the ozone layer. The potential for harm notwithstanding, a primary motivation for this work is the labor-saving or knowledge-enhancing potential of the colloidal probe technique.

San Jose State University is accredited by the Accreditation Board of Engineering and Technology (ABET). ABET's Code of Ethics of Engineers and the ethics code and practice of San Jose State University were adhered to in this research study.

## CHAPTER FOUR MATERIALS AND METHODS

The materials used in this research study consisted of organoclays and polymers, solvents, and AFM probes and substrates. The methods involved atomic force microscopy and coating of OMMTs and polymers onto probes and substrates.

### 4.1 Organoclays and Polymers

As shown in Figure 8, Southern Clay Products ranks the grades of Cloisite® according to relative surface hydrophobicity. The different grades of Cloisite® contain different types and amounts of organic modifiers. The modifiers are ternary and quaternary ammonium salts. Names of the modifiers and their concentration are shown in Table 2. The Cloisite® grades are listed in order of increasing surface hydrophobicity.

Table 2. Organic modifiers and concentrations in grades of Cloisite® [37].

Cloisite® Grade	Modifier Concentration, meq/100 g clay	Organic Modifier and Type of Anion
30B	90	MT2EtOT: methyl, *tallow, bis-2-hydroxyethyl, quaternary ammonium. Anion: chloride
10A	125	2MBHT: dimethyl, benzyl, hydrogenatedtallow, quaternary ammonium. Anion: chloride
25A	95	2MHTL8: dimethyl, hydrogenatedtallow, 2-ethylhexyl, quaternary ammonium, Anion: methyl sulfate
93A	90	M2HT: methyl, dihydrogenatedtallow, ternary ammonium. Anion: bisulfate
20A	95	2M2HT: dimethyl, dihydrogenatedtallow, quaternary ammonium. Anion: chloride
15A	125	2M2HT: dimethyl, dihydrogenatedtallow, quaternary ammonium. Anion: chloride

\*Tallow is a mixture of straight-chain hydrocarbon consisting of hydrocarbons with 14, 16, and 18 carbon atoms. The Cloisite® product bulletins state that the chain distribution is approximately 65% C<sub>18</sub>, 30% C<sub>16</sub>, and 5% C<sub>14</sub> [37].

Cloisite® 30B, 25A, and 20A were used in the study. These grades had similar modifier concentrations, and the modifier in each grade was a quaternary ammonium ion with aliphatic hydrocarbons. According to Figure 8 in Chapter 2, their relative hydrophobicities are low, medium, and high.

Samples of Cloisite® 25A and 20A were obtained from San Jose State University. A sample of Cloisite® 30B was purchased from Southern Clay Products, Inc. The samples were kept in 125-ml wide-mouth bottles with screw-top plastic caps.

The polymers nylon 6, poly(methyl methacrylate) (PMMA), and polyethylene-graft-maleic anhydride (PE-MA) were used in the study. They were chosen because each is compatible with one of the three selected grades of Cloisite® in forming a nanocomposite. Noda *et al.* reported that they made an exfoliated nanocomposite with nylon 6 and Cloisite® 30B [5]. As described in Chapter Two, Lim *et al.* measured a strong association between an organically-modified montmorillonite (OMMT) and poly(methyl methacrylate) (PMMA). The OMMT was Cloisite® 25A; they made an intercalated nanocomposite with it and PMMA [13]. Koo *et al.* reported that they made a exfoliated nanocomposite with PE-MA and Cloisite® 20A [38].

The polymers were purchased from Sigma-Aldrich Co. The following information was on the labels of the bottles in which the polymers were packaged:

Nylon 6; CAS 25038-54-4,  $C_{12}H_{24}N_2O_3$ ; FW 244.3; d 1.084; 3mm pellets; Tg=62.5° C; Aldrich catalog number 181110-25G.

Poly(methyl methacrylate); CAS 9011-14-7;  $C_9H_{14}O_4$ ; FW 186.2; mp 300° C; typical  $M_w$  996,000 (GPC); Tg (midpoint) 125.0° C; inherent viscosity 1.250; Aldrich catalog number 182265-25G.

Polyethylene-*graft*-maleic anhydride, 0.85% maleic; CAS 106343-08-2; C<sub>8</sub>H<sub>10</sub>O<sub>3</sub>; mp 120° C; d 0.925; melt index 1.50 g / 10 min. (190° C / 2.16 kg, ASTM D 1238); Aldrich catalog number 437204-250G.

The label of the bottle containing the PE-MA did not indicate the percentage maleic anhydride in the polymer. According to the description of the polymer in the Sigma-Aldrich catalog, the content was 0.85%.

#### 4.2 Solvent Selection for OMMTs and Polymers

A test was needed in order to screen solvents for use in dispersing Cloisite® 30B, 25A, and 20A. The Swelling Test was provided by Southern Clay Products [39]:

##### Swelling Test

1. In a 10 ml graduated cylinder fill with solvent to line
2. Weigh 0.2 grams of Cloisite® and gradually add to solvent
3. Cover using parafilm and let sit overnight
4. Take readings

Below are some results using Cloisite 93A. The better swelling solvents give the highest degree of swelling - better for dispersion.

<u>Solvent</u>	<u>Result</u>
Acetone	1.4 ml
Toluene	3.2 ml
Xylene	2.8 ml
Butyl Acetate	1.8 ml
Ethyl Acetate	2.4 ml
Methyl iso-Butyl Ketone	1.8 ml
Methyl Ethyl Ketone	1.8 ml
Mineral Spirits	1.4 ml

The volume of solvent specified in the Swelling Test was scaled down by a factor of 100 in order to minimize solvent usage in the Modified Swelling Test:

##### Modified Swelling Test

1. Weigh 0.02 grams of Cloisite® and place it in a 7 ml scintillation vial.
2. Place 1 ml of solvent in the vial.

3. Cap the vial and agitate it. Allow the vial to stand overnight.
4. Measure the thickness of swelled Cloisite® using a ruler with a mm scale.

Of the solvents screened, the better candidates were compared and judged using a qualitative clarity test, which was developed from the Modified Swelling Test. The Qualitative Clarity Test is as follows.

#### Qualitative Clarity Test

1. Weigh empty 7 ml scintillation vials; record mass of each empty vial.
2. Fill the vials about half full with the solvents.
3. Weigh the vials with the solvents; record the mass of each vial.
4. Calculate the mass of the Cloisite® required for 320 ppm in each vial.
5. Weigh and add the required mass of Cloisite® to each vial.
6. Cap the vials.
7. Place the vials upright in a sonication bath at 50° C for 1 hour.
8. Visually compare the clarity of the dispersions.

An analytical balance was used in all measurements of mass. All the solvents that were used were reagent grade. In order to minimize interference by any residues in the solvents, the minimum Cloisite® concentration used was 320 ppm. The concentration of 320 ppm corresponded to about one hundred times the maximum concentration of residue after evaporation reported on the solvent bottles.

Stock dispersions of 320 ppm and 3200 ppm were made for each of the three grades of Cloisite® used. The dispersions were made and kept in 125 ml Qorpak® wide-mouth bottles with Teflon®-lined caps. Before they were used for coating, they were placed in a sonication bath at 50° C for 1 hour.

Solvents for the three polymers were prescreened by searching the literature for references to each polymer being dissolved in solvents. In order to test the prescreened solvents, one or two grams of each of the solvents were placed in vials. The mass of each

solvent was measured. Then, the corresponding polymer was added to each vial to make a 1 wt% polymer-solvent mixture. The vials were capped.

The vials were allowed to stand overnight at room temperature. The vials containing solvents in which a polymer dissolved were set aside; clearly, the solvents were effective for the polymer; they were considered to be primary solvents.

Each solution in which polymer did not appear to dissolve was, in turn, placed in an oven that had a glass window in the door. The oven temperature was set at least 5° C below the boiling point of the solvent. The heated solution was observed over the course of up to three hours. The vial was removed from the oven after the polymer appeared to dissolve. The vial was allowed to stand at room temperature. It was observed after one hour, two hours, and overnight for the purpose of seeing whether the polymer solution was stable at room temperature or the polymer precipitated. Solvents in which a polymer was stable at room temperature were considered to be primary solvents for the polymer. Solvents in which a polymer precipitated at room temperature were considered to be secondary solvents for the polymer.

Stock solutions of polymers were made in concentrations ranging from 0.1 to 15 wt%. The solutions were made and kept in 125 ml Qorpak® wide-mouth bottles with Teflon®-lined caps.

All glassware used in the project was cleaned using a brush and warm 1 wt% Alconox® solution. The cleaned glassware was rinsed at least three times with distilled water, and dried in a convection oven set at 80° C. The Qorpak® jars were purchased from McMaster-Carr, Inc.

### 4.3 Probes and Substrates

Probes consisted of contact probes for imaging surfaces and colloidal probes for measuring adhesive forces. Substrates consisted of a silicon probe characterization grating and small sheets of mica.

#### 4.3.1 Contact Probes

For imaging of samples by AFM, ten mounted probes were purchased from Pacific Nanotechnology, Inc. of Santa Clara, California. The model number of the probes was P-MCU-SICT-0. The probes were supplied mounted, on 0.450-inch long by 0.100-inch wide metal substrates. Vendor information states that the probes were made from highly-doped silicon to dissipate static charge. Each probe consisted of a cantilever that was 450 microns long by 50 microns wide by 2 microns long. The probes had a reported force constant of 0.2 N/m. The imaging tip at the end of each cantilever was shaped like a pyramid with a height of 10 to 15 microns; the radius at the end of the tip was reported by the supplier to be less than 10 nm. The probes are designed to be used in contact mode. In contact mode, a probe scans across a sample surface at a nearly constant amount of bending of the cantilever toward the surface. In contact mode, a probe is not made to vibrate.

#### 4.3.2 Colloidal Probes

Colloidal probes were purchased from Novascan Technologies, Inc. of Ames, Iowa. The probes were the cantilever type. Novascan mounted borosilicate sphere-



like particles on the ends of the cantilevers. The quantity of colloidal probes purchased and the characteristics of the probes are shown in Table 3.

Table 3. Quantity and characteristics of colloidal probes.

Quant.	Cantilever Manufacturer and Product Name	Material	Coating	Force Constant, N/m	Particle Diameter in Microns
10	Veeco NP-OW	SiN	Au	0.12	10
5	MikroMasch NSC 35	Si	Al	14	10
15	MikroMasch NSC12	Si	none	0.35	10
7	MikroMasch CSC12	Si	none	0.08	10
7	MikroMasch CSC12	Si	none	0.08	5
12	MikroMasch CSC12	Si	none	0.08	5, inset
3	MikroMasch CSC12	Si	none	0.6	5, inset
10	MikroMasch CSC12	Si	none	0.6	5

The first set of ten colloidal probes (Veeco NP-OW) was chosen because it had a force constant of 0.12 N/m. The force constant value was chosen because Szücs *et al.* used colloidal probes with a force constant of 0.12 N/m for measuring interactions between a montmorillonite and a polycation [27]. A ten-micron-diameter particle was chosen because Szücs *et al.* used a twelve-micron-diameter silica particle, and it seemed prudent to choose a slightly smaller particle in case the adhesion between an OMMT and a polymer was greater. A borosilicate particle was chosen because the largest diameter silica particle that Novascan Technologies supplied on colloidal probes was five microns.

The second set, of five colloidal probes, was chosen to have a force constant of 14 N/m because the first set of colloidal probes had a strong tendency to bend downward and jump into contact with surfaces in ambient air, resulting in stiction between the probe and a surface. The stiction made learning to operate an AFM with colloidal probes more difficult. A probe product with an aluminum coating was chosen for the second set

because the gold coating on the first set of probes was too reflective for the light lever on the AFM; the gold coating reflected too much coherent red light to the photo detector, saturating the voltage signal from the photo detector. It turned out that the aluminum coating was also too reflective.

The third set, of fifteen colloidal probes, was chosen because the probe cantilevers were not coated with aluminum. It turned out that although the cantilevers had about the right amount of reflectance for the AFM, the cantilevers produced specular reflections at the boundaries of grain-like structure on the surface or inside the cantilevers. The result was that the probes worked poorly with the AFM.

The fourth set, of seven colloidal probes, worked well with the AFM. Some adhesion-force measurements were obtained between the OMMT Cloisite® 20A and the polymers PMMA and PE-MA. However, the probes had some difficulty associated with them. At the time, it seemed that the best way to confirm the presence of a coating on the ten-micron-diameter borosilicate particle was to scan the particle using a contact probe. Unfortunately, the ten-micron diameter exceeded the vertical scan range of the AFM, which was about eight microns. To scan a ten-micron spherical particle, the tip of the contact probe had to first be placed on top of the spherical particle. Placing the tip on top of the particle was difficult because neither the tip nor the particle were visible through the video microscope on the AFM. The cantilever of the contact probe hid both the tip and particle from view.

The fifth set, of seven colloidal probes, was ordered with five-micron diameter borosilicate particles. The five-micron-diameter particles were within the vertical scan

range of the AFM. Unfortunately, the particles were located at the end of the probe cantilevers. When a particle was scanned, the tip of the contact probe tended to catch on the end of the colloidal probe cantilever. When a tip caught while scanning, the contact-probe tip would sometimes catch and release with sufficient energy to knock the borosilicate particle off the colloidal probe.

The sixth set, of twelve colloidal probes, was ordered with the five-micron diameter borosilicate particles mounted ten to twelve microns from the end of the cantilevers; the borosilicate particles are described in Table 3 as being “inset.” The new inset location solved the problem of a contact probe knocking off a borosilicate particle during scanning. Unfortunately, two problems were encountered. The first problem was a sympathetic vibration that formed between a contact probe and a colloidal probe during a probe-on-probe scan; the vibration rendered the scans useless. It was unknown why the sympathetic vibration did not occur during previous probe-on-probe scans. The second problem was that the 0.08 N/m force constant of the colloidal probes had become too small. The problem was attributed to smoother polymer coatings, which had been developed. It was thought that the smoother coatings significantly increased the adhesive force between a coated probe and coated substrate. The bending of the colloidal probe was too great for the AFM to accurately measure. A probe with a higher force constant was needed.

The seventh set, of three probes, was ordered with a greater force constant – 0.6 N/m. The three probes were ordered to evaluate whether 0.6 N/m was in the right range. The results of a test suggested that it was. At about the same time, an easier way to scan

the borosilicate particles was found in the literature; the easier way involved scanning the colloidal probes over a MicroMasch TGT1 probe characterization grating, which is described below, in Section 4.3.3. Subsequently, the eighth and final set, of ten colloidal probes, was ordered.

Pacific Nanotechnology, Inc. (PNI) mounted all the colloidal probes onto 0.500-inch by 0.100-inch substrates, for use on a PNI Nano-R™ AFM. The chip associated with each probe was attached to a substrate using silver-filled epoxy. See Figure 11 for a photograph. The silver in the epoxy provided a conductive path from the probe chip to the substrate to dissipate electrostatic charge. A few of the probes were mounted using a standard epoxy for better resistance to chloroform. On those probes, PNI laid a carbon track to provide electrical conductivity between the probe chip and the substrate.

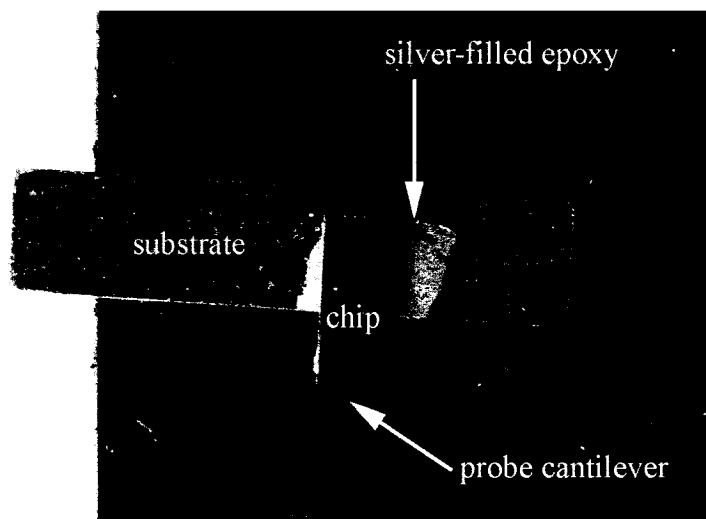


Figure 11. MikroMasch CSC12 probe mounted on a PNI substrate with silver epoxy. Image magnified 6.5 times.

#### 4.3.3 Tip Characterization Grating

A TGT1 tip characterization grating made by MikroMasch of Estonia was purchased from Nanotech America of Allen, Texas. According to a manufacturer's data sheet, the silicon grating consists of an array of sharp tips spaced 2.2 microns apart on a square grid 2 mm x 2 mm in size. The tips are pyramidal in shape, with a tip angle of 30 degrees and height between 0.3  $\mu\text{m}$  and 0.5  $\mu\text{m}$ . The grating was used with colloidal probes, to image the spherical particle that is attached to the probe cantilever.

#### 4.3.4 Mica Substrates

Muscovite, grade V-4, mica substrates were purchased from Supplies Division of Structure Probe, Inc. of West Chester, Pennsylvania. The substrates are 25mm x 25mm square by 0.26mm thick. Mica substrates were reused several times each by cleaving and removing the top layers of mica, revealing a new, smooth surface. The mica substrates were also cut into smaller sizes using scissors.

#### 4.4 Atomic Force Microscopy

The AFM used in the study is a Nano-R™, which was produced by Pacific Nanotechnology, Inc. (PNI) in 2004. The AFM is located at SRI International, a research institute located in Menlo Park, California. The AFM is mounted on an air-cushioned table to minimize vibrations.

##### 4.4.1 Description of the Nano-R™ Atomic Force Microscope.

West and Ross of PNI concisely described what an atomic force microscope is:

The Atomic Force Microscope (AFM) is a scanning probe imaging and sensing device, useful for physical and chemical studies. In its basic configuration, it measures the microscopic surface profile of a near-planar target by mechanically scanning a tiny probe across it in a raster pattern. The probe rises and falls in accordance with the surface profile. As it does so, its position is sensed and captured digitally. That captured topogram can then be rendered as a photograph-like image, reminiscent of an optical microscope [40].

The main stage components of the Nano-R™ are shown in Figure 12. The stage components, indicated as “motorized X-Y positioning” and “Z approach motor (1 of 3)” allow a sample located on a sample puck to be moved in the horizontal X and Y and vertical Z dimensions, relative to a probe mounted on the AFM scanner head. The magnitude of movement is in the range of microns to millimeters. The stage movements constitute the course adjustments of the instrument. Course adjustments are made in preparation for obtaining data, by bringing an area of interest on a sample in close proximity to a probe. The position and relative movement of the sample to the probe is observed by looking at the sample puck and stage, and by looking at the display of the video microscope.

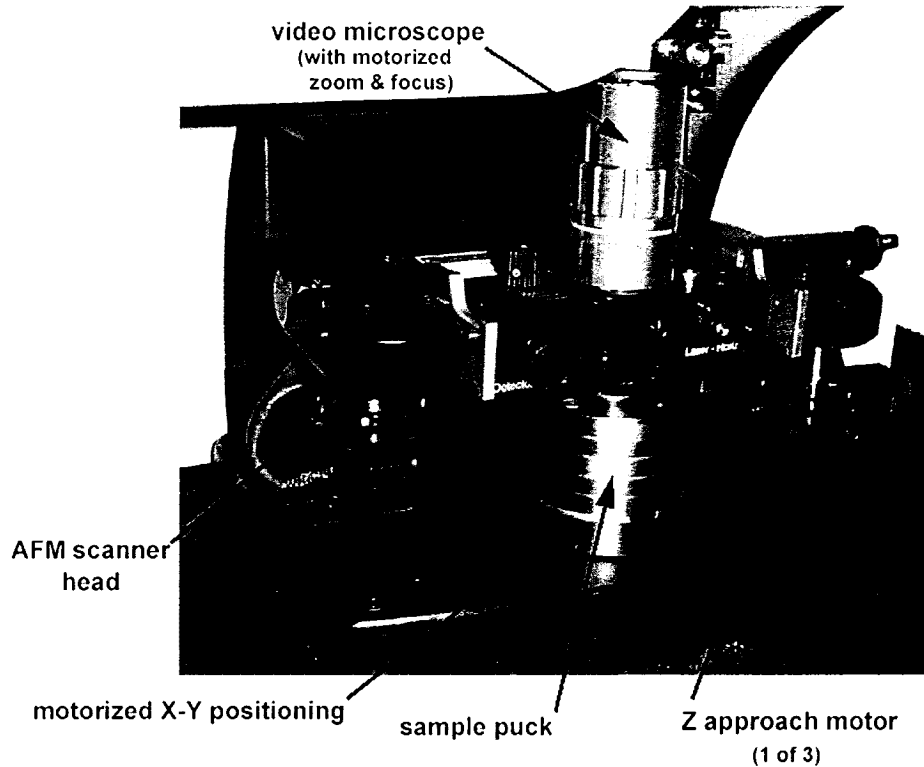


Figure 12. Stage components of PNI Nano-R™ atomic force microscope [41]. Reprinted with permission.

A probe is located on the scanner head. The scanner head contains a piezoelectric actuator, which moves the probe a maximum of 100 microns in the two X and Y horizontal dimensions, and maximum of eight microns in the Z vertical direction. The instrument uses the piezoelectric actuator to move the probe relative to the sample during scanning. Figure 13 shows a Nano-R™ with the sample puck removed and the middle portion of the scanner head rotated into the probe exchange position. The probe exchange position allows easy access to the probe mount. The probe mount is magnetic; it holds onto the steel substrate, to which the probe base has previously been attached by epoxy. A probe, with its substrate, is installed on and removed from the probe mount

using tweezers. When a probe is not in use, it is stored on a magnetic strip inside a plastic container.

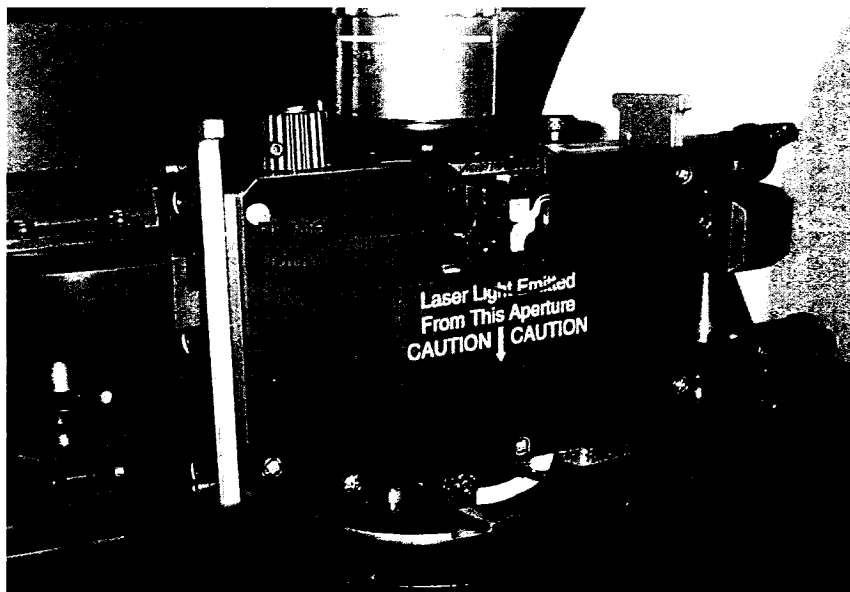


Figure 13. Probe exchange position of Nano-R™ scanner head, showing the probe mount [42]. Reprinted with permission.

The scanner head contains a light lever system for measuring the deflection of the cantilever of a probe as the tip of the probe interacts with a sample surface. The system is depicted in Figure 14. Coherent red light from a low-power laser is directed to the back of the probe cantilever. The light reflects to a photo detector, which is bifurcated into four sections. As the probe tip interacts with the surface, the cantilever bends in vertical deflection and/or torsion. As the cantilever bends, the position of the light spot on the photo detector moves. Movement of the light spot changes the relative amount of light that the bifurcated sections receive relative to each other. The difference in amount of light produces two voltage signals, which are proportional to the amount that the probe cantilever bends. The voltage signals are Z(ERR) and Z(LR). Z(ERR) provides a measure of how much the cantilever bends up and down. Z(LR) provides a measure of



how much the cantilever twists in torsion. The voltage signals provide the instrument with feedback for controlling the height of the cantilever above the sample surface. The voltage signals also provide data to the user.

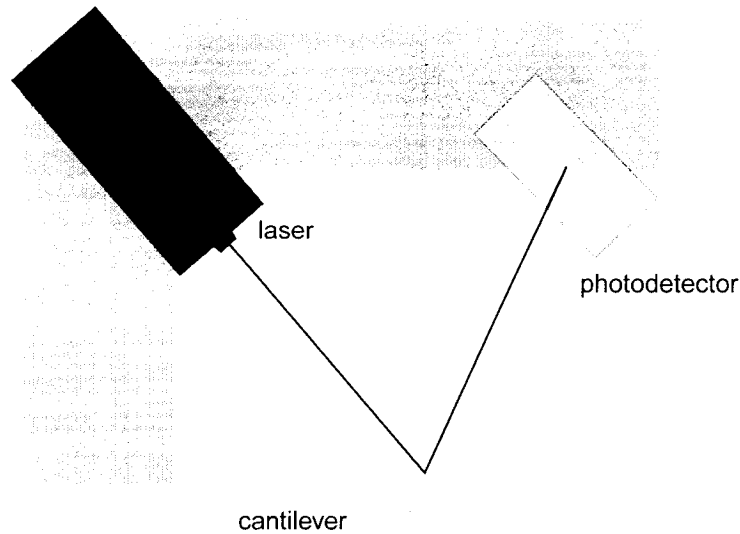


Figure 14. Light lever system for measuring the deflection of a probe cantilever [43]. Reprinted with permission.

The laser and photo detector are aligned after a probe is installed on the scanner head. The positions of the both the laser and the photo detector are adjustable. The laser spot can be physically placed anywhere on a probe's cantilever, but it is generally placed near the end to maximize the change in signal that occurs when the cantilever bends or twists. The detector signal intensity  $V(\text{SUM})$  must be between 0.8 Volt and 5 Volts, which means that the reflectivity of the surface of probes cannot be too low or too high.

#### 4.4.2 Environmental Cell

An environmental cell can be installed on the Nano-R™. The environmental cell consists of a special sample puck, rubber diaphragm, and special probe mount. The

special sample puck and special probe mount replace the usual sample puck and probe mount. When it is installed, the environmental cell allows AFM measurements to be conducted in other media (besides ambient air). In this study, adhesive force measurements between colloidal probes and substrates were conducted with the environmental cell installed. The measurements were conducted in dry, high-purity nitrogen gas.

The environmental cell was tested by generating force/distance curves between a new colloidal probe and a freshly-cleaved mica substrate. The adhesive force between a borosilicate sphere and mica is a strong function of the water-film thickness on the surfaces, which is a function of humidity. The force/distance curves showed a continuous decline in adhesion after the flow of nitrogen gas was started. The removal of water vapor from the cell appeared to be complete after thirty minutes; the force/distance curves stopped changing.

#### 4.4.3 Reverse Imaging of Particles on Colloidal Probes

The Nano-R™ was used to image the surface of the borosilicate spheres on colloidal probes, before and after the probes were coated with OMMT. The borosilicate spheres on the probes were five and ten microns in diameter. To image the borosilicate sphere of a colloidal probe, the probe was installed in the AFM on the probe mount and the TGT1 tip characterization grating was placed on double-sided tape on top of the sample puck. The colloidal probe was scanned over a five micron by five micron area of the TGT1 grating, producing several reverse images of the sphere as the sphere moved

over several of the sharp tips on the grating. The reverse imaging technique is described by Nieto and Craig [44].

Figure 15 depicts two five-micron diameter spheres on top of a TGT1 grating. The sphere on the left side is centered over one tip. If the sphere was attached to a probe cantilever, then the interaction between the surface of the sphere and the tip would be transferred to the cantilever. The cantilever would bend, producing a measurable signal in the light lever system. Moving the probe in a raster pattern would produce an image of the surface of the sphere until the sphere came in contact with a second tip, as depicted by the sphere on the right side. At that point, the second tip would take over and another image of the surface of the sphere would be produced as the AFM continued to move the probe in the raster pattern.

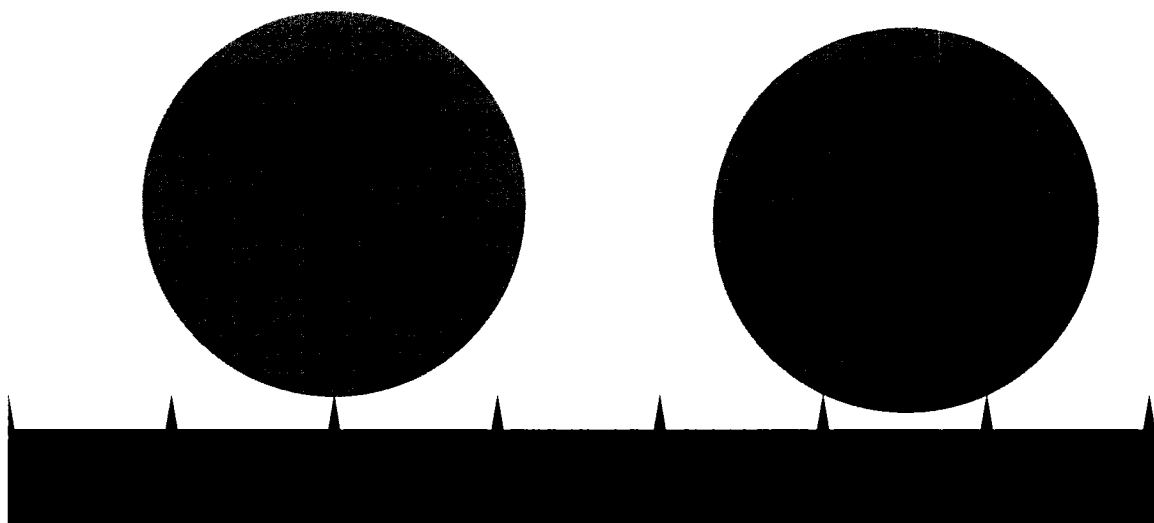


Figure 15. Representation of 5-micron diameter spheres over TGT1 grating, to scale.

Scans on the Nano-R™ are performed using the SPM Cockpit software provided with the AFM. Figure 16 shows a screen copy of the Scan Image window obtained by

scanning a colloidal probe with a five-micron-diameter sphere over the TGT1 grating. The probe was previously coated with an OMMT. The main controls used in scanning were scan size in microns and scan rate in Hertz. The scan-rate setting controls the time in which one scan line occurs. Each scan line consists of a forward and reverse scan. In the example, the scan-rate setting of 0.6 Hertz and resolution setting of 256 required 256 forward and 256 reverse scans, each taking 1.67 seconds (inverse of 0.6 Hertz); the total required scan time was 853 seconds, or fourteen minutes.

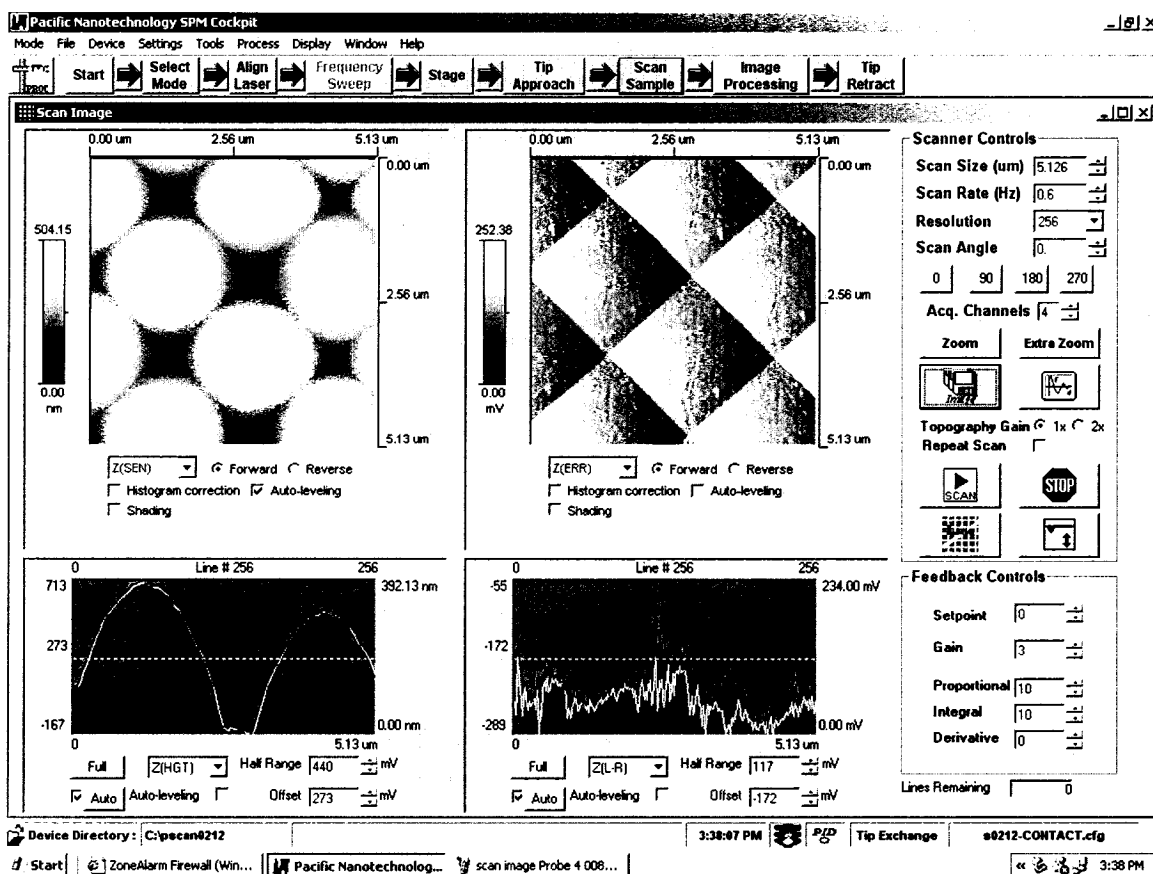


Figure 16. Scan Image window in the Nano-R™ SPM Cockpit software, obtained by scanning a colloidal probe with a five-micron-diameter sphere over a TGT1 tip characterization grating.

Four data channels were acquired when scanning. The data channels were Z(ERR), Z(LR), Z(HGT) and Z(SEN). Z(ERR) and Z(LR) are obtained from the photo detector on the light lever system; the milliVolt values indicate the amount that the probe cantilever bends and twists. Z(HGT) and Z(SEN) provide an estimate of sample elevation, based on the signal that the feedback controller sends to the piezoelectric actuator to maintain a range of interaction between the probe and the sample on the sample puck. Z(HGT) and Z(SEN) differ in that Z(SEN) is corrected for non-linearity in the response of the piezoelectric actuator. The data from Z(ERR) and Z(SEN) were used the most; Z(ERR) was used to obtain information on the texture of surfaces, and Z(SEN) was used to obtain information on the topography of surfaces. The upper two windows in Figure 16 display the scan data from Z(ERR) and Z(SEN). Z(SEN), the upper left window, shows that the spherical form of the borosilicate particle on the colloidal probe. Z(ERR), the upper right window, shows the texture of the surface of the borosilicate particle.

In the upper two windows in Figure 16, the tile-like pattern corresponds to the regular spacing of the tips on the TGT1 grating. According to the manufacturer, the tips are arranged in a square grid, 2.12  $\mu\text{m}$  apart. Therefore, scanning colloidal probes over the TGT1 yielded scans of the borosilicate particles that were approximately 2.12  $\mu\text{m}$  in size. The colloidal probes purchased later had borosilicate particles five microns in diameter instead of ten microns. Switching to a diameter of five microns caused a greater portion of the particles on the colloidal probes to be scanned using the TGT1.

The Z(SEN) data was used to verify the stated diameter of the borosilicate particles on the colloidal probes. Z(SEN) data were exported to a software program named NanoRule+; the program was supplied with the Nano-R™. The data was analyzed in the tool called Line Analysis, for the purpose of doing a section analysis of the spherical borosilicate particle. Figure 17 shows a section analysis, done on the Z(SEN) data obtained in the scan of the coated borosilicate particle depicted in Figure 16. A line was drawn at the widest point of one of the images to obtain a line profile of the curved surface. The line profile was analyzed as a chord, to obtain a horizontal length D in microns and a vertical height Z in nanometers. The values are shown enlarged in Figure 17; they are 1.605 μm and 122 nm, respectively. The chord height Z was converted to microns. Then, the chord length D and chord height Z were used in Equation 3 to calculate the diameter of the coated borosilicate particle.

$$\text{Diameter} = [(D/2)^2 + Z^2] / Z \quad \text{Equation 3}$$

Equation 3 was adapted from an equation described by Nieto and Craig [44]. The value calculated for the diameter of the coated borosilicate particle is 5.4 μm, which is in good agreement with the nominal diameter of five microns.

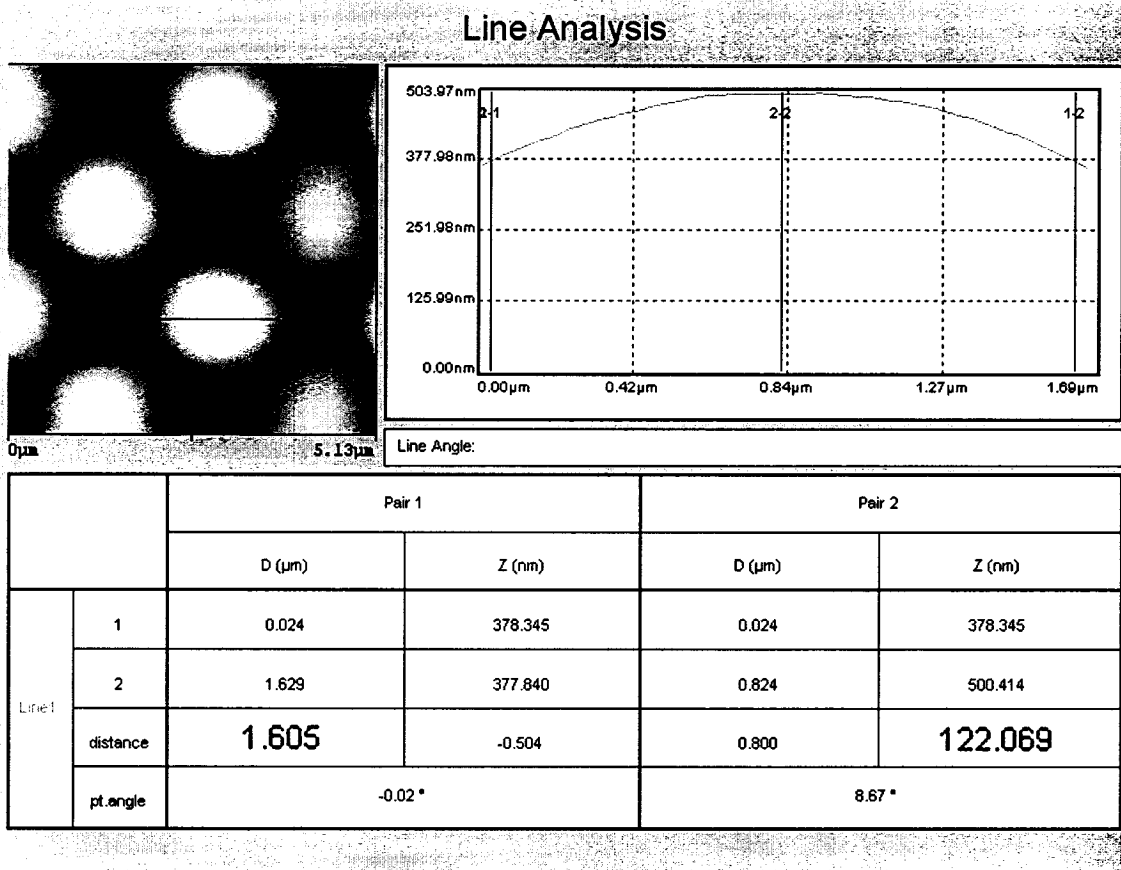


Figure 17. Line analysis on Z(SEN) data, using NanoRule+, for determining the diameter of a borosilicate particle on a coated colloidal probe.

#### 4.4.4 Imaging of Coatings on Mica Substrates

The Nano-R™ was also used to scan OMMT and polymer coatings that had been applied to mica substrates. To scan a coating, a P-MCU-SICT-0 probe was installed on the instrument's probe mount, and a coated mica substrate was placed on a double-sided tape on the sample puck. Scans were performed in the same manner as colloidal probes and the TGT1 grating. The difference was that the sharp tip was located on the probe, and the scanned surface was located on the substrate. The usual goal of such scans was a roughness measurement. To obtain a roughness measurement from a scan, Z(SEN) data

was exported to NanoRule+ and analyzed. Figure 18 shows the result obtained in NanoRule+, using scan data obtained from a coating of nylon 6 on mica. The lightly shaded rectangle within the image is a selected area; the values in the right column correspond to it. For comparisons between coatings, the average roughness values obtained over a ten-micron by ten-micron area were used. Such an area is subsequently referred to as a ten-micron scan area.

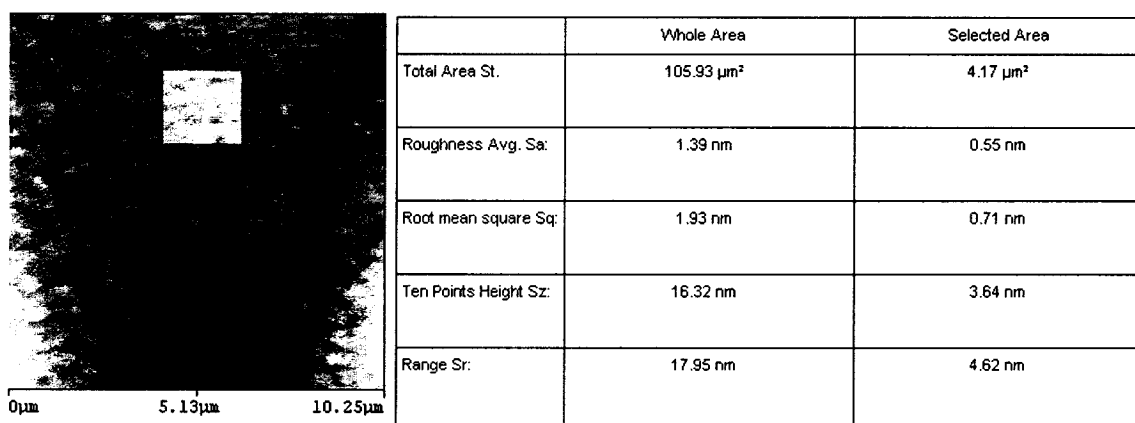


Figure 18. Roughness measurement in NanoRule+, using Z(SEN) scan data obtained from a nylon 6 coating on mica.

Three-dimensional images of Z(SEN) data were also produced in NanoRule+.

Three-dimensional images do not provide any data, but they often give one a better visual sense of a surface.

#### 4.4.5 Force/Distance Curve Technique

Adhesive force measurements were taken between colloidal probes and mica substrates, with the probes and substrates being both coated and uncoated. To perform the experiments, the environmental cell was installed on the Nano-R™. Then, a colloidal probe was placed on the probe mount and a substrate was placed on double-sided tape on



the sample puck. The environmental cell was closed, and a continuous flow of dry, high purity nitrogen gas to the environmental cell was begun. The inlet flow rate was adjusted such that the flow rates from the two outlet ports of the environmental cell were each about 4 ml/s; the flow rates were measured using a 10 ml bubble flow meter. The flow rates were not adjusted during the course of an experiment because it was found that large changes in flow rate caused the height of a probe above a substrate to change; the effect was probably due to pressure-induced strain on mechanical components of the probe mount and/or piezoelectric actuator. The light lever system was aligned with the probe cantilever. Nitrogen was allowed to purge through the environmental cell for 30 minutes before the first adhesive force measurement was taken.

The procedure for taking adhesive force measurements involved first lowering the probe close to the surface of the substrate, bringing the AFM into feedback mode, and doing a scan of the surface. Then, a point was selected in a scan window, which caused the piezoelectric actuator to move the probe over the substrate to the area that corresponded to the selected point. The Force Curve button in the Scan Image window was then clicked, which opened the Force/Distance Curve window.

A force/distance curve is shown in Figure 19. Included in the figure are representations of a colloidal probe during six stages. In stage 1, the piezoelectric actuator moves the colloidal probe toward the surface; the probe approaches, beginning at a distance of eight microns; the probe is too far away to interact with the surface. In stage 2, the spherical particle at the end of the probe has come very close to the surface; attractive force causes the spherical particle to jump into contact with the surface,

bending the probe cantilever downward in the process. The downward bend reduces the voltage of Z(ERR); the reduced voltage appears as a small downward peak. In stage 3, the piezoelectric actuator continues to push the probe closer to the surface; as the probe moves toward the surface, the downward-bent cantilever first straightens and then bends upward. The upward bend increases the voltage of Z(ERR), resulting in an upward sloping line as the probe is pressed onto the surface with continuously increasing force. The piezoelectric actuator stops pushing further when Z(ERR) reaches an upper deflection limit, in this case 2,000 mV.

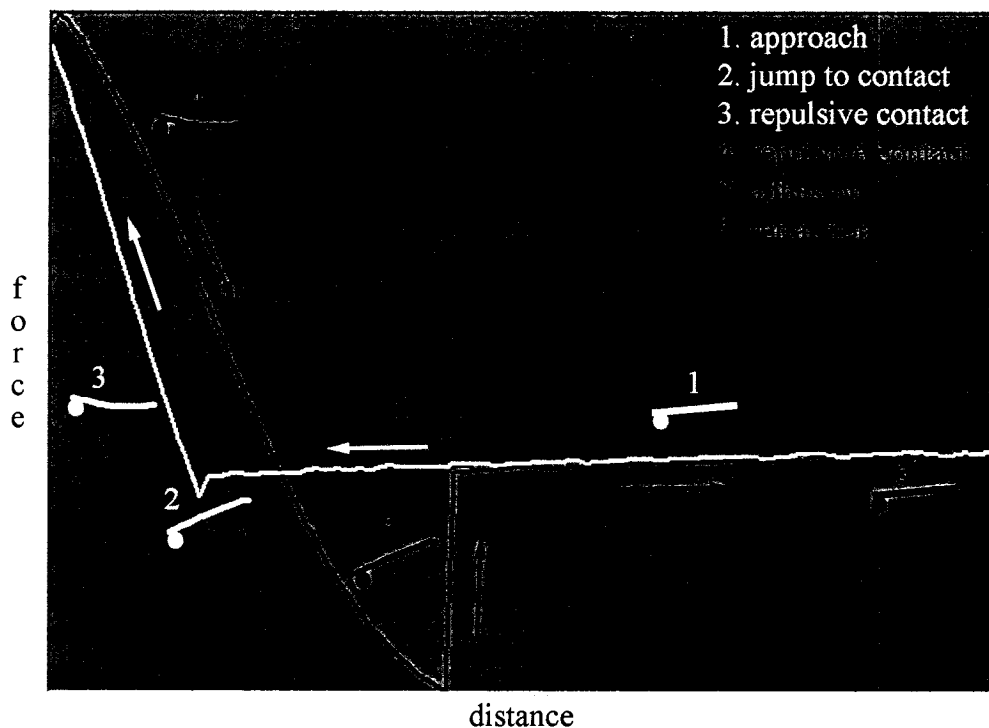


Figure 19. Force/distance curve between a colloidal probe and a flat surface, showing representations of a colloidal probe as it first approaches a surface until it retracts.

In stage 4, the piezoelectric actuator begins to move away from the surface. The force and deflection of the probe continuously reduces. However, the downward sloping

line does not retrace the path of stage 3 because of hysteresis in the piezoelectric actuator. The cantilever straightens until stage 5, when adhesion begins to hold the spherical particle on the surface. The cantilever is bent downward until the cantilever reaction force equals the adhesive force, at which point the downward deflection of the cantilever is at the maximum. Suddenly, the cantilever pulls the spherical particle free from the surface and the cantilever rapidly straightens. At stage 6, the probe is no longer in contact with the surface as the piezoelectric actuator lifts the probe away.

The Force/Distance Curve window does not provide a means to move a probe to a different area of the surface. Subsequent force/distance curves obtained within the same window were considered to be performed at the same spot on the substrate surface. To obtain a force/distance curve in a different area, the window was closed. A different area was selected in one of the scan windows in the Scan Image window. Then a new Force/Distance Curve window was opened.

The main parameters of the force/distance curve are upper deflection limit of  $Z(\text{ERR})$  and the rate at which the piezoelectric actuator moves the probe toward and away from the surface. The parameters affect the magnitude and time of the force that pushes a probe onto a surface. The magnitude and time can affect the magnitude of the adhesive force that results, especially if one of the surfaces is viscoelastic or undergoes plastic deformation [31]. The approach taken in this study was to use the same upper deflection limit and same time rate on every force/distance curve. The value of the deflection limit was 2,000 mV; the time rate was 2.82 s/curve.

The data for each force/distance curve were saved in ASCII files. Microsoft Excel was used to plot the second half of each curve, from step 4 to step 6. The Z(ERR) values in millivolts formed the abscissa of the plot. The corresponding Z(HGT) values in nanometers formed the ordinate; Z(SEN) values are corrected for hysteresis, but they were not used because the Nano-R™ does not record Z(SEN) values in the force/distance curve data files. A value of the adhesive force in nanoNewtons was calculated from each data set.

There are two methods that can be used to calculate the adhesive force from force/distance curve data obtained on a Nano-R™. One method involves using Z(ERR) – the voltage signal from the light lever system that relates to the amount and direction that a probe cantilever is deflecting. Four values of Z(ERR) in a force/distance curve data set are identified:  $Z(ERR)_{\text{baseline}}$ ,  $Z(ERR)_{\text{min}}$ , and two values used to calculate the slope  $\Delta Z(\text{HGT})/\Delta Z(\text{ERR})$ .  $Z(ERR)_{\text{baseline}}$  is the value corresponding to the zero-deflection baseline that occurs after the spherical particle releases from the surface.  $Z(ERR)_{\text{min}}$  is the value corresponding to the maximum point of downward deflection of the probe cantilever – the point at which the spherical particle is about to release from the surface. For calculation of the slope  $\Delta Z(\text{HGT})/\Delta Z(\text{ERR})$ , two values of Z(ERR) with corresponding values of Z(HGT) are chosen from an area of constant slope in the repulsive-contact region of the force/distance curve. The adhesive force is calculated by subtracting  $Z(ERR)_{\text{baseline}}$  from  $Z(ERR)_{\text{min}}$  and multiplying the result (called “pullback voltage”) by  $\Delta Z(\text{HGT})/\Delta Z(\text{ERR})$  and the force constant of the probe. See Figure 20 for

an example of an adhesive-force calculation using Z(ERR) values; the example is above the baseline of the plot in Figure 20.

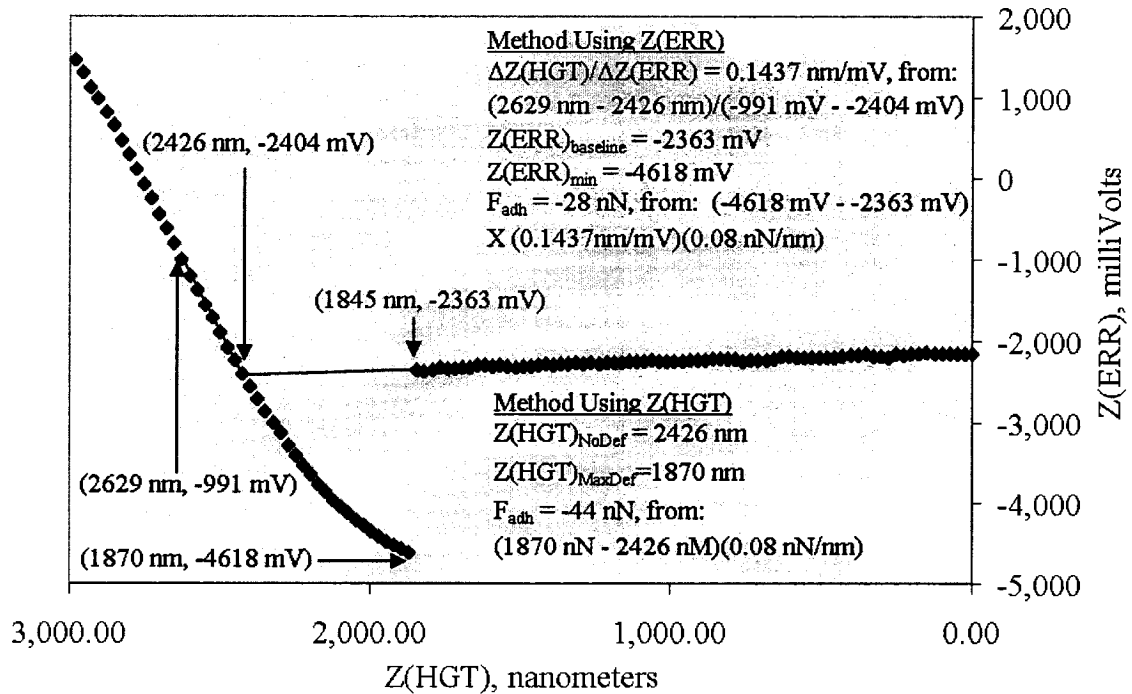


Figure 20. Plot of the retraction portion of force/distance curve data, including calculation of the adhesive force  $F_{\text{adh}}$  using two methods. The plot and Figure 19 are from the same data source.

The other method of calculating the adhesive force involves using Z(HGT) – a data value that corresponds to the distance that the piezoelectric actuator is extended. Two values of Z(HGT) in a force/distance curve data set are identified –  $Z(\text{HGT})_{\text{NoDef}}$  and  $Z(\text{HGT})_{\text{MaxDef}}$ . The value  $Z(\text{HGT})_{\text{NoDef}}$  corresponds to the beginning of the adhesion portion of the force/distance curve, where the cantilever deflection switches from positive to negative. Determining  $Z(\text{HGT})_{\text{NoDef}}$  requires extrapolating the baseline to find an intercept. The value  $Z(\text{HGT})_{\text{MaxDef}}$  corresponds to the point of maximum negative cantilever deflection of the force/distance curve. To calculate adhesive force,

$Z(\text{HGT})_{\text{NoDef}}$  is subtracted from  $Z(\text{HGT})_{\text{MaxDef}}$ ; the result is called “peak width.” It is multiplied by the force constant of the probe cantilever. See Figure 20 for an example of an adhesive-force calculation using  $Z(\text{HGT})$ ; it is located under the baseline of the plot in Figure 20.

The values of the adhesive force calculated by the two methods in the example are significantly different. The value calculated using  $Z(\text{ERR})$  was -28 nN; the value calculated using the  $Z(\text{HGT})$  was -44 nN. The large discrepancy is believed to be due to a nonlinear response of  $Z(\text{ERR})$  at significant downward deflections of a probe cantilever. The slope of the line in the adhesion region can be seen to decrease in Figure 19 and Figure 20. Extrapolating a linear response of  $Z(\text{ERR})$  in the adhesion region gives a value for  $Z(\text{ERR})_{\text{min}}$  of roughly -6,000 mV. Recalculating the adhesive force gives a value of -42 nN, which is close to the value of -44 nN calculated using  $Z(\text{HGT})$ .

Not only is the response of  $Z(\text{ERR})$  nonlinear, it also depends on the location of the laser beam on the probe cantilever. An experiment was performed in which the laser spot was placed at various distances from the end of a colloidal probe cantilever. Force/distance curves were obtained between the colloidal probe and a mica substrate in nitrogen. The retraction curves are plotted in Figure 21.  $Z(\text{ERR})$  is strongly dependent on the location of the laser spot, but  $Z(\text{HGT})$  is not. The peak-width values show little variation. As a consequence of the nonlinear and dependent behavior of  $Z(\text{ERR})$ , the method using  $Z(\text{HGT})$  values was used for calculating adhesive forces from force/distance curves.

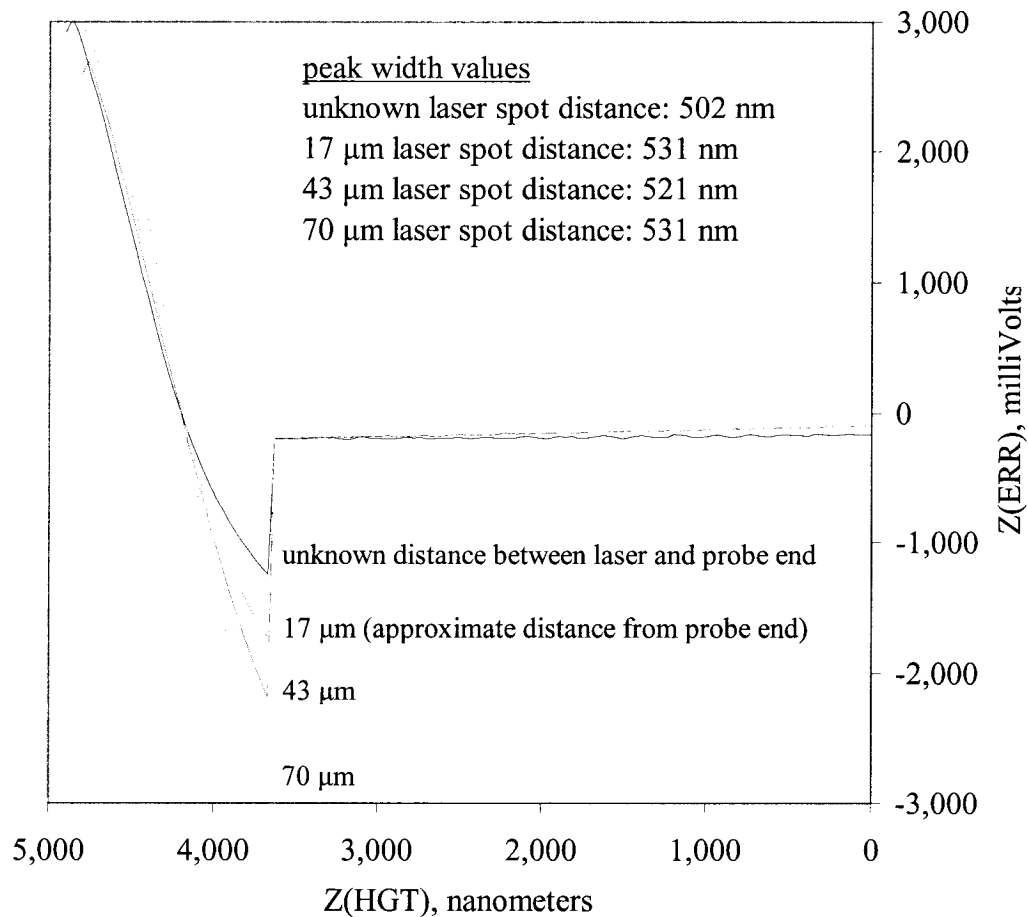


Figure 21. Force/distance retraction curves showing the dependence of  $Z(\text{ERR})$ , and the independence of  $Z(\text{HGT})$ , on laser spot distance from the probe end. The curves were obtained in dry nitrogen between a new colloidal probe and a freshly cleaved mica substrate.

As a consequence of the observed nonlinearity in  $Z(\text{ERR})$ ,  $Z(\text{HGT})$  values were used as the method for calculating adhesive forces from force/distance curves.

Two factors were not included in the calculation of adhesive forces. One factor is that the actual force constant of a probe is not the same as the nominal value reported by the probe manufacturer. Force constants of probes were not measured in this study because they were difficult to measure. The other factor not included in the calculations

is the fact that on AFMs, probes are mounted with a tilt relative to the sample surface. The tilt results in the end of a probe cantilever (where the tip or spherical particle is located) being closer to the sample surface than the beginning of the cantilever (where the cantilever is connected to the probe chip). On the Nano-R™, the tilt is seven degrees. Heim *et al.* reported that the tilt increases the effective force constant of a probe, which reduces the apparent adhesive force. Their experiments with colloidal probes showed that a tilt of 20 degrees decreased the apparent adhesive force by 20 to 30 percent [45]. Tilt was not taken into account with the Nano-R™ because the effect was small.

#### 4.5 Coating Colloidal Probes and Substrates

The general approach taken to coating colloidal probes and substrates with OMMTs and polymers involved a three-step process. First, the OMMTs and polymers were dispersed or dissolved in solvents. Next, the solutions containing the OMMTs and polymers were applied to the surfaces of the colloidal probes and substrates. In the last step, the solvents in the applied solutions were allowed to evaporate, leaving behind coatings of OMMTs and polymers on the colloidal probes and substrates. In the case of coating colloidal probes with OMMTs, an additional step was added. The surfaces of the colloidal probes were pretreated with silane coupling agents by vapor deposition. The colloidal probes were pretreated with silane coupling agents because the colloidal probes had been shipped in gel packs. Gel packs may release hydrophobic vapors, which can deposit onto probe surfaces and render them hydrophobic. Silane coupling agents provided a means of controlling the surface chemistry of the borosilicate particles on the probes.



#### 4.5.1 Coating Colloidal Probes with Organoclays

The primary goals during the coating of OMMTs onto colloidal probes were that the colloidal probes stayed assembled and that the borosilicate particles were actually coated with OMMTs. The secondary goals were that the OMMT coatings on the borosilicate particles were smooth and that any OMMT coatings on the probe cantilevers would have minimal detrimental effects on the light lever system of the AFM when the probes were used.

The technique used to apply an OMMT solution to a probe was rather crude. A probe was grasped using tweezers and then held under the surface of an OMMT solution for twenty seconds. The probe was then placed back onto a magnetic strip in a probe storage container. The lid of the of the storage container was taped somewhat open to assist in evaporation of the solvent. The storage container was oriented in a manner that caused gravity to assist any drops of solution left on the probe cantilever to run down onto the borosilicate particle. The probe was allowed to dry overnight at room temperature. In order to minimize the chance of contamination, it was generally used to obtain force/distance curves on the AFM the next day.

#### 4.5.2 Coating Colloidal Probes with Polymers

PMMA was the only polymer coated onto a colloidal probe. The technique used to apply a PMMA solution to a probe was the same as the technique used to apply an OMMT solution.

#### 4.5.3 Colloidal Probe Coating Simulation Technique

The efficacy of the probe coating technique was tested and refined using pipettes made from borosilicate glass. The tips of new borosilicate pipettes were sealed closed using the flame from a propane torch. Some of the sealed borosilicate pipettes were pretreated with silane coupling agents. The tips of the pipettes were then dip-coated in OMMT and polymer solutions of concentrations being considered for probes. The pipettes were allowed to dry overnight. The next day, the percent coverage or quality of the coating on the dipped lengths of the pipette tips was estimated or compared using a visible-light microscope set at magnification 28. See Figure 21. A black surface located underneath the pipette tip enhanced the visibility of a coating. The black surface was made by marking a piece of tape with a black-ink marker. If a coating was not clearly visible through the microscope, its presence was confirmed by breaking the coating with a razor blade.

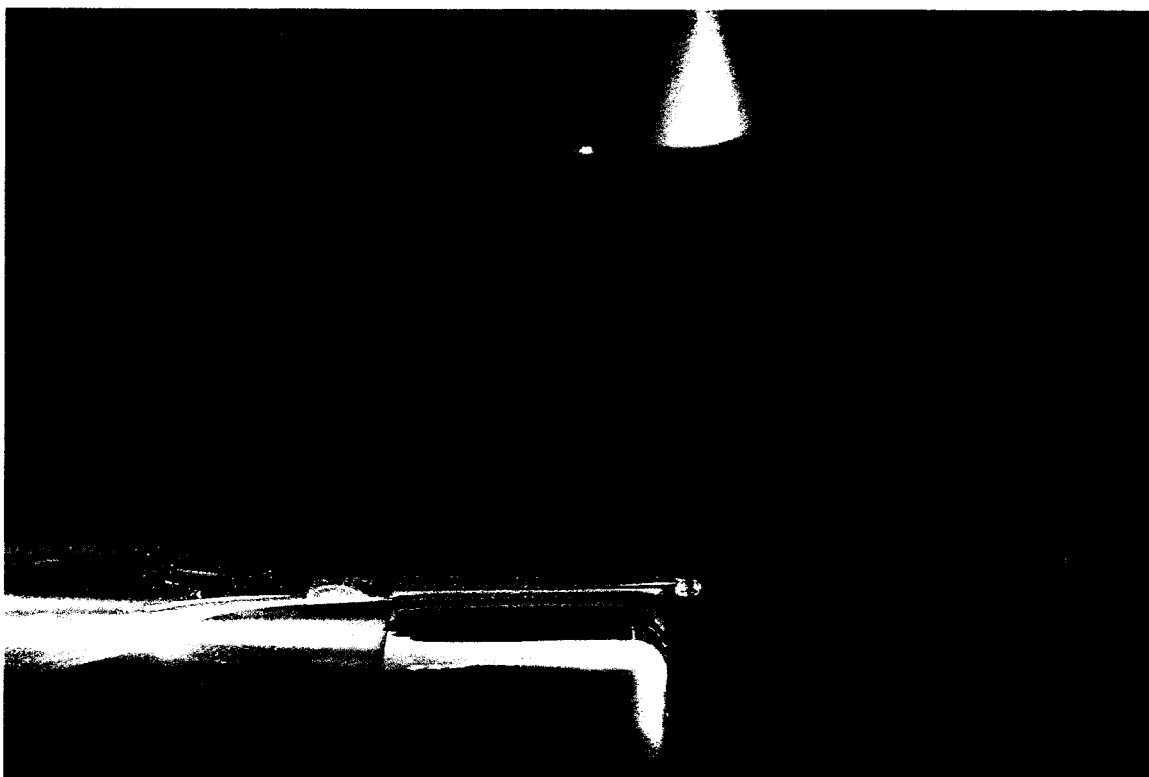


Figure 22. Sealed and coated pipette tip under a visible-light microscope, being side-lit by a lamp.

#### 4.5.4 Pretreating with Silane Coupling Agents

Colloidal probes and borosilicate pipettes were treated with silane coupling agents in a 5.4-liter stainless steel vessel. See Figure 23. The vessel is rated to 140 psig between 20° F and 100° F. The vessel was cleaned with hot 1 wt% Alconox® solution and configured with two quarter-turn valves for purging, and an injection port with a rubber septum for a syringe. To treat an item with a silane coupling agent, the vessel was opened and the item was placed inside with a desiccant cartridge containing a silica gel. The vessel was closed and purged with argon six times. One purge cycle consisted of pressurizing the vessel to 22 psig at one port and then depressurizing to nearly atmospheric pressure at the other port. After purging, the desiccant cartridge was given

fifteen minutes to scavenge any remaining water vapor. A syringe was used to inject 0.4 ml of liquid silane coupling agent, and the vessel was placed in an oven at 60° C for 90 minutes. At the end of the 90-minute period, the vessel was removed from the oven and immediately opened. To cure the silane coupling agent vapor that had deposited on the item, the item was removed from the vessel and placed back in the oven to be exposed to air at 60° C for 30 minutes. After curing, the item was immediately dip-coated with an OMMT solution.



Figure 23. Stainless steel vessel used to apply silane coupling agents to colloidal probes and borosilicate pipettes via vapor deposition.

Two silane coupling agents were used to treat colloidal probes and borosilicate pipettes. Both were purchased from Gelest, Inc. as neat liquids. They were 3-aminopropyltriethoxysilane (APTES) and 3-(2,3-epoxypropoxy)propyltrimethoxysilane

(EPPMS). APTES and EPPMS are reported to produce treated surfaces with critical surface tensions of 37.5 mN/m and 42.5 mN/m, respectively [46]. APTES was used to pretreat probes and pipettes before they were dip-coated in Cloisite® 20A solutions. The Cloisite® 20A solutions used chloroform as solvent. Chloroform has surface tension of 27.5 mN/m [47]; since the surface tension of chloroform is less than the critical surface tension of an APTES-treated surface, it can be expected to wet a APTES-treated surface. EPPMS was used to pretreat probes and pipettes before they were dip-coated in Cloisite® 30B and 25A solutions, which used *n*-methyl-2-pyrrolidone (NMP) as the solvent. NMP has surface tension of 40.7 mN/m [48]. Because of its higher surface tension, NMP does not wet APTES-treated surfaces well. NMP can be expected to wet EPPMS-treated surfaces; the critical surface tension of EPPMS-treated surfaces is higher than the surface tension of NMP.

#### 4.5.5 Coating Substrates with Organoclays

Cloisite® 30B, 25A, and 20A were coated onto mica substrates from NMP and chloroform dispersions. To make a coating from an NMP dispersion, a drop was cast onto a freshly-cleaved mica substrate inside an oven at 100° C. NMP dispersions were cast at 100° C because NMP evaporated very slowly at room temperature. To make a coating from a chloroform dispersion, a drop was cast was cast onto a freshly-cleaved mica substrate at room temperature in open air or inside a drop-casting chamber. The drop-casting chamber was used to slow the evaporation of chloroform, which evaporated quickly at room temperature. It was thought that reducing the evaporation rate would produce smoother coatings.

The drop-casting chamber consisted of an inverted one-liter polyethylene beaker and a glass plate. To make a coating, a mica substrate was first placed on the glass plate. A measured amount of liquid chloroform was placed next to the mica substrate in a container. The beaker was placed over both the mica substrate and the container of chloroform. The chloroform in the container was allowed to evaporate, for the purpose of nearly saturating the air inside the chamber. After the chloroform had evaporated, a pipette containing a small amount of a Cloisite® dispersion was lowered into the chamber. A drop of the dispersion was cast onto the mica substrate. The pipette was withdrawn from the chamber. The Cloisite® precipitated and formed a coating as the chloroform slowly evaporated.

#### 4.5.6 Coating Substrates with Polymers

The three polymers nylon 6, PMMA, and PE-MA were drop cast from solvent solutions onto mica substrates. The primary goal was smooth coatings of the polymers. Smooth coatings of PMMA were found to be easy to make, by casting a solution consisting of 10 wt% PMMA in toluene at room temperature and allowing the toluene to evaporate into ambient air. Nylon 6 and PE-MA presented a challenge. An abstract was which refers to a meeting where Ennis *et al.* presented the results of a study on spin casting polymer films with optimal quality. The abstract refers to a strong correlation between solvent vapor pressure and film quality [49]. After a significant amount of experimentation, it was determined that smooth coatings of nylon 6 and PE-MA could be made by drop casting low concentrations of them in high-boiling solvents at high

temperature in an oven. Experiments and results are discussed are discussed in Chapter Five.

#### 4.6 Safety Precautions

The main hazards associated with performing this study were inhalation of organoclay; ignition of flammable solvents; and breathing, splashing into the eyes, and absorption through the skin of solvents. According to material safety data sheets (MSDS), the Cloisite® samples contained up to 1 wt% crystallized silica (quartz) particles, which can cause lung disease and lung cancer if they are inhaled. To avoid inhalation of Cloisite® during transfers of Cloisite® powders, a NIOSH-approved respirator was worn. Cloisite® powders were transferred in still air.

MSDS indicated that some of the solvents used were poisonous, and some were also carcinogenic. Personal protection gear was worn, namely solvent-resistant gloves and aprons, safety glasses with side shields, and a NIOSH-approved respirator. Transfers of solvents were performed inside a fume hood.

## CHAPTER FIVE RESULTS AND DISCUSSION

The experimental results are presented and discussed in the order in which they were obtained. Generally, later experiments depended on results obtained in earlier experiments. The experiments began with solvent tests on OMMTs and polymers, proceeded with explorations into the intricacies of coating colloidal probes and mica substrates, and ended with the measurement of force/distance curves. Chapter Five ends with suggestions for future work.

### 5.1 Solvent Tests on Organoclays

Solvents were tested on Cloisite® 30B, 25A, and 20A in order to find solvents that disperse the OMMTs for the purpose of coating them onto colloidal probes and/or mica substrates. The solvent tests began with the Modified Swelling Test. The solvent choices for Cloisite® 20A were largely known, since 1,1,1-trichloroethane and chloroform are described in the literature as solvents that exfoliate the similar organoclay Cloisite® 15A. The solvent choices for Cloisite® 30B and 25A were unknowns. Many solvents were tested, especially for Cloisite® 30B.

Results from the Modified Swelling Test are given in Table 4. Only the most notable results are included for Cloisite® 30B; the complete data set is provided in Appendix A. The higher results for the thickness of swollen organoclay are considered better. Not surprisingly, the 1,1,1-trichloroethane and chloroform performed well on Cloisite® 20A; they swelled the OMMT to the point that no supernatant liquid remained in the vials. Only 1,1,1-trichloroethane did as well with Chloisite® 25A. No solvent



swelled Cloisite® 30B to the point where no supernatant liquid remained in a vial; the best two solvents for this most hydrophilic of the three OMMTs were *n*-methyl-2-pyrrolidone (NMP) and dimethylacetamide (DMAC).

Table 4. Results of Modified Solvent Swelling tests on Cloisite® 30B, 25A, and 20A, with thickness of swollen OMMTs measured in millimeters.

Solvent	Cloisite® 30B Thickness, mm	Cloisite® 25A Thickness, mm	Cloisite® 20A Thickness, mm
1,1,2-Trichloroethylene	2	4.6	7 (no supernatant)
1,1,1-Trichloroethane	3.2	7 (no supernatant)	7 (no supernatant)
Acetone	2.7	2.8	2.8
Chloroform	2.8	6	7 (no supernatant)
1,1,2-Trichlorethane	3.7	5	4
Dichloromethane	3.7	5	4
Methyl ethyl ketone	3.3	3.4	2.8
<i>N</i> -methyl-2-pyrrolidone	4.5	-	-
Dimethylacetamide	5.5	-	-

As the next step in solvent testing, dispersions of the OMMTs were made in the best solvents identified in the Modified Swelling Test. The best solvents were evaluated using the Quantitative Clarity Test, in which the clarities of 320-ppm dispersions were compared. For Cloisite® 30B, NMP was the best. The clarity of the dispersion made with NMP was so good that Cloisite® 25A and Cloisite® 20A were also tried. See Figure 24 for a photograph of the dispersions of the three OMMTs in NMP. In the light in which the photograph is taken, the clarity of the dispersions can be compared by looking at the solutions mid-level and toward the left side. Lower clarity appears as a greater amount of light scatter, which appears as white fog in the photograph. From the photograph, it is apparent that the Cloisite® 20A dispersion had the lowest clarity.

The clarity of dispersions of Cloisite® 25A in chloroform; 1,1,1-trichloroethane; NMP; and DMAC were compared (see Figure 25). NMP made the best dispersion,

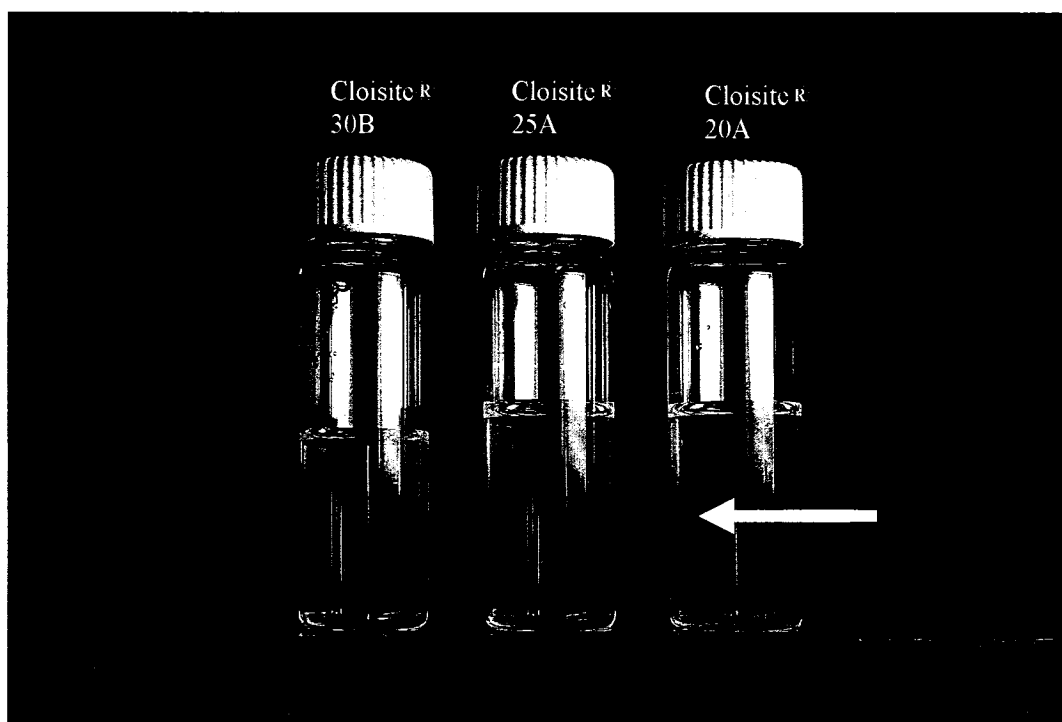


Figure 24. Dispersions of 320 ppm Cloisite<sup>®</sup> 30B, 25A, and 20A in *n*-methyl-2-pyrrolidone. A location showing scattering of light is indicated by the arrow.

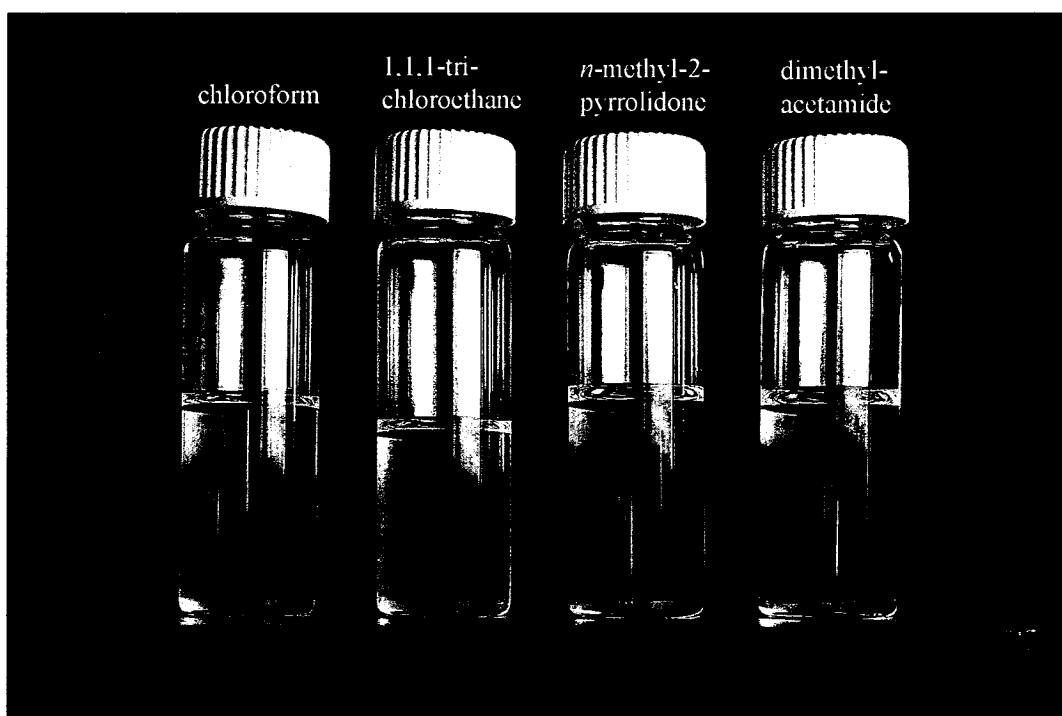


Figure 25. Dispersions of 320 ppm Cloisite<sup>®</sup> 25A in chloroform; 1,1,1-trichloroethane; *n*-methyl-2-pyrrolidone; and dimethylacetamide.

followed by DMAC and chloroform; 1,1,1-trichloroethane made the worst dispersion of the four solvents. DMAC was mentioned in Chapter Two; Chang *et al.* reported that they dispersed Cloisite® 25A in DMAC [30]. It is apparent from the photograph that a portion of the Cloisite® 25A in chloroform was settling to the bottom of the vial.

The clarity of dispersions of Cloisite® 20A in chloroform, NMP, DMAC, dimethylformamide (DMF), and tetrahydrofuran (THF) were compared; see Figure 26. DMAC, DMF, and THF were tested because they are all in some way similar to NMP. Being that NMP performed well on Cloisite® 30B, it was thought that DMAC, DMF, or THF might work as well on Cloisite® 20A. NMP gave the best clarity, followed by chloroform.

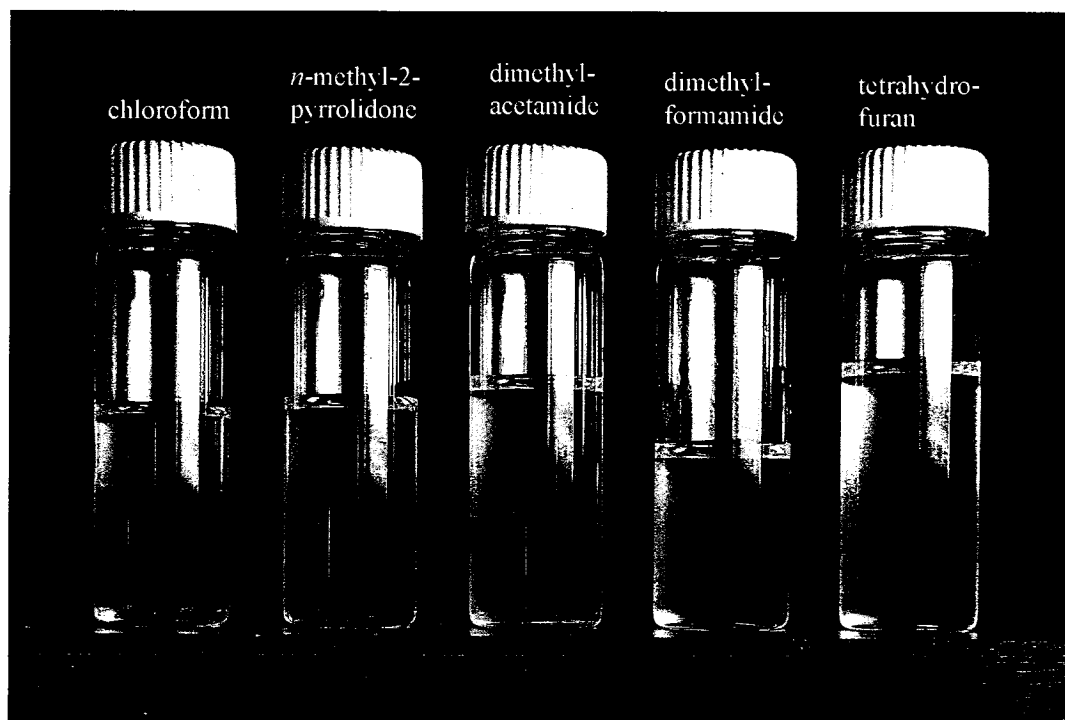


Figure 26. Dispersions of 320 ppm Cloisite® 20A in chloroform, *n*-methyl-2-pyrrolidone, dimethylacetamide, dimethylformamide, and tetrahydrofuran.

In summary, the solvents selected for dispersing organoclays were NMP for Cloisite® 30B, NMP and chloroform for Cloisite® 25A, and chloroform and NMP for Cloisite® 20A. NMP might have been chosen as the solvent for all three OMMTs; chloroform was retained as one of two options for Cloisite® 25A and Cloisite® 20A because it evaporated significantly faster than NMP at room temperature. As will be discussed below, faster evaporation rates can produce smoother coatings.

## 5.2 Solvent Tests on Polymers

Solvents were tested on nylon 6, PMMA, and PE-MA in order to identify the solvents that would be used to dissolve the polymers for coating them onto colloidal probes and/or mica substrates. The results of the tests are given in Table 5.

Table 5. Solvent test results on polymers, giving test temperature and time for dissolution of 1 wt% mixtures, and stability of the solutions at room temperature.

Polymer	Solvent	Solvent Boiling Point	Test Temperature	Observations
Nylon 6	Phenol, liquefied with 9.8% water	182° C [50]	100° C	Dissolved in 2 hours. Stable at 22° C.
Nylon 6	2,2,2-trifluoroethanol	75° C [51]	70° C	Dissolved in 1 hour. Stable at 22° C.
PMMA	Toluene	111° C [52]	22° C	Dissolved in 3 hours. Stable at 22° C.
PE-MA	Toluene	111° C	100° C	Dissolved in 3 hours. Precipitated at 22° C.
PE-MA	<i>O</i> -xylene	144° C [53]	100° C	Dissolved in 3 hours. Precipitated at 22° C.
PE-MA	Cyclohexane	81° C [54]	70° C	Polymer did not dissolve.

Liquefied phenol and 2-2-2-trifluoroethanol were identified as primary solvents for nylon 6. Toluene was identified as a primary solvent for PMMA. Toluene and *o*-xylene were

identified as secondary solvents for PE-MA. No primary solvents were found for PE-MA.

### 5.3 OMMT Coating Experiments on Mica Substrates

Unexpected difficulties were encountered in coating mica substrates with the three OMMTs. In the case of Cloisite® 30B, a 320 ppm dispersion in NMP was found to spread over most of the mica substrate and then flow off one side, since the mica substrate was not perfectly level. It was found that a drop cast 3,200 ppm Cloisite® 30B dispersion tended to stay on a mica substrate. In the case of Cloisite® 25A, an even coating was not produced; instead, clusters formed (see Figure 27). The clusters tended to be sufficiently large in size to be studied by AFM.

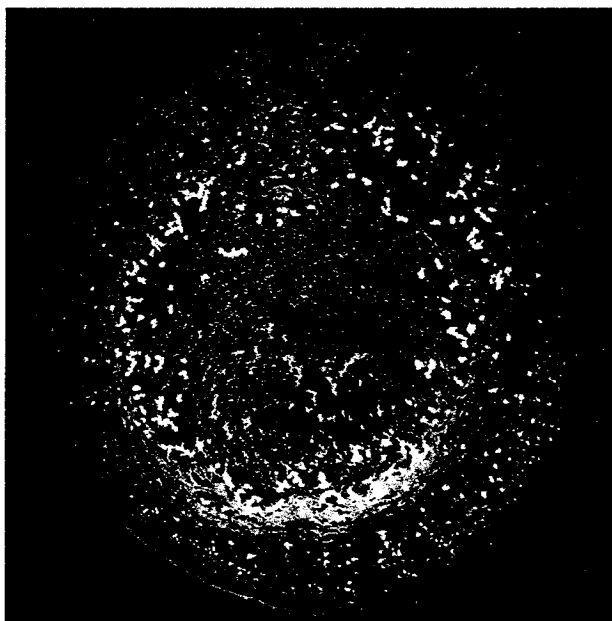


Figure 27. Visible-light photograph of a mica substrate with a dried Cloisite® 25A coating. The coating was made by drop casting a 320 ppm solution in a chamber with 90% chloroform vapor pressure. The image shows many clusters of Cloisite® 25A. The image is magnified 3.2 times.

The coatings that were produced were not as smooth as desired. An effort was made to produce smoother coatings by varying the rate of solvent evaporation, and by varying the concentration of the dispersions. The rate of evaporation of chloroform was slowed by drop casting inside a chamber that contained chloroform vapor at approximately 90% vapor pressure. See Table 6 for conditions at which the OMMTs were cast, and roughness values for each coating. Roughness values were obtained over ten micron scan areas by AFM, after looking for smoother areas by use of the video microscope on the Nano-R™ and by selecting the smoothest area on a 100-micron scan.

Table 6: Root mean square roughness of ten-micron scans of Cloisite® coatings on mica substrates, determined by atomic force microscopy.

Cloisite® Grade	Concentration by Weight, ppm	Solvent	Coating Conditions	Roughness, nm RMS
30B	3,200	NMP	100° C, in air, inside oven	95
25A	320	Chloroform	22° C, in chamber with 90% solvent vapor pressure	32
20A	320	Chloroform	22° C, in air	33 (60 μm scan area)
20A	320	Chloroform	22° C, in chamber with 90% solvent vapor pressure	38
20A	3,200	Chloroform	22° C, in air	38

In comparing the OMMT concentrations, coating conditions, and roughness values in Table 6, it appears that lower OMMT concentrations and faster solvent evaporation tend to produce smoother coatings. The smoothest coating was probably the one cast in air from the chloroform dispersion containing 320 ppm Cloisite® 20A. The roughness value is 33 nanometers RMS for a 60-micron scan area. If the roughness had been measured for a ten-micron scan area, the value probably would have been lower.

A three-dimensional view of a ten-micron scan of the coating corresponding to the last row in Table 6 is shown in Figure 28. The coating and its mica substrate were

used in force/distance measurements. The aspect ratio of the image is ten, which means the vertical relief of the hills and valleys is magnified ten times relative to the horizontal scale. The roughness value of the area is 38 nanometers RMS. Szücs *et al.* reported a roughness value of 1.23 nanometers for a 1.5 micron scan of a coating of montmorillonite as typical [27]. Even accounting their small scan size, the roughness of the organoclay coating is an order of magnitude greater. For example, the roughness of the relatively smooth 1.5  $\mu\text{m}$  by 1.5  $\mu\text{m}$  area in the right corner of Figure 28 was calculated by NanoRule+ to be about 8 nm RMS.

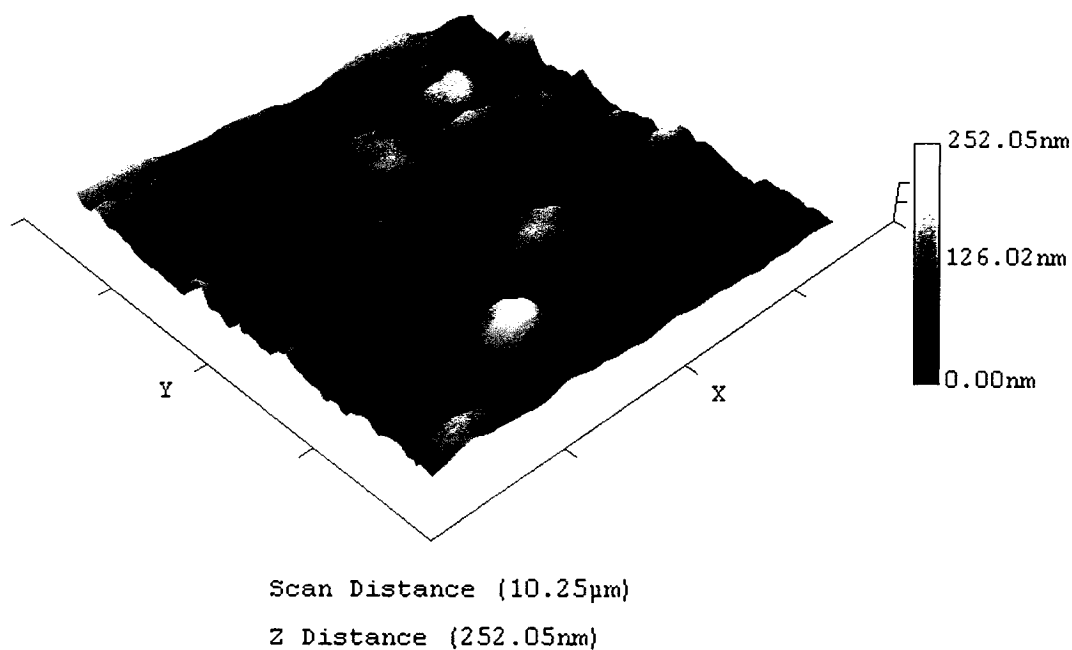


Figure 28. Three-dimensional image of a 10.2  $\mu\text{m}$  AFM scan of Cloisite® 20A coating made by drop casting a 3,200 ppm dispersion in chloroform at 22° C in air. The aspect ratio is ten.

#### 5.4 Polymer Coating Experiments on Mica Substrates

Significant effort was expended in determining how to cast smooth coatings of the three polymers onto mica substrates. The approach taken was to vary solution concentration between 0.01 wt% and 10 wt%, to vary casting temperature from room temperature to above polymer melting temperature, and to vary the rate of solvent evaporation. The rate of solvent evaporation was varied by either allowing a solvent to evaporate into open air, by reducing the rate of evaporation using the drop cast chamber or by casting the drop inside a 120-milliliter glass bottle and immediately capping the bottle with a cap into which a 1/16-inch diameter vent hole had been drilled. The resulting coating on a mica substrate was visually inspected after it had dried. If any portion of the coating appeared glassy, then that portion of the coating was deemed to be smooth – potentially smooth enough for an AFM roughness measurement. The percentage of the area of the coating was estimated. When a change in one of the parameters of concentration, temperature, or rate of evaporation resulted in an increase in smooth area, then the change was deemed to be a step in the right direction. The correct direction for each parameter was determined, and followed. Smooth coatings were thereby obtained.

The conditions and results of the experiments are given in Table 7. The polymers are listed in order of increasing hydrophobicity. For each polymer, the experiments are listed in the order in which they were performed. It can be seen in Table 7 that the smooth percentages of the coatings made with each polymer generally increase as one moves down the table.



Table 7. Polymer solution drop casting experiments on mica substrates, including percent area estimates of glassy surface on each coating, and roughness measurements of ten-micron scans over glassy areas by AFM.

Polymer	Concentration, wt%	Solvent (ambient temperature unless noted)	Coating Conditions	% Glassy Area; Roughness of a Smooth Area
Nylon 6	1	2,2,2-trifluoroethanol	22° C, chamber w/ 90% solvent vapor pressure	0% smooth
Nylon 6	1	2,2,2-trifluoroethanol	120° C, in air	0% smooth
Nylon 6	1	Phenol, liquefied with 9.8 % water	130° C, inside vented bottle	5% smooth
Nylon 6	10	Phenol, liquefied with 9.8 % water	245° C, in air, inside oven	0% smooth
Nylon 6	1	Phenol, liquefied with 9.8 % water	245° C, in air, inside oven	70% smooth
Nylon 6	0.1	Phenol, liquefied with 9.8 % water	245° C, in air, inside oven	80% smooth; 1.8 nm RMS
Nylon 6	0.01	Phenol, liquefied with 9.8 % water	245° C, in air, inside oven	90% smooth
PMMA	0.1	Toluene	24° C, chamber w/ 90% solvent vapor pressure	50% smooth 59 nm RMS
PMMA	10	Toluene	22° C, in air	100% smooth; 0.78 nm RMS
PE-MA	1	Toluene, 100° C	100° C, inside oven	40% smooth; 27 nm RMS
PE-MA	1	<i>O</i> -xylene, 130° C	130° C, inside vented bottle	0% smooth
PE-MA	10	<i>O</i> -xylene, 130° C	130° C, inside vented bottle	0% smooth
PE-MA	5	<i>O</i> -xylene, 130° C	180° C, inside vented bottle	5% smooth
PE-MA	5	<i>O</i> -xylene, 130° C	180° C, in air	10% smooth
PE-MA	1	<i>O</i> -xylene, 130° C	180° C, in air	40% smooth
PE-MA	0.1	<i>O</i> -xylene, 130° C	180° C, in air	90% smooth; 1.1 nm RMS
PE-MA	0.01	<i>O</i> -xylene, 130° C	180° C, in air	95% smooth

PMMA was the first polymer on which coating experiments were conducted. PMMA was easy; it only required two experiments to achieve a 100% smooth coating, with a roughness reading of 0.78 nm RMS. The low roughness value set a standard for nylon 6 and PE-MA.

Coating experiments with nylon 6 and PE-MA were performed in tandem. It was found that the combination of a low polymer concentration, a high casting temperature, and uninhibited solvent evaporation produced smooth coatings. In experimenting with casting temperature, the temperature for nylon 6 was first increased to above the glass transition temperature of 62.5° C. (The glass transition temperature was printed on the Sigma-Aldrich label of the bottle in which the nylon 6 was packaged). The temperature was increased again, to above the melting point of 210-225° C [55]. For the experiments at higher temperature, liquefied phenol was used as the solvent instead of 2,2,2-trifluoroethanol. (According to the Fisher Scientific label on the bottle in which the liquefied phenol was packaged, the liquefied phenol contained 90.6% phenol and 9.8% water). The boiling point of 2,2,2-trifluoroethanol is 78° C [51]; the boiling point of phenol is 182° C [50]. Casting at high temperature with a low-boiling-point solvent would have made it difficult to inhibit the rate of evaporation, which was one of the parameters in the experiments. In the end, the parameters for producing a smooth nylon 6 coating were chosen to be a 0.1 wt% concentration in liquefied phenol, cast onto a preheated mica substrate in the open air inside an oven set at 245° C. A concentration of 0.01 wt% was an option, but it produced a coating that was difficult to see.

The casting temperature for PE-MA was also increased – first above the melting point temperature of 120° C and then to near a melt-index temperature of 190° C. (Both temperatures were obtained from the Sigma Aldrich label on the bottle in which the PE-MA was packaged.) For the higher temperatures, the solvent *o*-xylene, which has a boiling point of 144° C [53], was used instead of toluene, which has a boiling point of 111° C [52]. The parameters for producing a smooth PE-MA coating were chosen to be a 0.1 wt% concentration in *o*-xylene, cast onto a preheated mica substrate in the open air inside an oven set at 180° C. A concentration of 0.01 wt% might have been chosen if the coating it produced had not been difficult to see.

Roughness values of the nylon 6 and PE-MA coatings made at the selected conditions were measured. They were 1.8 nm RMS and 1.1 nm RMS, respectively. The values compare favorably with the value of 0.78 nm RMS obtained with PDMS. Three-dimensional images of the 10.2 μm scans used to calculate the roughness values are shown in Figure 29. The aspect ratio of the images is 500, which is 50 times greater than the aspect ratio of the three-dimensional image of the Cloisite® 20A coating in Figure 28. The polymer coatings were significantly smoother.

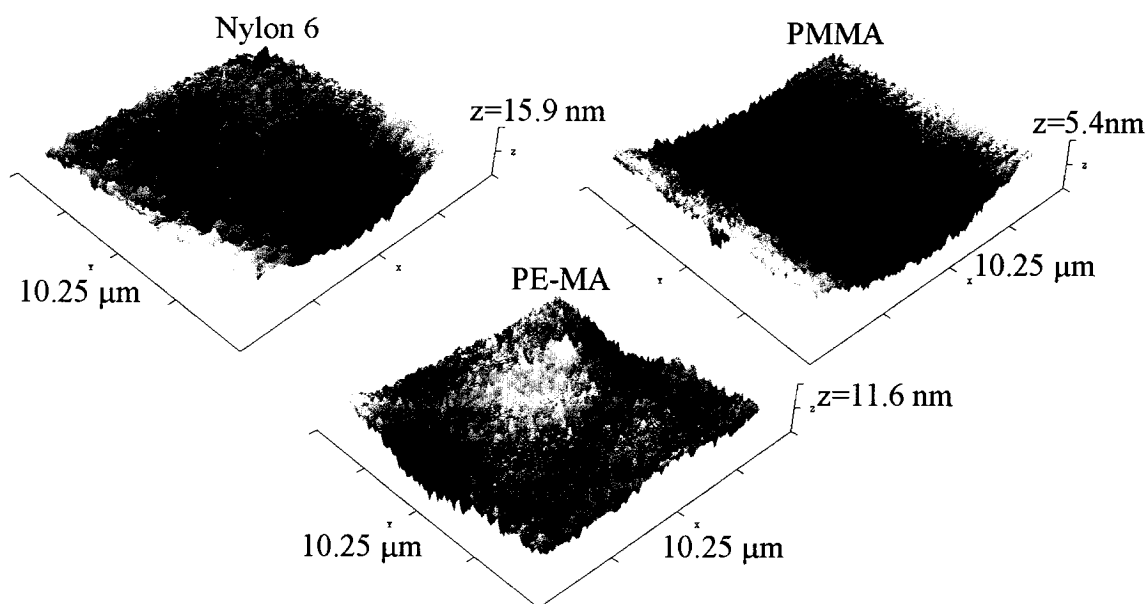


Figure 29. Three-dimensional images of 10.2  $\mu\text{m}$  AFM scans of smooth polymer coatings on mica substrates. The aspect ratio is 500.

Szücs *et al.* reported a roughness value of 0.57 nm RMS for a two micron scan of a coating of polydiallyldimethylammonium chloride (PDDACl) [27]. The roughest of the three scans shown in Figure 29, of nylon 6, compares favorably. According to NanoRule+, two-micron-by-two-micron subsections of the scan have a roughness of about 0.8 nm RMS.

The nylon 6 coating most likely underwent oxidative degradation when it was cast. Nylon 6 is known to rapidly oxidize when it is heated above 200° C in air [55]; the coating was cast at 245° C. The thicker coatings, cast with one percent and ten percent solutions, were visibly discolored; they were amber. The use of liquefied phenol as the solvent contributed a significant amount of water, which contributes to the degradation of nylon 6 through nucleophilic attack [25]. The degree to which the nylon 6 in the coating

was degraded is unknown. The effect of the nylon 6 degradation on adhesive force measurements is also unknown.

## 5.5 OMMT Coating Experiments on Colloidal Probes

Experiments were performed on coating colloidal probes with Cloisite® 25A. Cloisite® 25A was chosen because it was the middle of the three OMMTs studied in terms of hydrophobicity. It was thought that if a technique was developed to coat Cloisite® 25A onto colloidal probes, then the technique would be transferable to coating Cloisite® 30B and Cloisite® 20A.

Three parameters were varied. They were the solvent in which the OMMT was dissolved, the concentration of the OMMT in the coating solution, and the types of pretreatment performed before dip-coating a colloidal probe. In every experiment, the colloidal probe was coated by dipping it in a Cloisite® 25A solution for twenty to thirty seconds. Prior to coating, the solution was sonicated at 50° C for one hour.

Three microscopy techniques were used to verify the presence of Cloisite® 25A coatings on the borosilicate particles of the probes: scanning electron microscopy (SEM), energy dispersive x-ray analysis (EDX analysis), and atomic force microscopy (AFM). Probes were sputter coated with gold before being placed in an SEM, unless otherwise noted. AFM was performed using the MikroMasch TGT1 tip characterization grating, to obtain reverse images of a borosilicate particle.

The experiments are presented in the order in which they were performed. In the first experiment, a new colloidal probe was dip-coated without any pretreatment. It was dipped in a 320 ppm Cloisite® 25A – chloroform solution, and then held in the air until

drops visible on the probe chip and substrate had dried. Six days later it was sputter coated with gold and viewed using a Hitach S-2300 scanning electron microscope (see Figure 30). A coating is clearly evident on the borosilicate particle, but it is very rough. It was thought that the roughness was related to the low clarity of the chloroform solution, and that non-exfoliated OMMT particles had settled onto the borosilicate particle. See Figure 25, which shows that the solution was cloudy.

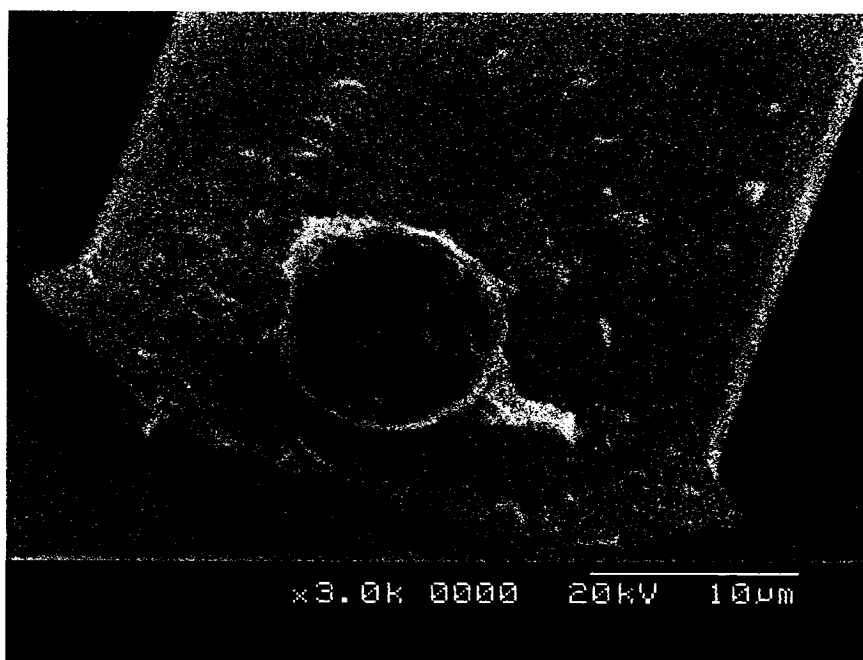


Figure 30. SEM image showing an uneven coating of Cloisite® 25A on the borosilicate particle of a new probe dip-coated in a 320 ppm Cloisite® 25A – chloroform solution.

In the next experiment, a probe was dip-coated and imaged three times. It was pretreated by sputtering it with gold, imaged via SEM, and then dip-coated in a 320 ppm Cloisite® 25A – NMP solution. The probe was sputtered, imaged, and then dipped in a 3,200 ppm solution. It was sputtered, imaged, and then dipped in a 32,000 ppm (3.2%) solution. It was sputtered and imaged.

The probe was first sputtered with gold for two reasons. The first reason was to image it before coating it, for comparison after it was coated. The second reason was to improve the wetting of the coating solution on the borosilicate particle. It was thought that better wetting would translate to a smoother coating. In a side experiment, the degree that drops of NMP spread on a gold-sputtered glass microscope slide (VWR International, catalog item 48312-002) was compared to NMP spread on a cleaned but otherwise untreated slide. The NMP spread better on the gold-sputtered slide. SEM images showing the gold-sputtered probe before dip-coating is shown in Figure 31.

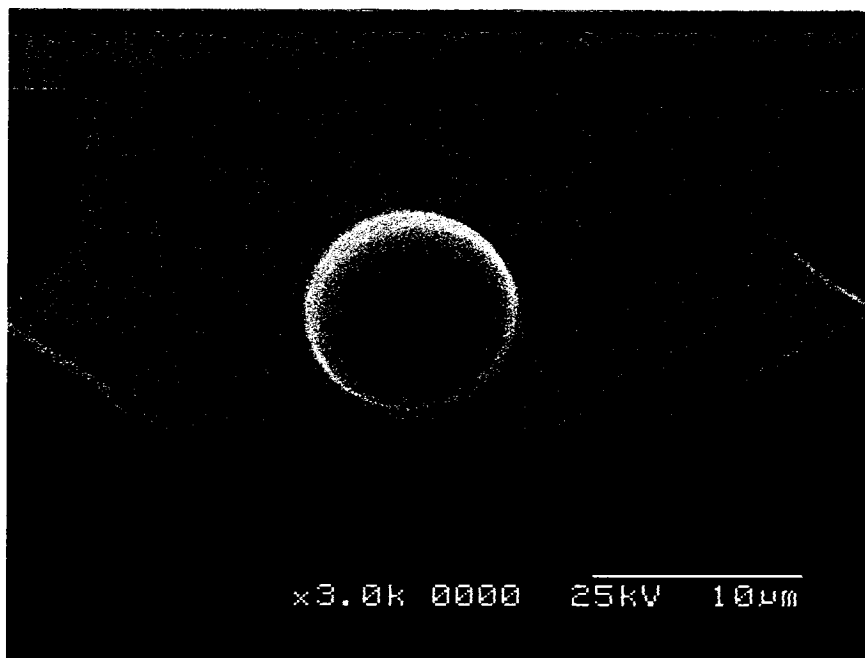


Figure 31. SEM image of gold-sputtered colloidal probe before it was dip-coated.

The probe was dip-coated in 320 ppm Cloisite® 25A solution. The probe was dried by placing it in an oven at 95° C for 30 minutes. While the probe was drying, it was oriented such that the borosilicate sphere was facing down – to have gravity assist in keeping coating solution on the borosilicate particle. After the probe was dry, it was

sputtered with gold and imaged; see Figure 32. In comparing Figure 31 and Figure 32, it appears that the probe gained a partial collar around the borosilicate particle. Perhaps the collar was an artifact of the adhesive that Novascan Technologies used to attach the borosilicate particle.

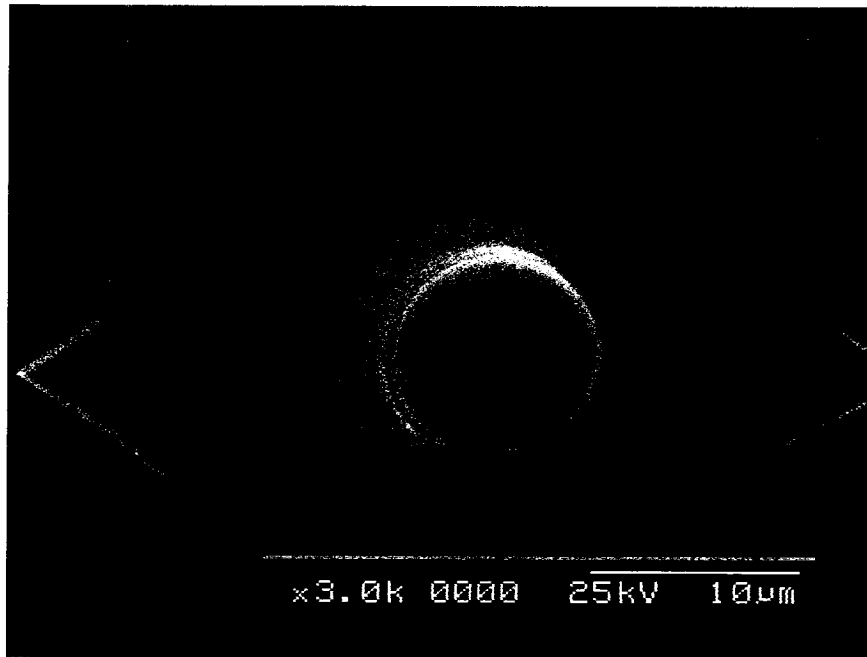


Figure 32. SEM image of probe after dip-coating in 320 ppm Cloisite® 25A – NMP.

The concentration was increased; the probe was dip-coated in 3,200 ppm Cloisite® 25A – NMP solution. It was dried, sputtered with gold, and imaged. See Figure 33.





Figure 33. SEM image of probe after dip-coating in 3,200 ppm Cloisite® 25A – NMP. The borosilicate particle appears fuzzier after dip-coating in the 3,200 ppm solution. The fuzziness may be an indication of a coating of Cloisite® 25A.

The probe was dip-coated one more time, in 32,000 ppm (3.2%) Cloisite® 25A – NMP solution. The solution was viscous, like syrup. The probe was dried; it was sputtered with gold, and imaged. See Figure 34.



Figure 34. SEM image of probe after dip-coating in 32,000 ppm Cloisite® 25A – NMP. The borosilicate particle appears fuzzy, perhaps fuzzier, after dip-coating in the 32,000 ppm solution. A conclusion was made that a coating of Cloisite® 25A was present on the borosilicate particle.

In the next experiment, a new probe was sputtered with gold and dip-coated in 32,000 ppm Cloisite® 25A – NMP solution. After the probe was dried, it was sputtered with gold for imaging and EDX analysis with a LEO 435. It was compared with a new probe – a blank. See Figure 35 and Figure 36 for SEM images of both probes.

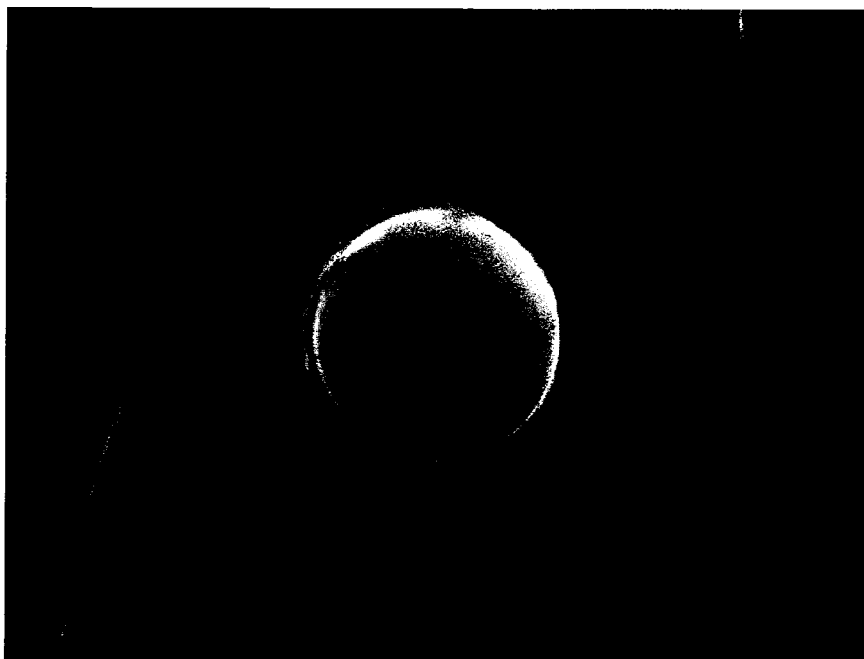


Figure 35. SEM image of a probe after sputtering it with gold, dip-coating it in 3,200 ppm Cloisite® 25A – NMP solution, drying it, and sputtering it with gold again.

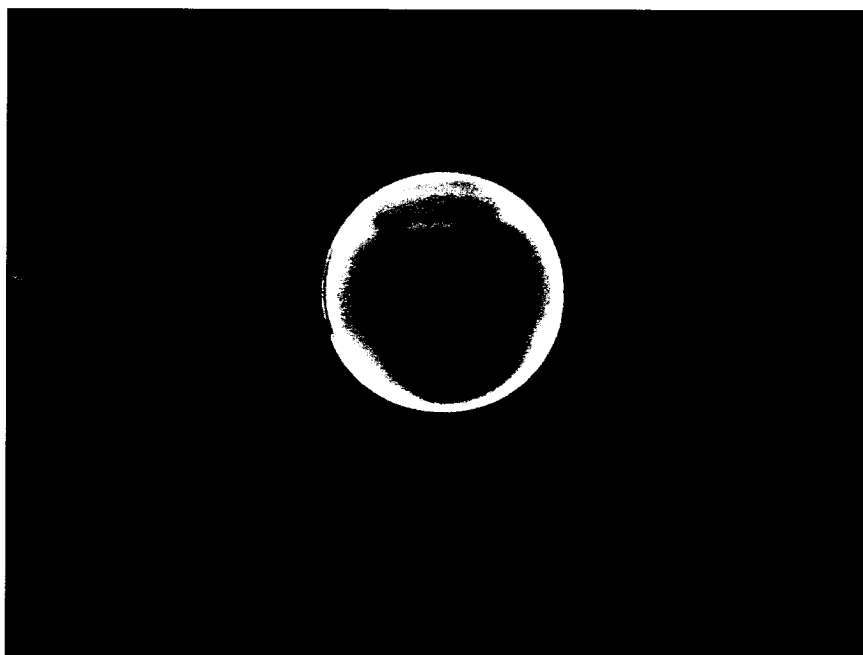


Figure 36. SEM image of a new probe – a blank.

It appears in Figure 35 that a coating is present on the upper right part of the top of the borosilicate sphere (as viewed); it is not as clear that there is a coating in the shadow, down and to the right. There appears to be a coating on the probe cantilever around the borosilicate particle, in the form of a collar. A collar-like artifact was also observed in the previous experiment. On the blank shown in Figure 36, no coating is apparent.

EDX analysis was performed both on the coated probe and the blank. A spectrum of each is shown in Figure 37 and Figure 38. The spectra differ in that the dip-coated probe has small peaks for gold (labeled “Au”) and magnesium (hand labeled “Mg”).

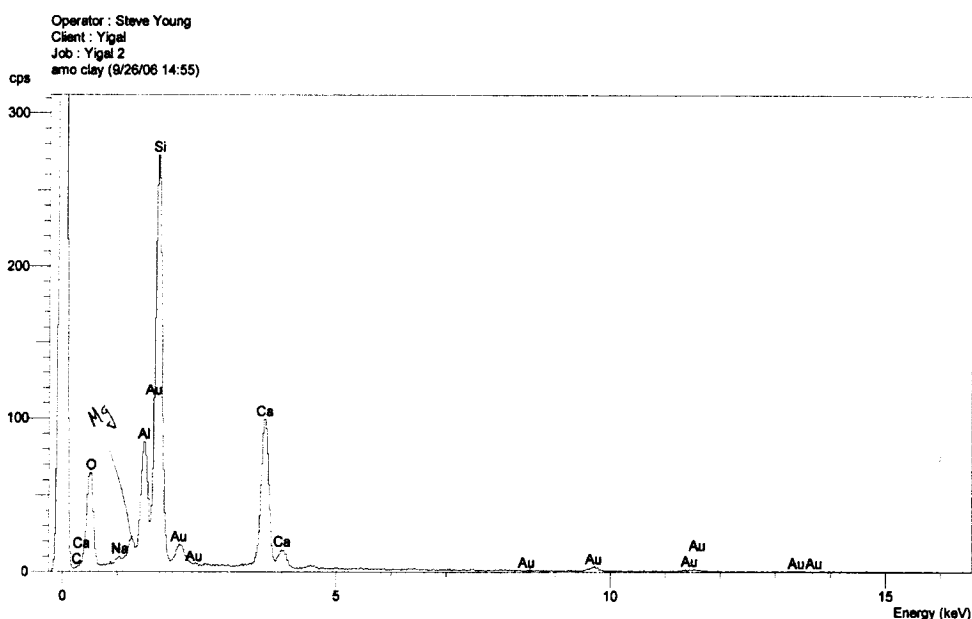


Figure 37. EDX spectrum of a colloidal probe sputtered with gold, dip-coated in 32,000 ppm Cloisite® 25A – NMP solution, and sputtered again with gold. A small peak on the left is hand labeled “Mg.”

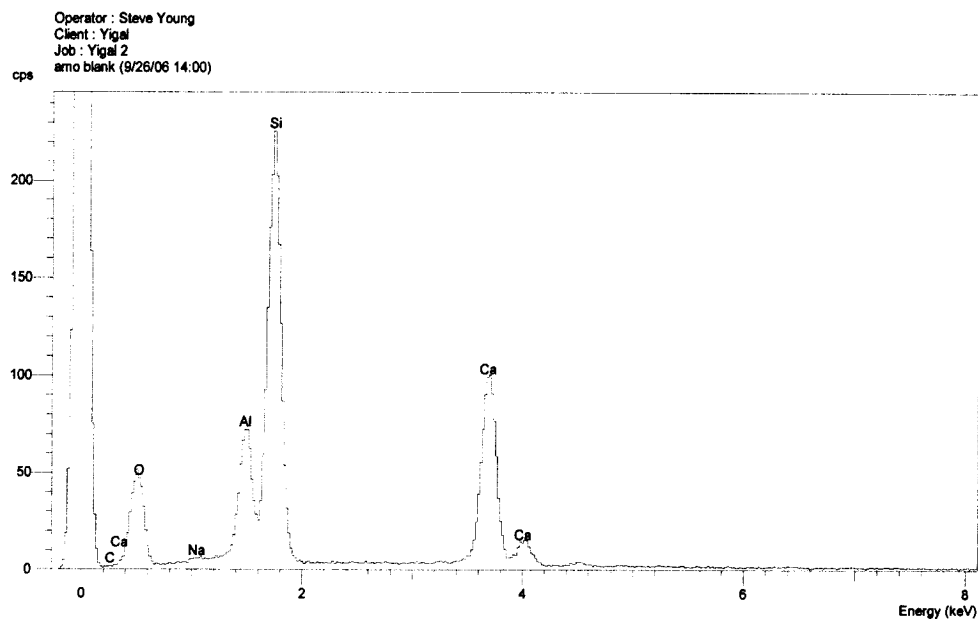


Figure 38. EDX spectrum of a blank – a new colloidal probe.

The presence of a peak for magnesium confirms the presence of Cloisite® 25A, which is composed of montmorillonite and an organic cation. Montmorillonite contains magnesium atoms; they substitute for aluminum atoms and give montmorillonite an ion exchange capacity.

EDX images corresponding to the spectrum obtained with the gold-sputtered and dip-coated probe are shown in Figure 39. The images show the relative strength of different peaks over the area of the probe that was scanned. The image labeled “MgKa1,, 9” corresponds to the magnesium peak. The image is quite noisy, but it shows a brighter area where the borosilicate particle is located. The brighter area suggests the presence of Cloisite® 25A on the borosilicate particle. Curiously, there is no bright area around the borosilicate particle that would correspond to the collar visible in the SEM image in

Figure 35. Perhaps the collar consists of the adhesive used to attach the borosilicate particle to the cantilever. Perhaps exposure to NMP during dip-coating changed the surface roughness of the adhesive, rendering it visible in SEM images.

Operator: Steve Young  
Client: Yigal  
Job: Yigal 2  
Label: (untitled) (26 Sep 06 15:16:56)

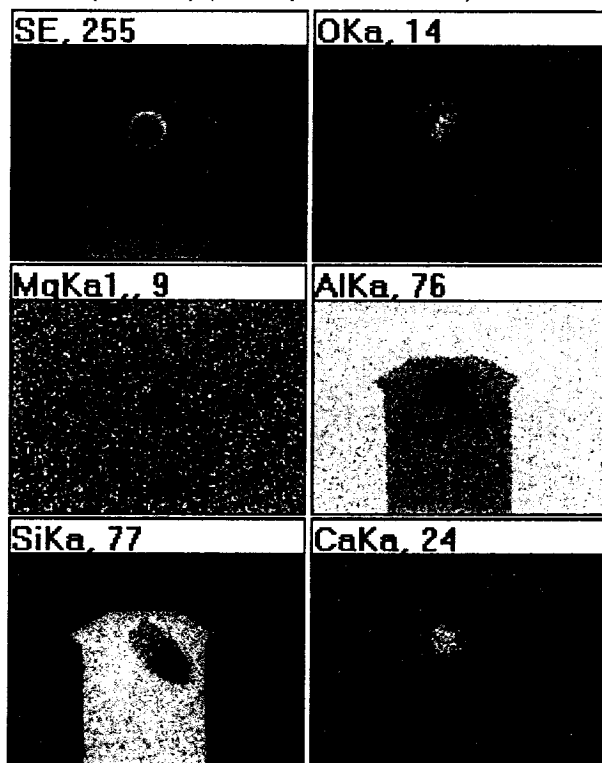


Figure 39. EDX images of a colloidal probe sputtered with gold, dip-coated in 32,000 ppm Cloisite® 25A – NMP solution, and sputtered again with gold.

EDX analysis showed promise for confirming the presence of OMMT coatings on colloidal probes. The technique was not developed further in this study.

The probes that underwent EDX analysis were scanned on the Nano-R™ AFM afterwards. The probes were scanned over the TGT1 tip characterization grating. The

scans were five microns in size. Images from the scans are shown in Figure 40 and Figure 41.

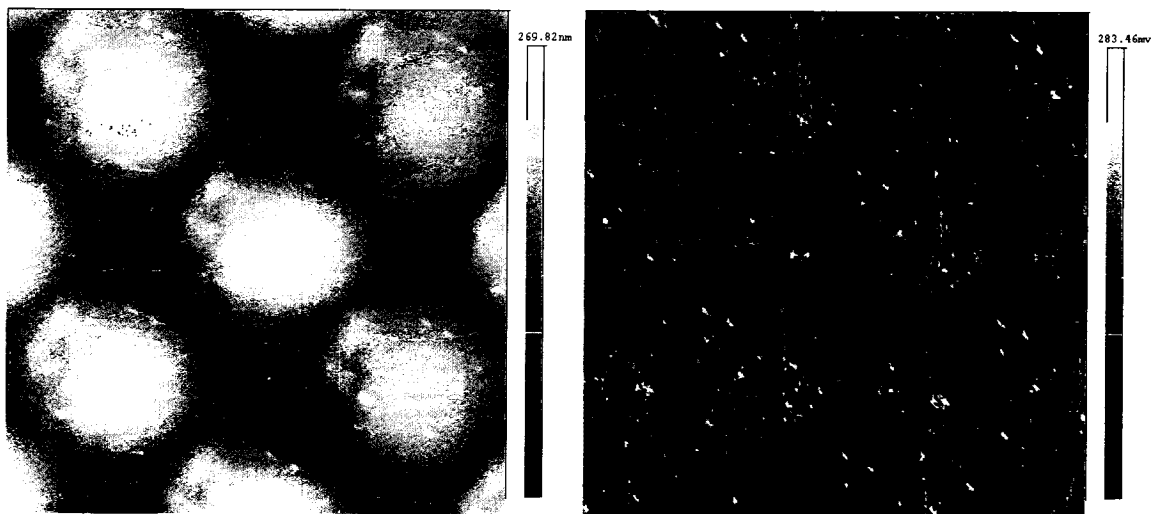


Figure 40. AFM contrast-brightness displays of Z(SEN) on the left and Z(ERR) on the right, obtained by reverse imaging the colloidal probe shown in Figure 35 (first sputtered with gold and then dip-coated in 32,000 ppm Cloisite® 25A – NMP solution).

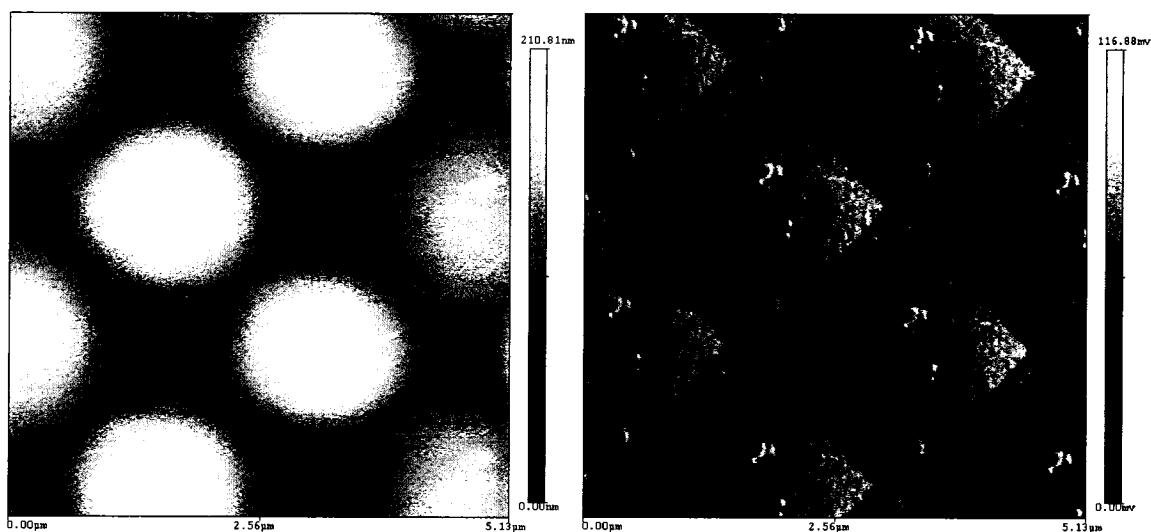


Figure 41. Contrast-brightness displays of Z(SEN) on the left and Z(ERR) on the right obtained by reverse imaging the blank colloidal probe shown in Figure 36 via AFM.

The left and right images in Figure 40 and Figure 41 each contain multiple scans of the top of the borosilicate particle on the respective probes. The scans are about 2.2 microns

in size, corresponding to the spacing between tips on the TGT1 grating. The displays of Z(SEN) indicate surface elevation; the displays of Z(ERR) indicate surface texture.

The top of each scan in the images shown in Figure 40 corresponds to the part of the borosilicate particle that is closest to the end of the cantilever. The rougher area on the left side seems to correspond to the apparent coating visible on the upper-right area of the top of the borosilicate particle in the SEM image of Figure 35. Like the SEM image, the AFM images do not appear to confirm that a coating of Cloisite® is present on the smoother area to the right.

The AFM images shown in Figure 41 appear to indicate that the blank probe picked up some dust particles after the EDX analysis. The most useful role of AFM in imaging the spherical particles on colloidal probes seems to be checking the roughness of the coatings and detecting the presence of dust particles. Excessive roughness and dust particles may compromise adhesive force measurements obtained through force/distance curves. The effectiveness of using a TGT1 grating to confirm the presence of a coating is compromised by organoclay particles that deposit on the probe cantilever; the particles negatively affect the light-lever system by causing specular reflections.

In the last OMMT coating experiment on colloidal probes, two probes were dip-coated in a 10% Cloisite® 25A – NMP solution. Both probes were new. The first probe was dip-coated without any pretreatment. The second probe was dip-coated after it was sputtered with gold. The probes were dried, sputtered with gold, and imaged on a Hitachi S-2300. SEM images are shown in Figure 42 and Figure 43.



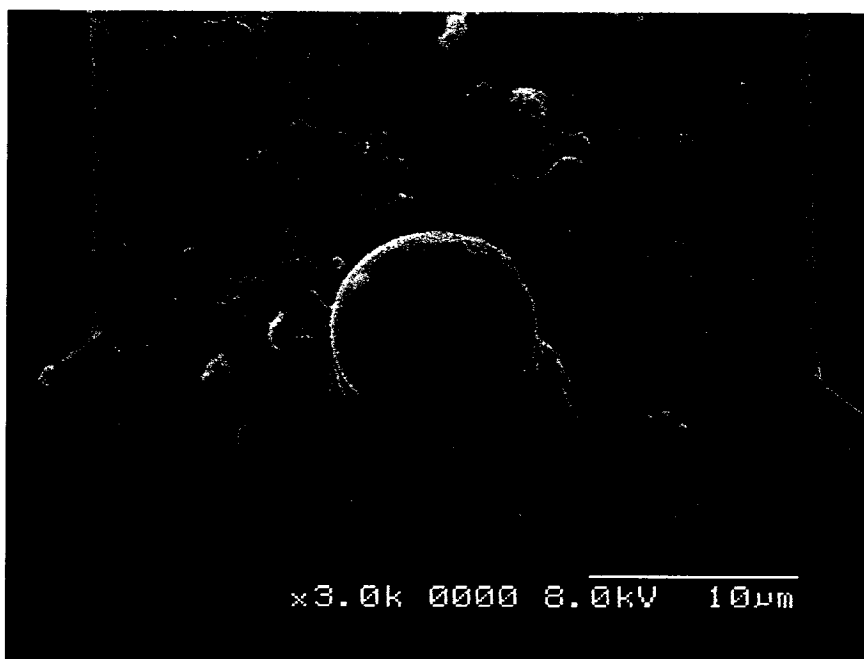


Figure 42. SEM image showing a rough coating of Cloisite® 25A on the borosilicate particle of a new probe dip-coated in a 10% Cloisite® 25A – NMP solution.

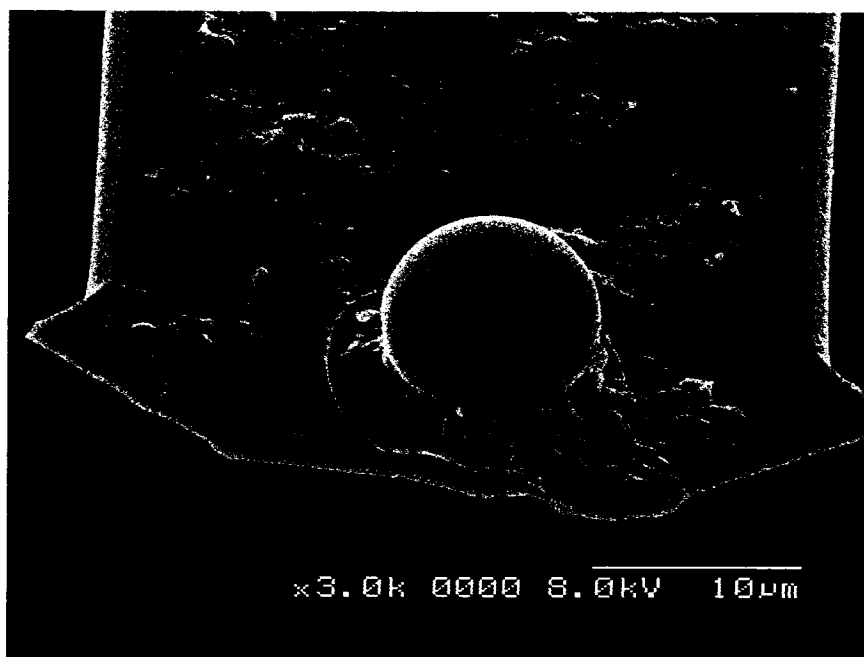


Figure 43. SEM image showing a lack of a visible coating of Cloisite® 25A on most of the borosilicate particle of a new probe first sputtered with gold and then dip-coated in a 10% Cloisite® 25A – NMP solution.

A rough coating is evident on the top the borosilicate particle in Figure 42. A coating is not evident in Figure 43; there appear to be only spots of Cloisite® 25A on the borosilicate particle. From these images, it appears that pretreating a colloidal probe with gold is detrimental to coating a borosilicate particle on the probe. Note also that there are fewer clusters of Cloisite® 25A on the cantilever of the probe that was pretreated with gold.

The poor result with gold might be related to an inherent quality of gold or it might be attributable to environmental effects. According to Kapple and Butt, gold surfaces under ambient conditions are usually coated with organic contaminants that greatly reduce the surface energy [34]. A reduced surface energy can inhibit wetting, and therefore inhibit coating.

Environmental effects may also inhibit coating of new probes. Sirghi *et al.* reported in 2006 that silicon AFM probes lost hydrophilicity due to contaminants present in the air and due to contaminants present in packaging [56]. They found that they were able to remove contaminants by placing the probes in a plasma cleaning system, but that the hydrophilicity of the cleaned probes declined in a few days. They attributed the decline in hydrophilicity to the adsorption of airborne contaminants.

In this study, the contamination of new colloidal probes seemed to be a problem only if the contamination inhibited the wetting and possible contamination of the borosilicate particles on the probes. The lack of access to a plasma cleaning system led to the consideration of an alternative – treatment with silane coupling agents. It was thought that silane coupling agents would both displace organic contaminants from the

borosilicate particles and render the surfaces of the borosilicate particles amenable to coating for a time. The idea was tested on borosilicate pipettes, by treating pipettes with the silane coupling agents APTES and EPPMS and then immediately dip-coating them in solutions of Cloisite® 30B, 25A, and 20A over a range of concentrations. The resulting coatings on the pipettes were compared with the coatings on pipettes that had been dip-coated in the same solutions but that had not been pretreated. Three sets of experiments were conducted. The experiments are summarized in Table 8 through Table 10.

Table 8. Effect of Cloisite® 20A concentration and APTES treatment on coating quality of dipped lengths of borosilicate pipettes, from the first experiment.

Weight Concentration of Cloisite® 20A in Chloroform	Untreated Pipette, Description of Coating	APTES-Treated Pipette, Description of Coating
320 ppm	Small islands of clay	Hazy coating
3,200 ppm	White haze	Slightly hazy coating
32,000 ppm (3.2%)	Hazy coating	Translucent coating

Table 9. Effect of Cloisite® 25A and 30B concentration and EPPMS treatment on amount coated on dipped-lengths of borosilicate pipettes, from the second experiment.

Weight Concentration of Cloisite® 25A or 30B in NMP	Untreated Pipette, Amount Coated	EPPMS-Treated Pipette, Amount Coated
320 ppm 25A	One small spot only	Four small spots only
3,200 ppm 25A	70% of dipped length	100% of dipped length
320 ppm 30B	Two small spots only	One small spot only
3,200 ppm 30B	30% of dipped length	40% of dipped length

Table 10. Effect of Cloisite® 25A and 30B concentration and EPPMS treatment on amount coated on dipped-lengths of borosilicate pipettes, from the third experiment.

Weight Concentration of Cloisite® 25A or 30B in NMP	Untreated Pipette, Amount Coated	EPPMS-Treated Pipette, Amount Coated
3,200 ppm 25A	60% of dipped length; Haze possibly on the rest	75% of dipped length; haze definitely on the rest
3,200 ppm 30B	40% of dipped length; haze possibly on the rest	60% of dipped length; haze possibly on the rest
10,000 ppm 30B	70% of dipped length; haze possibly on the rest	100% of dipped length

The conclusion was drawn that silane treatment improved the coating of borosilicate pipettes with Cloisite® solutions. Silane treatment was used as a pretreatment in subsequent coating of colloidal probes with OMMT.

## 5.6 Polymer Coating Experiments on Colloidal Probes

Three experiments were performed on coating colloidal probes with PMMA. In the first experiment, borosilicate pipettes were substituted for colloidal probes. The effect of silane treatment was investigated. The experiment is summarized in Table 11.

Table 11. Effect of PMMA concentration and APTES treatment on coating coverage of dipped lengths of borosilicate pipettes.

Weight Percent of PMMA in Chloroform	Untreated Pipette, Amount of Dipped Length Coated	APTES-Treated Pipette, Amount of Dipped Length Coated
0.1	Mostly uncoated – spots only	Mostly uncoated – spots only
1	Entire dipped-length coated	Entire dipped-length coated
10	Entire dipped-length coated	Entire dipped-length coated

Silane treatment had no discernable effect. Nevertheless, it was concluded that there was an advantage to silane treating colloidal probes before coating them with PMMA solution. The advantage was that silane treatment probably replaced, on the borosilicate particles, a surface with unknown hydrophobicity (due to airborne contaminants) with a surface of known hydrophilicity.

In the second experiment, a new colloidal probe was silane treated with APTES and then dip-coated in a 10% PMMA – toluene solution. The probe was sputtered with gold after it dried. It was imaged on a Hitachi S-2300, and then on a LEO 435. See Figure 42 and Figure 43 for the respective SEM images. The probe appears to be coated

quite thickly. The coating appears to cover the top of the borosilicate particle, too, where some of the PMMA appears to have formed a protuberance.

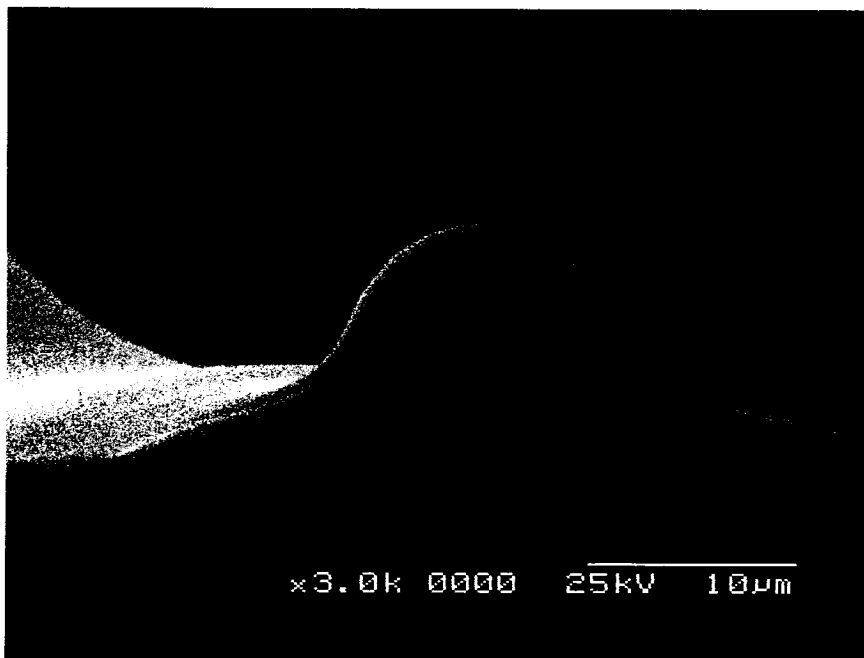


Figure 44. SEM image obtained on a Hitachi S-2300 showing a thick coating of PMMA on a colloidal probe that was first silane-treated with APTES and then dip-coated in a 10% PMMA – toluene solution.



Figure 45. SEM image obtained on a LEO 435 showing a coating of PMMA on the borosilicate particle of the same colloidal probe shown in Figure 44.

The LEO 435 was then used to perform EDX analysis on the coated probe. The EDX spectrum is shown in Figure 46.

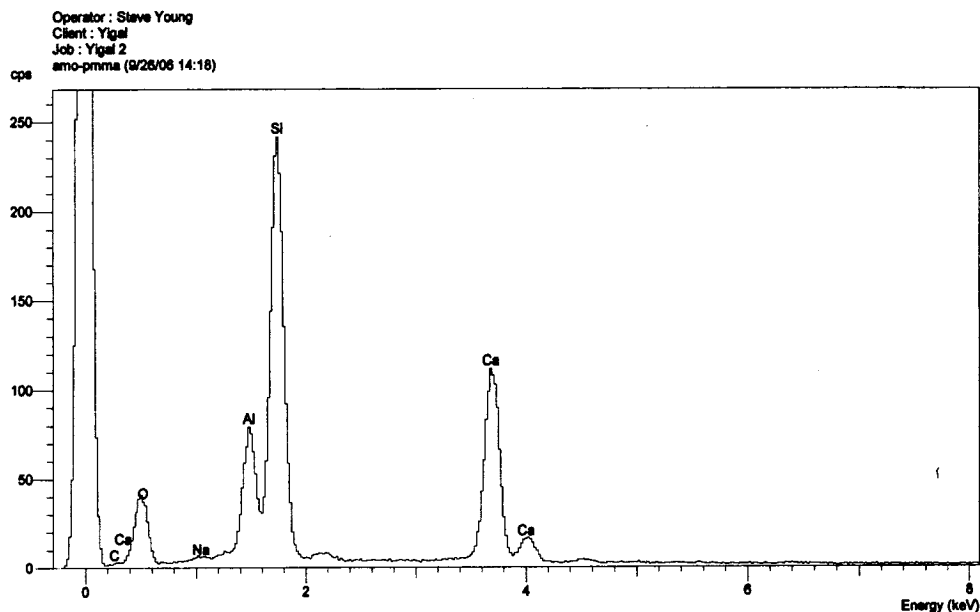


Figure 46. EDX spectrum of the colloidal probe silane-treated with ATPES and dip-coated in 10% PMMA – toluene solution. C peak is larger compared to C peak in the EDX spectrum of the blank colloidal probe shown in Figure 38. The larger C peak confirms the presence of a PMMA coating.

The EDX spectrum obtained from the PMMA-coated colloidal probe can be compared to the EDX spectrum of the blank probe, shown in Figure 38. The EDX spectrum of the PMMA-coated probe has a very small carbon peak, labeled “C.” Although it is very small, it is larger than the carbon peak on the EDX spectrum of the blank probe. The larger carbon peak is consistent with the presence of PMMA on the probe

In the third experiment, the apparently detrimental effect of gold on effective coating was confirmed. A new colloidal probe was sputtered with gold, and then dip-coated in a 10% PMMA – toluene solution. It was sputtered with gold again, and imaged on a Hitachi S-2300. An SEM image is shown in Figure 47.

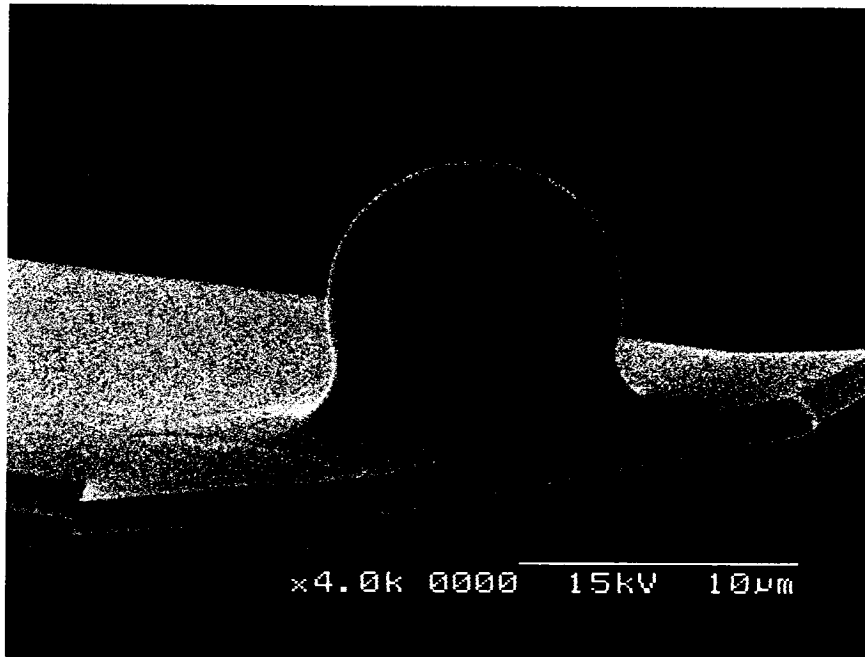


Figure 47. SEM image showing a colloidal probe that was sputter-coated with gold and then dip-coated in a 10% PMMA – toluene solution.

A coating of PMMA on the probe is not apparent. The difference between the probes shown in Figure 47 and Figure 44 is striking. Both probes were dip-coated in 10 wt% PMMA – toluene solution, but the probe that was pretreated with APTES had a thick coating of PMMA while the probe that was pretreated with gold appears to have had none.

### 5.7 OMMT Placement Option Experiments

Experiments were performed to study the option of OMMT placement in force/distance curve studies of the adhesive forces between OMMTs and polymers. The OMMTs can be located on probes and the polymers can be located on substrates, or OMMTs can be located on substrates and the polymers can be located on probes. The



objective of the experiments was to determine which option is better. Cloisite® 20A and PMMA were the OMMT and polymer used in the experiment.

The experiments consisted of recording force/distance curves – first between a colloidal probe coated with Cloisite® 20A and a mica substrate coated with PMMA, and second between a colloidal probe coated with PMMA and a mica substrate coated with Cloisite® 20A. For each experiment, the preparation of colloidal probes and substrates is described. Force/distance retraction-curve data are presented in Section 5.7.1 and Section 5.7.2. A conclusion is made as to which option is better, and at the end, the results are interpreted.

#### 5.7.1 Force/Distance-Curves Experiment with OMMT on the Probe

A colloidal probe with 0.08 N/m force constant and a ten-micron diameter borosilicate particle was coated with Cloisite® 20A by first silane-treating it with APTES and then dip-coating it in a 3,200 ppm Cloisite® 20A – chloroform solution. To confirm that the borosilicate particle was coated, the top of the borosilicate particle was scanned using the Nano-R™ atomic force microscope when the probe was new and after the probe was coated. The borosilicate particle was scanned by placing the colloidal probe on the sample puck, and scanning the borosilicate particle with a contact probe. Scans were 2.2 μm in size – approximately the same size that are obtained using the TGT1 tip characterization grating. Each 2.2 μm scan was followed by a 0.7 μm scan in a relatively flat area within the 2.2 μm scan. The 0.7 μm scans were leveled. Three-dimensional representations of the Z(SEN) data are shown in Figure 48 and Figure 49.

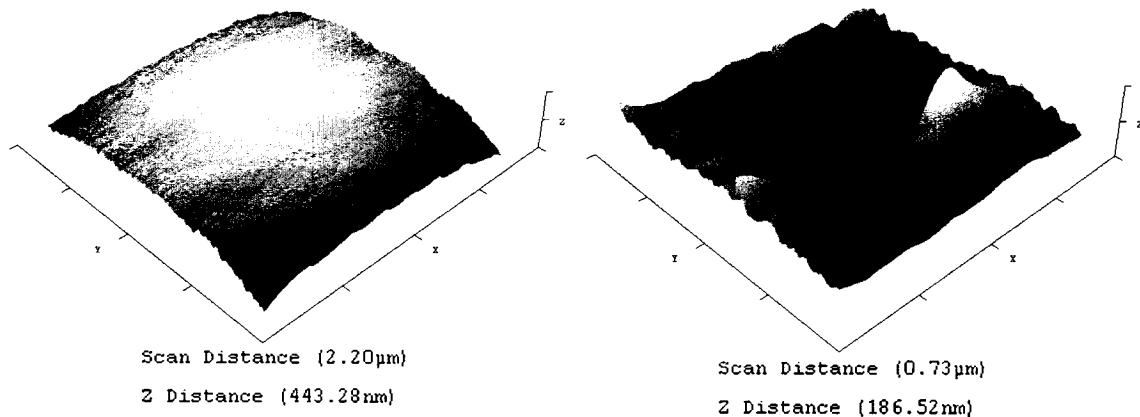


Figure 48. Three-dimensional images of 2.2 μm and 0.7 μm AFM scans of a borosilicate particle on a colloidal probe when it was new, before it was coated with Cloisite® 20A. The aspect ratio is three.

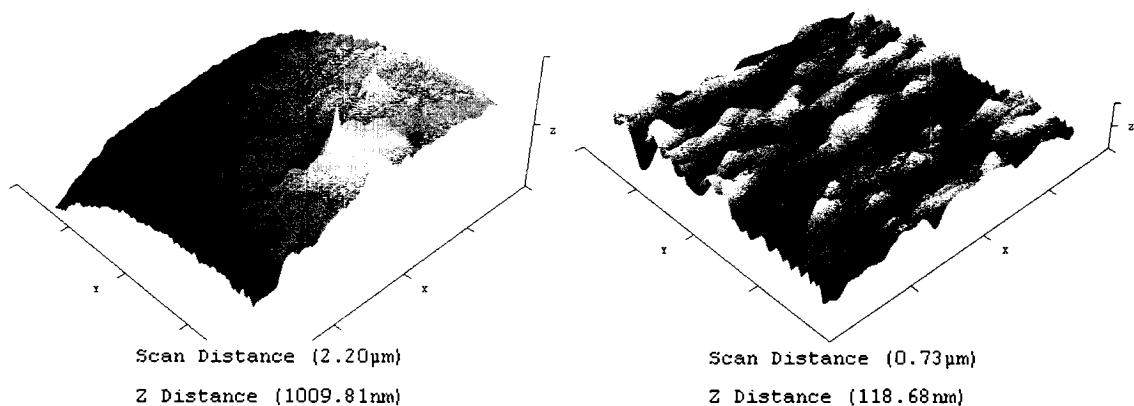


Figure 49. Three-dimensional images of 2.2 μm and 0.7 μm AFM scans of a borosilicate particle on a colloidal probe after silane-treating it with APTES and dip-coating it in a 3,200 Cloisite® 20A – chloroform solution. The aspect ratio is three.

The 2.2 μm scans were not performed over the same area of the borosilicate particle. It was difficult to position the tip of the contact probe on the apex of the particle. The 0.7 μm scans appear quite different, which suggests that a coating of Cloisite® 20A formed on the surface. The roughness value obtained from the 0.7 μm scan before coating was 5.8 nm RMS; the roughness value obtained after coating was 14.1 nm RMS.

The colloidal probe was considered to be coated with Cloisite® 20A. The probe was ready for force/distance curve measurements with a PMMA coating on a mica substrate. The PMMA coating was made by drop casting a 10% PMMA – toluene solution onto a mica substrate, at 22° C in air. This particular coating is described above, in Table 7 and Figure 29. The force/distance curves were obtained over the center of the PMMA coating, where it appeared smoothest.

The force/distance-curve experiment was performed with the Cloisite®-20A-coated colloidal probe and the PMMA-coated mica substrate located inside the environmental cell. Thirty force/distance curves were obtained. The first five curves were obtained with the environmental cell open to ambient air. The last twenty-five curves were obtained with high-purity nitrogen gas flowing through the cell. The purpose of the nitrogen gas was to purge the surfaces of the probe and PMMA of water vapor and any adsorbed hydrocarbon vapors. The last seventeen curves were obtained after nitrogen had purged the cell for at least thirty minutes. In another experiment, thirty minutes was found to be a sufficient amount of time to purge water vapor from the cell.

Of thirty force/distance curves that were obtained, eleven were recorded in ASCII files. Of the eleven curves, only two were obtained at the same location on the PMMA coating. Two Z(ERR) voltage values were recorded for all thirty curves. The first value was obtained at the lowest point of the retraction curve – the point of maximum downward deflection of the probe where the adhesive force was balanced by the upward force being exerted on the probe. The second value was obtained at a point on the retraction curve base line, shortly after the probe had released and rebounded off

the surface. The second voltage was subtracted from the first voltage, to calculate the pullback voltage. The recorded Z(ERR) values of all thirty force/distance curves are listed in Table 12. The data separated by thin row-borders were obtained at the same location on the PMMA-coated substrate. The force/distance curves which were recorded in an ASCII file are indicated with “yes.”

Table 12. Z(ERR) values recorded from force/distance retraction curves, obtained between a colloidal probe coated with Cloisite® 20A and a mica substrate coated with PMMA.

F/D curve #	Recorded in ASCII file?	Z(ERR) minimum, milliVolts	Z(ERR) baseline, milliVolts	Pullback Voltage, milliVolts
1	yes	-5852	-2234	-3609
2		-5884	-2257	-3627
3		-5868	-2303	-3565
4		-5855	-2289	-3566
5		-5869	-2292	-3577
6		-5749	-2163	-3586
7		-5787	-2135	-3652
8		-5804	-2130	-3674
9		-5735	-2180	-3555
10		-5728	-2180	-3548
11		-5787	-2166	-3621
12		-5742	-2167	-3575
13	yes	-5717	-2221	-3496
14		-5756	-1859	-3897
15		-5760	-1833	-3927
16		-5725	-1856	-3869
17	yes	-5655	-1869	-3786
18		-5713	-1774	-3939
19		-5697	-1775	-3922
20	yes	-5697	-1779	-3893
21		-4329	-412	-3917
22		-4306	-423	-3883
23	yes	-4315	-449	-3866
24		-5623	-2063	-3560
25	yes	-5672	-1854	-3818
26	yes	-5726	-2012	-3714
27	yes	-5566	-1993	-3573
28	yes	-5695	-1920	-3775
29	yes	-5661	-2162	-3499
30	yes	-5726	-2056	-3670

The pullback voltages do not vary significantly among the curves obtained in the same location. If the pullback voltages had changed significantly, then the analysis of the data would have been more difficult.

The ASCII files of the eleven saved force/distance curves were processed to obtain Z(HGT) peak-width distances. The retract curves and peak-width values are shown in Figure 50.

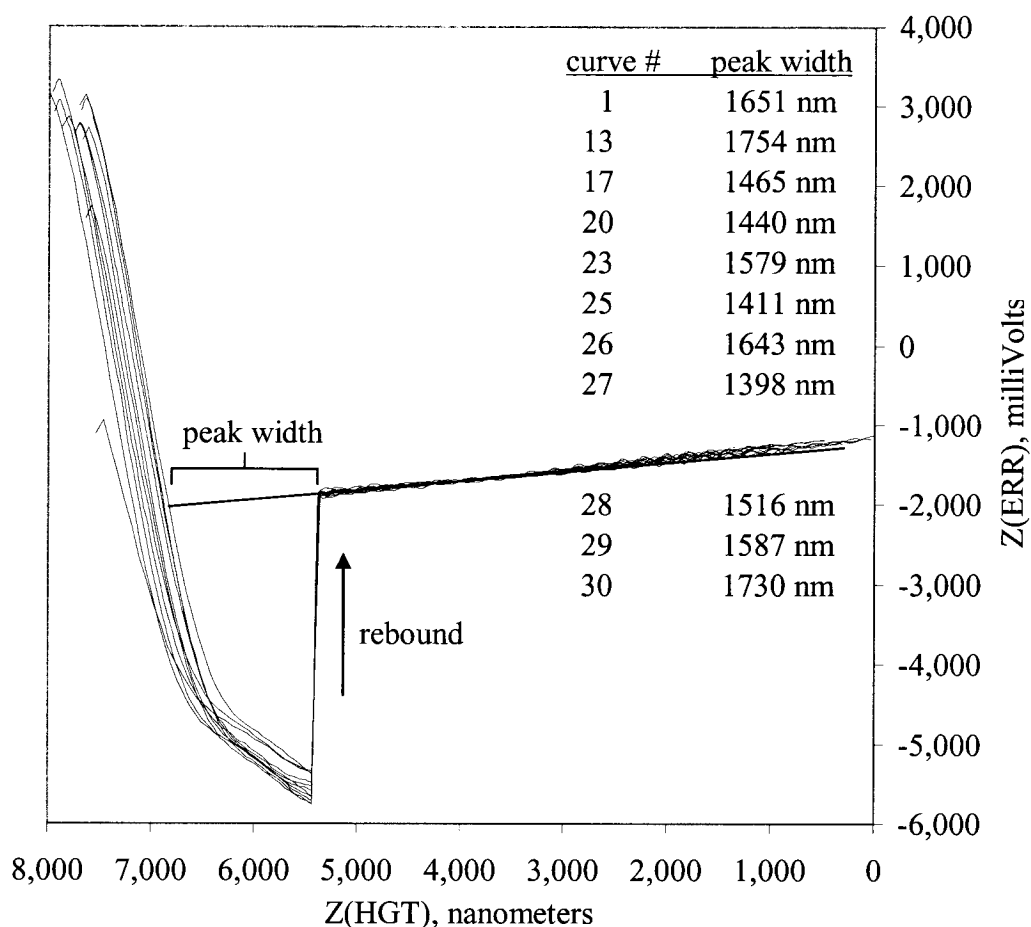


Figure 50. Force/distance retraction curves and corresponding peak-width values obtained between a colloidal probe coated with Cloisite® 20A and a mica substrate coated with PMMA. The curves are aligned for easier viewing.

The peak-width values are listed in the order in which the force/distance curves were obtained. The peak-width value of the first curve was obtained in ambient air; the value is similar to the other values, which were obtained in nitrogen. Flowing nitrogen through the environmental cell does not appear to have had much of an effect. The thirteenth curve was obtained in the same location as the first curve after nitrogen had been flowing for fourteen minutes; the peak-width value of the thirteenth curve is greater, but it is not significantly greater.

The range of the peak-width values is 1,398 nanometers and 1,754 nanometers. The average value is 1,561 nanometers; the median value is 1,579 nanometers; the standard deviation is 125 nanometers. A probability plot is shown in Figure 51; the peak-width values appear to be normally distributed, or approximately so.

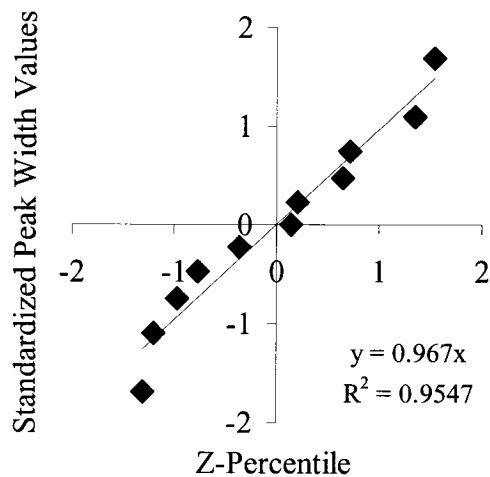


Figure 51. Normal probability plot of the peak-width values shown in Figure 50.

The average peak-width value of 1,561 nm and the nominal cantilever force constant value of 0.08 nN/nm were multiplied to calculate the adhesive force between the

PMMA-coated substrate and the Cloisite®-20A-coated colloidal probe. The average adhesive force to two significant figures is 120 nN. Adhesive forces measured using colloidal probes are often normalized to the radius of the spherical particle on the colloidal probe, which in this case is nominally five microns. The normalized value was calculated to be 25 mN/m. Szücs *et al.* measured an adhesive force of 65 mN/m between a colloidal probe coated with a montmorillonite and a silicon wafer coated with polydiallyldimethyl-ammonium chloride (PDDACl) [27]. They commented in their paper that the oppositely charged clay and polyelectrolyte adhered strongly to each other. In regard to the value measured in this study, it seems reasonable that the adhesive force measured between an organically-modified montmorillonite and PMMA is less.

#### 5.7.2 Force/Distance-Curves Experiment with PMMA on the Probe

A colloidal probe with 0.008 N/m force constant and a ten-micron diameter borosilicate particle was coated with PMMA by first silane-treating it with APTES and then dip-coating it in a 1% PMMA – toluene solution. To confirm that the borosilicate particle was coated, the top of the borosilicate particle was scanned using the Nano-R™ atomic force microscope when the probe was new and after the probe was coated. The scans consisted of a 2.2 μm scan followed by a 0.7 μm scan within an area of the 2.2 μm scan. Three-dimensional representations of the Z(SEN) data are shown in Figure 52 and Figure 53.



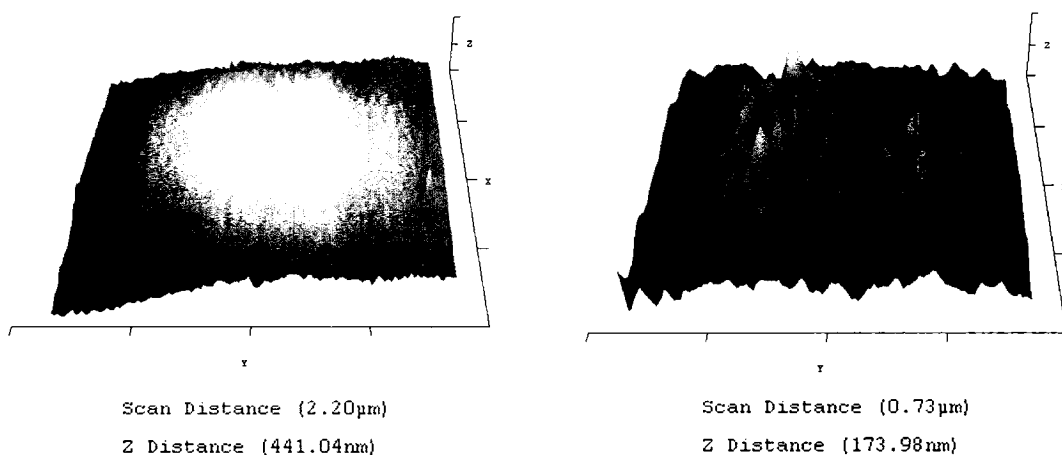


Figure 52. Three-dimensional images of 2.2 μm and 0.7 μm AFM scans of a borosilicate particle on a colloidal probe when it was new, before it was coated with PMMA. The aspect ratio is three.

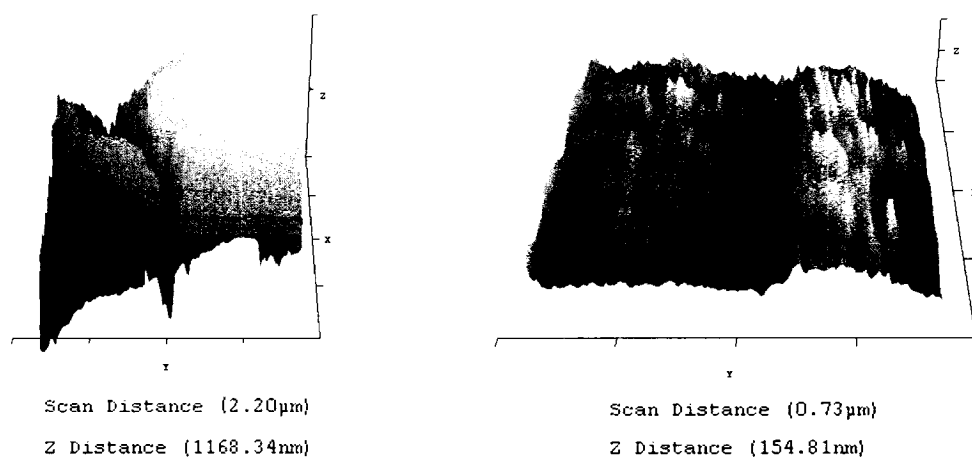


Figure 53. Three-dimensional images of 2.2 μm and 0.7 μm AFM scans of a borosilicate particle on a colloidal probe after silane treating it with APTES and dip-coating it in a 1% PMMA – toluene solution. The aspect ratio is three.

The latter of the two 2.2 μm scans has a fissure. The fissure appeared to be real; it was present in both the forward and reverse data channels of Z(SEN). It was not seen in the

2.2  $\mu\text{m}$  scan performed when the probe had not yet been coated, but the scan was performed at a different location on the borosilicate particle.

The two 0.73  $\mu\text{m}$  scans are similarly rough; the first scan has a roughness value of 14.9 nm RMS; the second scan has a roughness value of 14.6 nm RMS. One difference between the scans is that the surface structure in the second scan is finer. The difference does not seem to confirm the presence of a coating of PMMA, however. In order to confirm that the colloidal probe had been coated with PMMA, the probe was viewed through the video microscope on the Nano-R™. PMMA appeared to have formed terraces of different coating thicknesses on the cantilever around the borosilicate particle. The terraces appear to decrease in thickness with distance from the borosilicate particle. A 7.3  $\mu\text{m}$  scan was performed on an outer terrace. There were fissures adjacent to high areas in the scan. A 1.5  $\mu\text{m}$  scan was performed in the middle of the 7.3  $\mu\text{m}$  scan area; near a fissure. The scan captured the edge of a fissure. Both scans are shown in Figure 54.

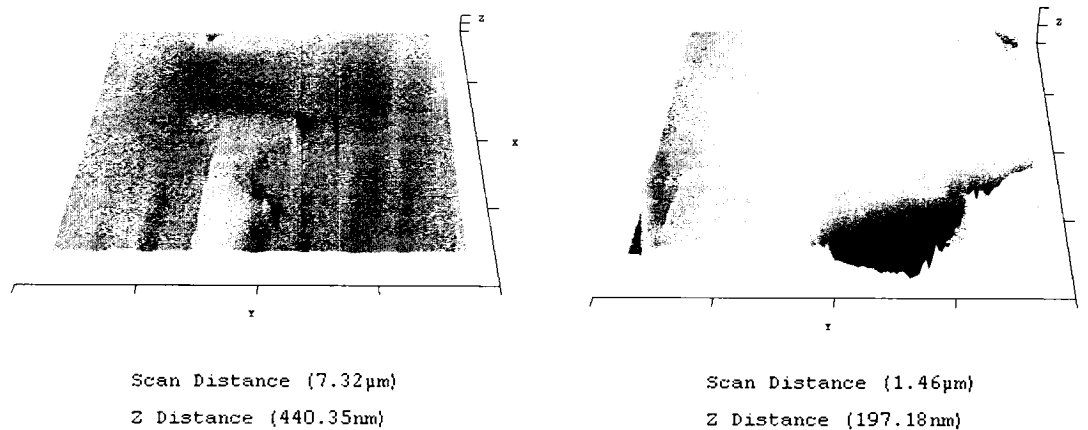


Figure 54. Three-dimensional images of a 7.3 μm scan (left) and a 1.5 μm AFM scan (right) of the cantilever of a colloidal probe in an area visibly coated with PMMA. The probe was silane-treated with APTES and then dip-coated in a 1% PMMA – toluene solution. The aspect ratio is three.

The discovery of fissures in an area of the cantilever that had a visible coating of PMMA was taken as evidence that the borosilicate particle was coated with PMMA, being that the borosilicate particle also had a fissure.

The colloidal probe was considered to be coated with PMMA. The probe was ready for force/distance curve measurements with a Cloisite® coating on a mica substrate. The Cloisite® 20A coating was made by drop casting a 3,200 ppm Cloisite® 20A - chloroform solution onto a mica substrate, at 22° C in air. This particular coating is described above, in Table 6 and Figure 28.

The force/distance-curve experiment was performed with the PMMA-coated colloidal probe and the Cloisite®-20A-coated substrate located inside the environmental cell. The flow of high-purity nitrogen gas was begun 38 minutes before the first curve was obtained; the flow was continued until the end of the experiment. Since the Cloisite®-20A coating was not smooth, it was scanned with the colloidal probe to

determine the topography. Three locations for obtaining force/distance curves were selected from the scan. A set of five force/distance curves were obtained per location. The scan and the locations are shown in Figure 55. The locations are numbered in the order in which the sets of force/distance-curve were performed.

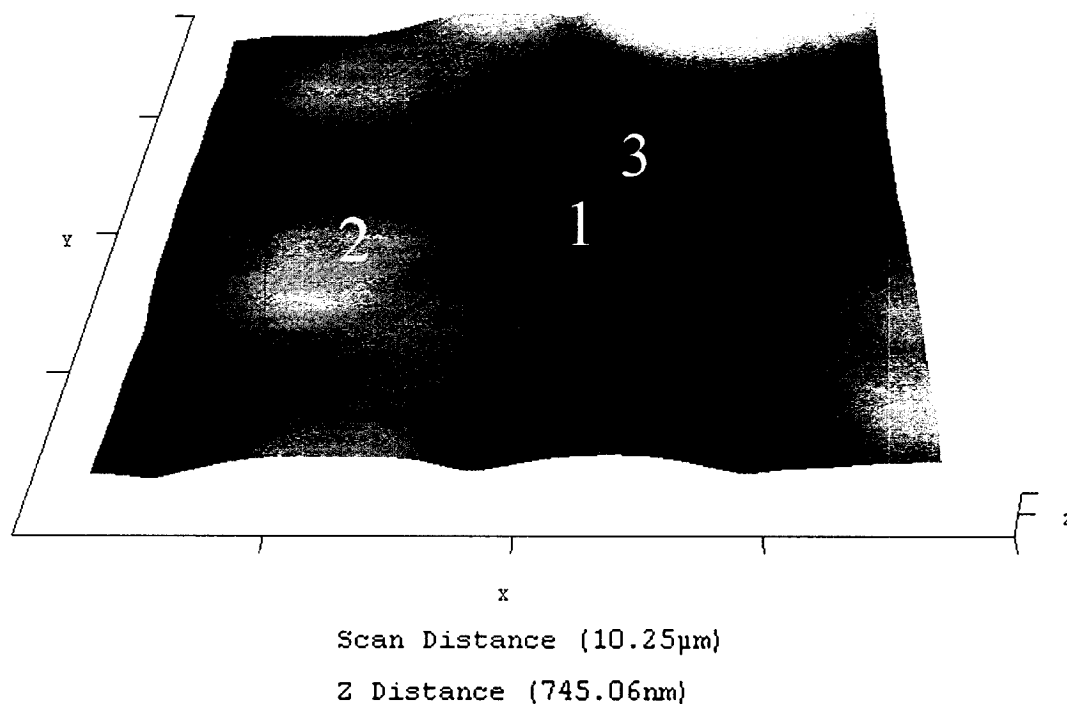


Figure 55. Three-dimensional representation of Z(ERR) obtained from a 10.2 µm scan of a mica substrate coated with Cloisite® 20A using a colloidal probe coated with PMMA. The aspect ratio is three.

The soft appearance of the scan is due to fact that it was scanned using a colloidal probe with a ten-micron-diameter spherical particle. The soft appearance suggests that the spherical particle did not have a protuberance on its surface where it interacted with the Cloisite® 20A surface during the scan. A protuberance can significantly increase scan resolution. A protuberance of PMMA was seen on a spherical particle of a colloidal probe on which EDX analysis was performed. See Figure 44 and Figure 45.

An ASCII data file was saved for every force/distance curve except the last one due to human error. The ASCII data files were processed to obtain Z(HGT) peak-width distances. The retract curves and peak-width values are shown in Figure 56, Figure 57, and Figure 58, corresponding three consecutive locations indicated on the scan.

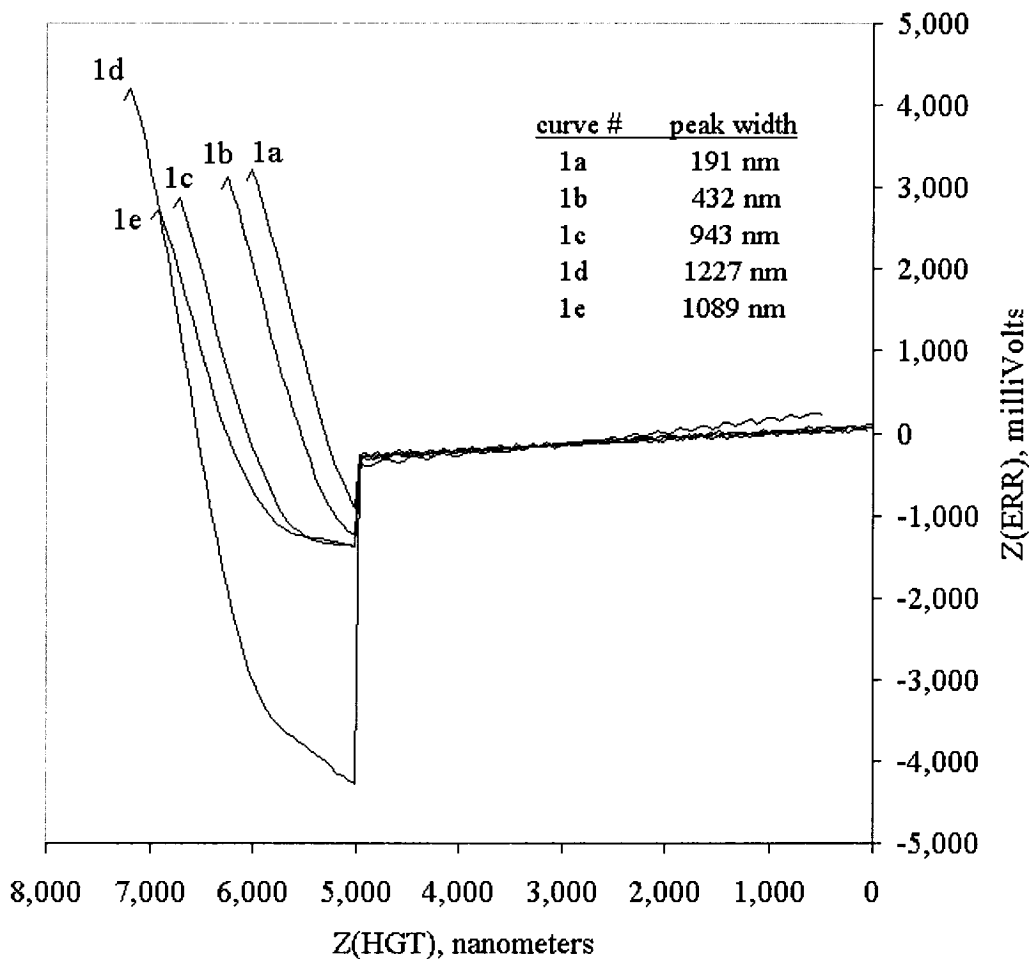


Figure 56. Force/distance retraction curves and corresponding peak-width values obtained between a colloidal probe coated with PMMA and a mica substrate coated with Cloisite® 20A. The curves (1a to 1e) were obtained from the location on the substrate marked “1” in Figure 54.

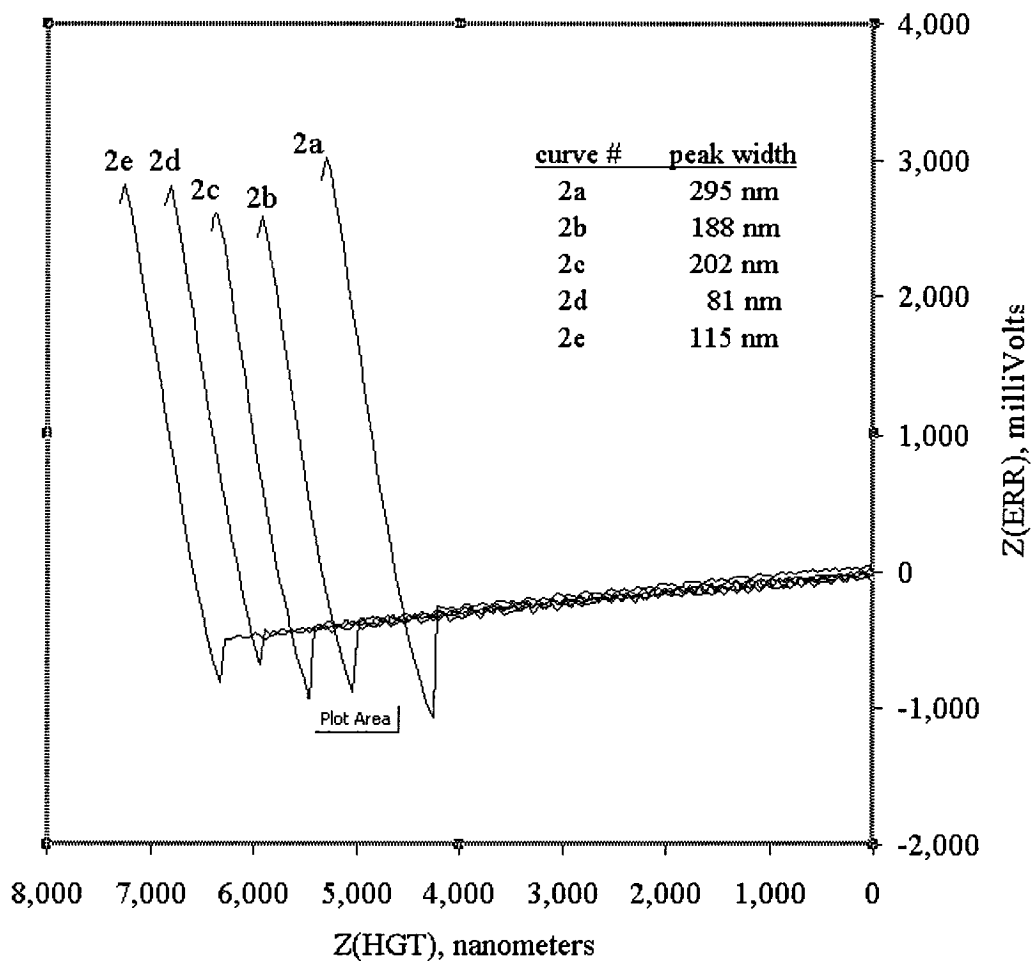


Figure 57. Force/distance retraction curves and corresponding peak-width values obtained between a colloidal probe coated with PMMA and a mica substrate coated with Cloisite® 20A. The curves (2a to 2e) were obtained from the location on the substrate marked “2” in Figure 54.

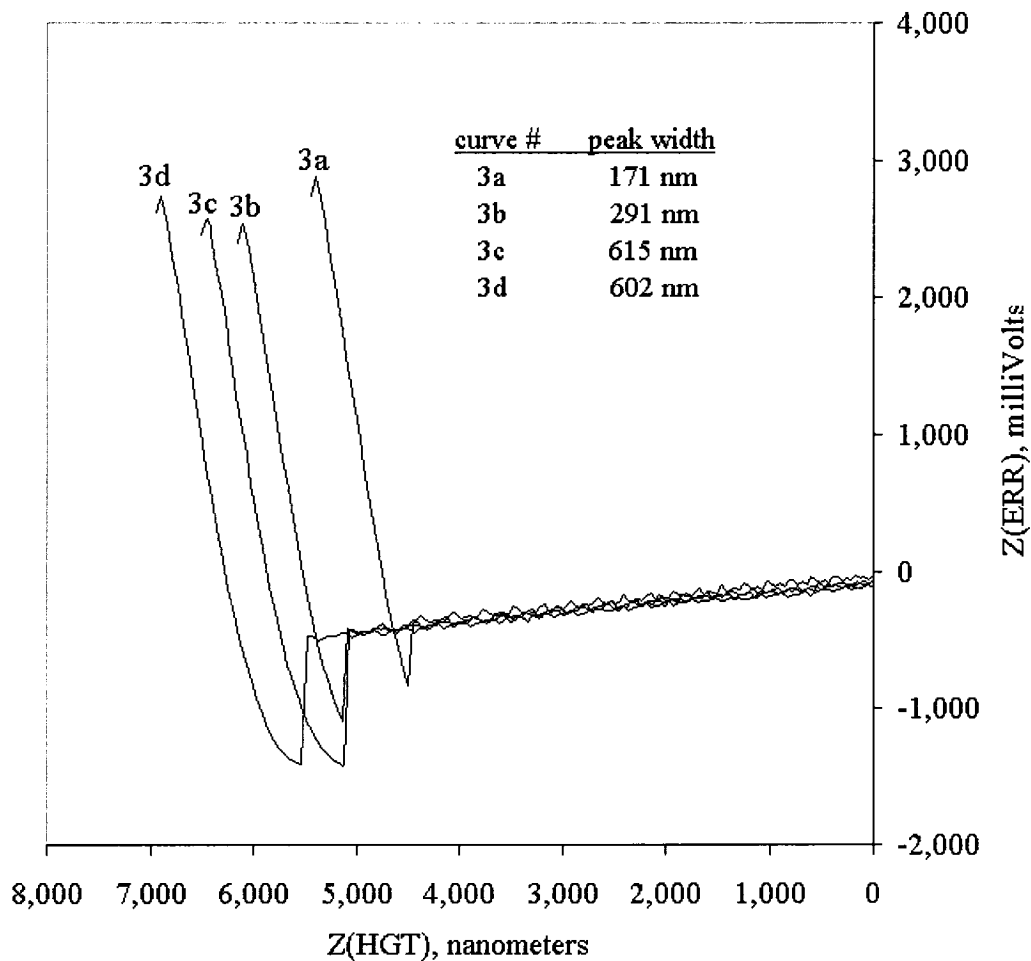


Figure 58. Force/distance retraction curves and corresponding peak with values obtained between a colloidal probe coated with PMMA and a mica substrate coated with Cloisite® 20A. The curves (3a to 3d) were obtained from the location on the substrate marked “3” in Figure 54.

The largest peak-width value obtained in nineteen force/distance curves was 1,089 nm. It was less than the smallest value obtained in the previous experiment (1,389 nm), in which the locations of PMMA and Cloisite® 20A were reversed. Also, there is considerable variation in the values; they range from 81 nm to 1,089 nm. The values vary considerably within each location. The values that correspond to the first location on the

scan, which appears plateau-like in the scan, increase significantly. The values corresponding to the second location, which also appeared plateau-like in the scan, appear to decrease. The values corresponding to the third location, which appears valley-like, appear to increase. An explanation is not offered as to why the peak-width values appear to increase in one location, and decrease in another. Because of the wide variation in peak width, the average peak-width was not calculated.

The results from the first experiment – where Cloisite® 20A was on the probe and PMMA was on the substrate – are significantly better than the results from the second experiment – where PMMA was on the probe and Cloisite® 20A was on the substrate. The pull-back voltages and peak-width values obtain in the first experiment had significantly less scatter, both in repeated force/distance curves in the same location and in force/distance curves obtained at different locations.

### 5.7.3 Interpretation of the Results of the Placement Option Experiments

In late 2006, Drelich reported results and conclusions from adhesive force measurements conducted between colloidal probes and substrates in which the roughness of both were varied [57]. Both deformable and rigid materials were used. Imperfections in solid surfaces were confirmed to be a major cause of scatter in measured force adhesion values. The actual area of contact between rough surfaces is reduced. One finding was that theoretical models for rough surfaces can be used with measured parameters that describe the characteristics of a surface to normalize the measured surfaces. Another finding, which is applicable to this project, was that with a deformable



material, sufficient loading of a colloidal probe onto a surface can result in the elimination of the effect of roughness, especially roughness on the nanometer scale.

Drelich's conclusions may explain the results obtained with Cloisite® 20A and PMMA. In the case of the colloid probe coated with Cloisite®20A, the coating was rough – on the order of 14 nm in the 0.73  $\mu\text{m}$  probe-on-probe scan shown in Figure 49. When the force/distance curves were obtained, the borosilicate particle may have been pressed sufficiently hard onto the thick, smooth, and compliant PMMA coating to conform the PMMA surface to the imperfections of the Cloisite® 20A coating on the borosilicate particle. The result of that process would be little variation in contact area in each force/distance-curve trial. Drelich also provided some guidance on determining the appropriate amount of loading force to achieve sufficient deformation.

Drelich's explanation also provides a potential explanation in the case of the colloidal probe coated with PMMA, in which a relatively thin coating of PMMA came in contact with a relatively stiff Cloisite® 20A coating of micron-scale roughness. Neither coating was able to conform sufficiently. The result was a large variation in contact area in the force/distance-curve trials.

In conclusion, the placement of organoclay on borosilicate particles rather than mica substrates is the better choice. Force/distance curves with relatively little variation in adhesion force were obtained with Cloisite® 20A located on a probe. In contrast, force/distance curves with Cloisite® 20A located on a substrate showed significant variation.

## 5.8 Environmental Factors

The argument presented for the colloidal probe technique was that it offered good control over the many factors that affect the interactions between polymers and clays. Being that the interaction of interest is adhesive force, it makes sense to identify and mitigate the environmental factors that impact the measurement of adhesive force between OMMTs and polymers on an AFM.

The environmental factors that can impact adhesive force appear to come from two sources. One source is the factors that affect the properties of polymers, OMMTs, and polymer-clay nanocomposites. These factors include water vapor, solvents, temperature and temperature cycling, solvents, chemical attack, aging and decomposition, and stress. They are an issue during sample preparation and storage. An example is the decomposition of nylon 6 at 200° C in the presence of water during coating, and the absorption of water by the nylon 6 coating from air afterwards. Such factors largely affect the entire mass of a material in contact with the environment. They can affect the actual adhesive forces between clay and polymer in a nanocomposite. No experiments were performed to investigate these factors. They were mitigated by using clear glassware in the preparation of stock solutions, and keeping samples at room temperature in sealed containers with desiccant.

The other source of environmental factors is the colloidal probe technique itself. The technique brings a spherical surface and a flat surface into contact; the technique therefore introduces roughness as a potential factor. It introduces other factors, which are generally localized to the point of contact of two surfaces. They impact the ability to

accurately measure the actual adhesive force, or change the actual adhesive force in the course of measuring it. According to Kappl and Butt, the factors include loading force, contact time, humidity, temperature, and surface roughness [34]. They pertain directly to the hypothesis – that the colloidal probe technique is a useful tool for studying the interactions between polymers and OMMTs.

The approach taken toward the factors described by Kappl and Butt was to minimize them or keep them constant. An attempt was made to mitigate the effect of roughness by making smooth coatings. To minimize the effects of humidity, experiments were carried out in an environmental cell that was continuously purged with dry nitrogen. Temperature effects were not explored; experiments were carried out at room temperature. To minimize the effect of loading force and contact time, the same settings of the Z(ERR) deflection limit and time rate were used throughout. The intent to minimize the effect of loading force was compromised by failure to always locate the Z(ERR) baseline value near zero volts. If a baseline was at -1,000 mV, then effective Z(ERR) deflection limit was 3,000 mV; the loading force was increased by a factor of 1.5.

## 5.9 Adhesive Force Experiments

The final objective was to perform adhesive force measurements between OMMTs and polymers using coated colloidal probes and substrates. Based on the results discussed in Section 5.8 Placement Option Experiments, experiments were performed with OMMTs coated on colloidal probes and polymers coated on substrates. The results

in Section 5.8 demonstrated repeatable adhesive force measurements between a probe coated with Cloisite® 20A and a substrate coated with PMMA.

Three exploratory experiments were performed to confirm repeatability and to check whether adhesive force measurements obtained using different coated probes and different coated substrates produced reasonable values compared to the earlier result obtained between Cloisite® 20A and PMMA. The adhesive force measurements were also compared to the value reported by Szücs *et al.* and to a value calculated using the JKR model. Significantly higher adhesive forces were measured. The results are interpreted with regard to the hypothesis that colloidal probe technique can be used on an AFM to study the interfacial interactions between OMMTs and polymers

A final set of adhesive force measurements, designed to determine whether the adhesive forces measured between different sets of OMMTs and polymers can be positively correlated to the known compatibility of each set for processing into nanocomposites, was not completed.

#### 5.9.1 Exploratory Experiment One

The first exploratory experiment was performed immediately after the force/distance curves were obtained for the experiment described in Section 5.7.1, the placement option experiment in which Cloisite® 20A was placed on the probe. The colloidal probe was used again for the exploratory experiment. A mica substrate was coated with PE-MA by drop casting a 1 wt% PE-MA – toluene solution onto the substrate inside an oven set at 100° C. The solution had been preheated to 100° C. Immediately after the drop was cast, the substrate was covered with a jar to slow the rate

of evaporation. The experiment was performed before the technique for casting smooth PE-MA coatings had been developed.

A total of eleven force/distance curves were obtained and recorded. They were obtained in two locations on the coating. Retraction curves and Z(HGT) peak-width values are shown in Figure 59 and Figure 60.

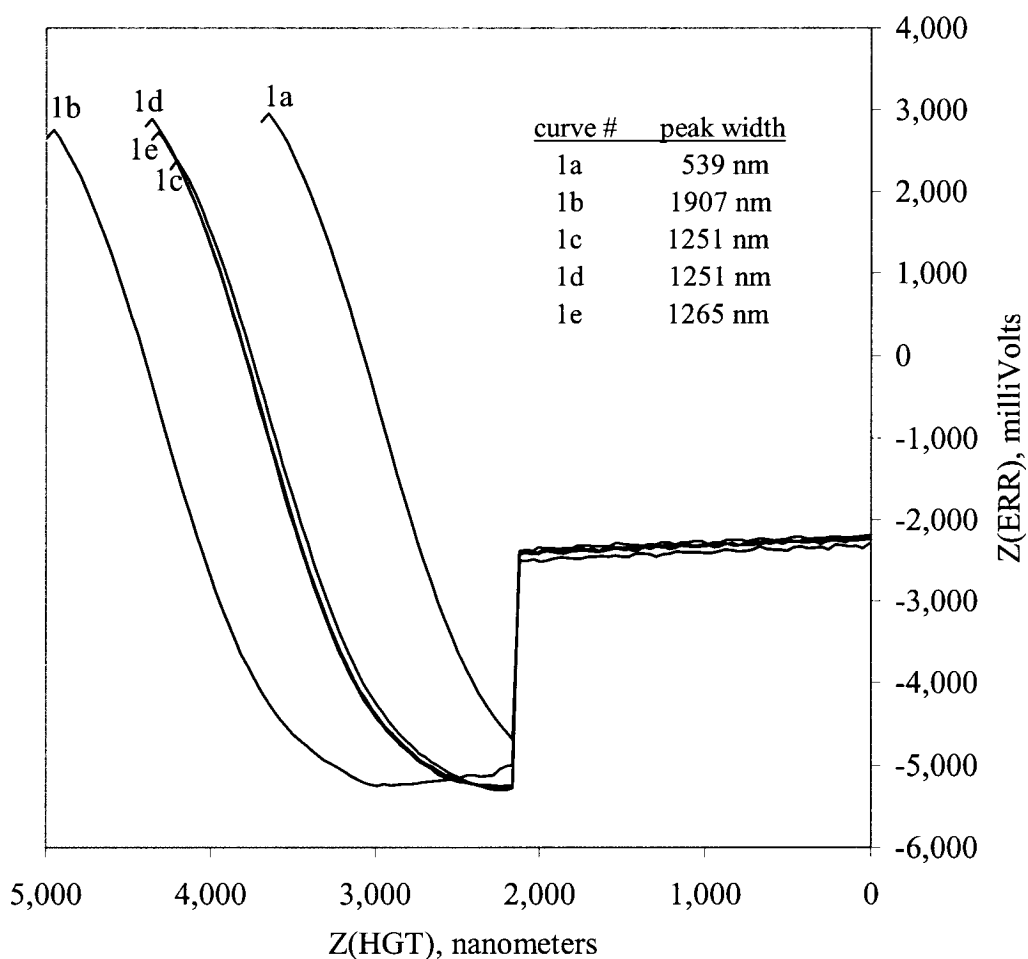


Figure 59. Force/distance retraction curves and corresponding peak-width values obtained between a colloidal probe coated with Cloisite® 20A and a mica substrate coated with PE-MA. The curves (1a to 1e) were obtained from the same location.

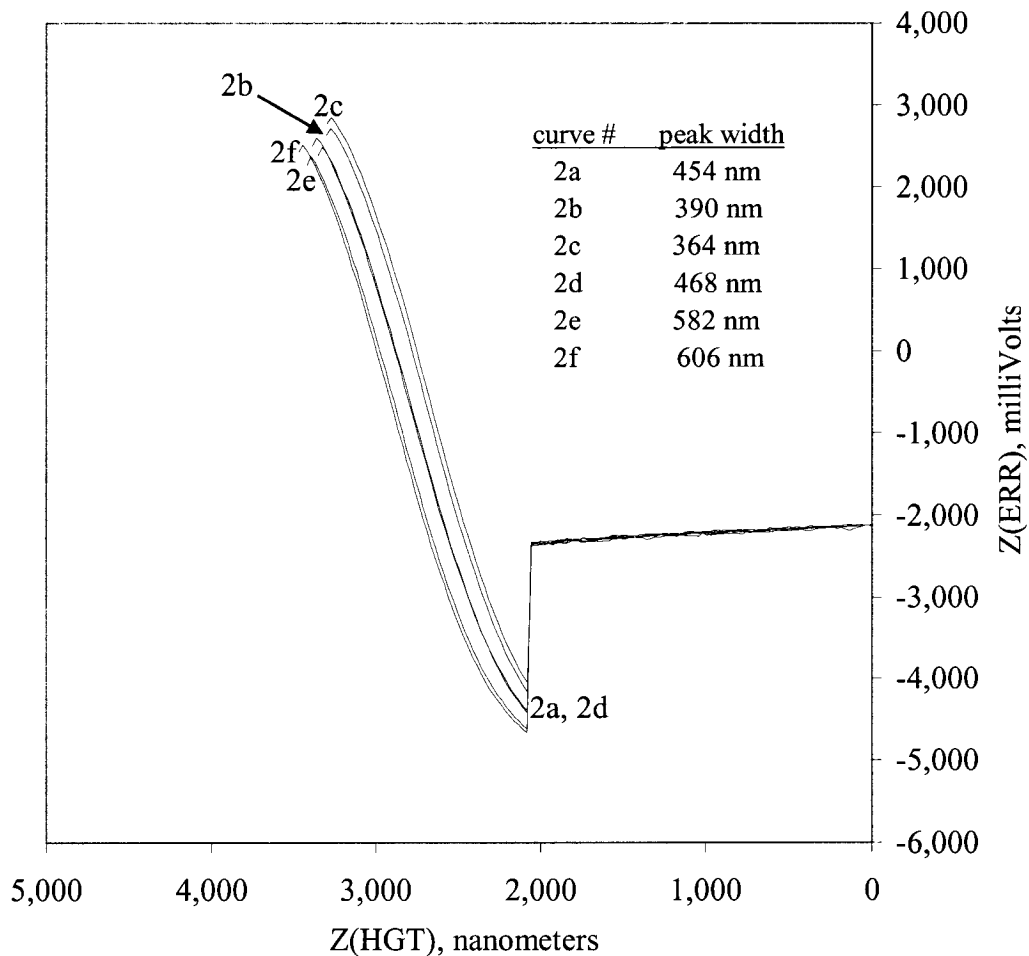


Figure 60. Force/distance retraction curves and corresponding peak-width values obtained between a colloidal probe coated with Cloisite® 20A and a mica substrate coated with PE-MA. The curves (2a to 2e) were obtained from the same location.

The peak-width values vary significantly within and between the two locations. The smallest peak-width value is 364 nm. The largest peak-width value is 1,907 nm; it is greater than the largest value obtained between the same colloidal probe and the PMMA coating in the placement-option experiment, which was 1,745 nm.

The PE-MA coating was scanned using the Cloisite®-20A-coated colloidal probe. A roughness value from the 10.2  $\mu\text{m}$  scan was obtained; it was 27.4 nm RMS. A three-dimensional representation of the Z(SENS) data is shown in Figure 61.

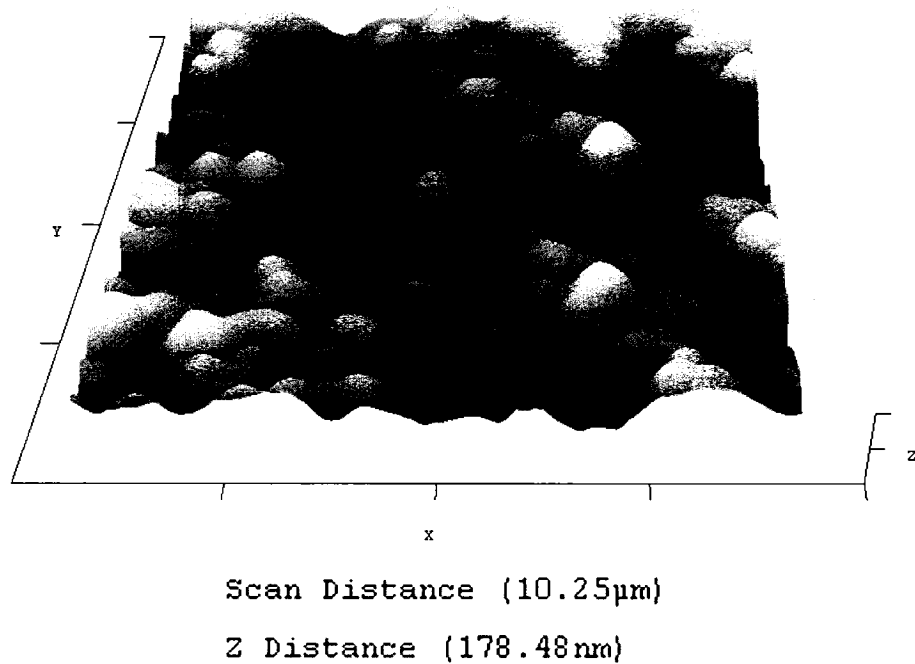


Figure 61. Three-dimensional representation of Z(SENS) obtained from a 10.2  $\mu\text{m}$  scan of a mica substrate coated with PE-MA using a colloidal probe coated with Cloisite® 20A. The nominal force constant of the probe was 0.08 N/m; the nominal diameter of the borosilicate particle was ten microns. The aspect ratio of the image is 20.

The large scatter in the peak-width values was attributed to the roughness of the PE-MA coating. The conclusion was made that smoother coatings of PE-MA and nylon 6 were needed.

The resolution of Figure 61 appears to be 1 to 2  $\mu\text{m}$ . Ordinarily, a colloidal probe with a ten-micron diameter sphere is limited to a resolution of 4 to 5  $\mu\text{m}$ . Figure 55 is more typical of the type of image that can be obtained with a colloidal probe. The higher

resolution of Figure 61 indicates the presence of an asperity on the borosilicate particle of the probe used in the experiment.

### 5.9.2 Exploratory Experiment Two

The second exploratory experiment was performed after smooth coatings of nylon 6 and PE-MA had been made. A colloidal probe with a force constant of 0.08 N/m and a borosilicate particle of five-microns diameter was silane-treated with EPPMS and dip-coated in 3,200 ppm Cloisite® 25A – NMP. Force/distance curves were obtained between the probe and the smooth PE-MA coating described at the end of Section 5.4. A total of seven curves were obtained, over three locations. The amount of interaction appeared to be consistent among the curves. Unfortunately, the interaction between the colloidal probe and the PE-MA coating was too great. The colloidal probe had large negative deflections on both the approach and the retract curve. The large negative deflection in the approach curve is associated with stiction. See Figure 62.



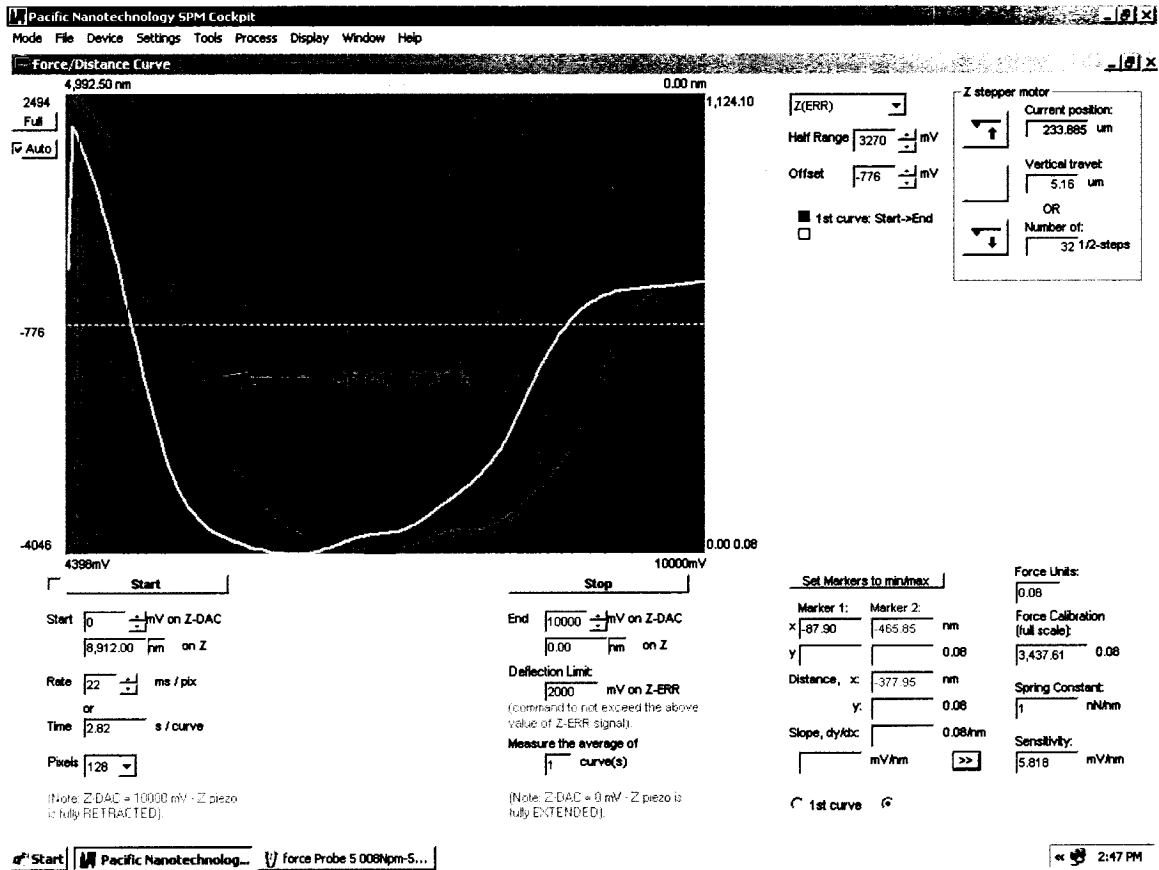


Figure 62. Force/Distance Curve window of the Nano-R™ SPM Cockpit software, between a colloidal probe coated with Cloisite® 25A and a smooth coating of PE-MA on a substrate. The nominal force constant of the probe was 0.08 N/m; the nominal diameter of the borosilicate particle was five microns.

The lack of an adequate baseline prevented the calculation of peak-width values. The conclusion was made that the force constant of the probe was too small. Colloidal probes with stiffer cantilevers were needed; probes with nominal force constant 0.6 N/m were ordered.

### 5.9.3 Exploratory Experiment Three

The third exploratory experiment was performed after a set of colloidal probes with a nominal force constant of 0.6 N/m were obtained. The diameter of the

borosilicate particles was five microns. Two of the probes were silane-treated with EPPMS. The first of the two silane-treated probes was dipped in NMP. The second of the two silane-treated probes was dip-coated in 3,200 ppm Cloisite® 25A – NMP. The probes were allowed to dry. The first probe served as a control for the second – to see whether dip-coating in the Cloisite® 25A solution resulted in a difference.

Force/distance curves were obtained between the two probes and the substrate with the smooth PMMA coating.

A total of fifteen force/distance curves were obtained using the probe that was dipped in NMP. The curves were obtained over three locations. The interaction was substantial, but the curves were consistent and the peak-width values showed little variation within the location and between locations. Figure 63 shows the five retraction curves and peak-width values obtained at the first location. Figure 64 shows the first retraction curves and peak-width values obtained at each of the three locations.

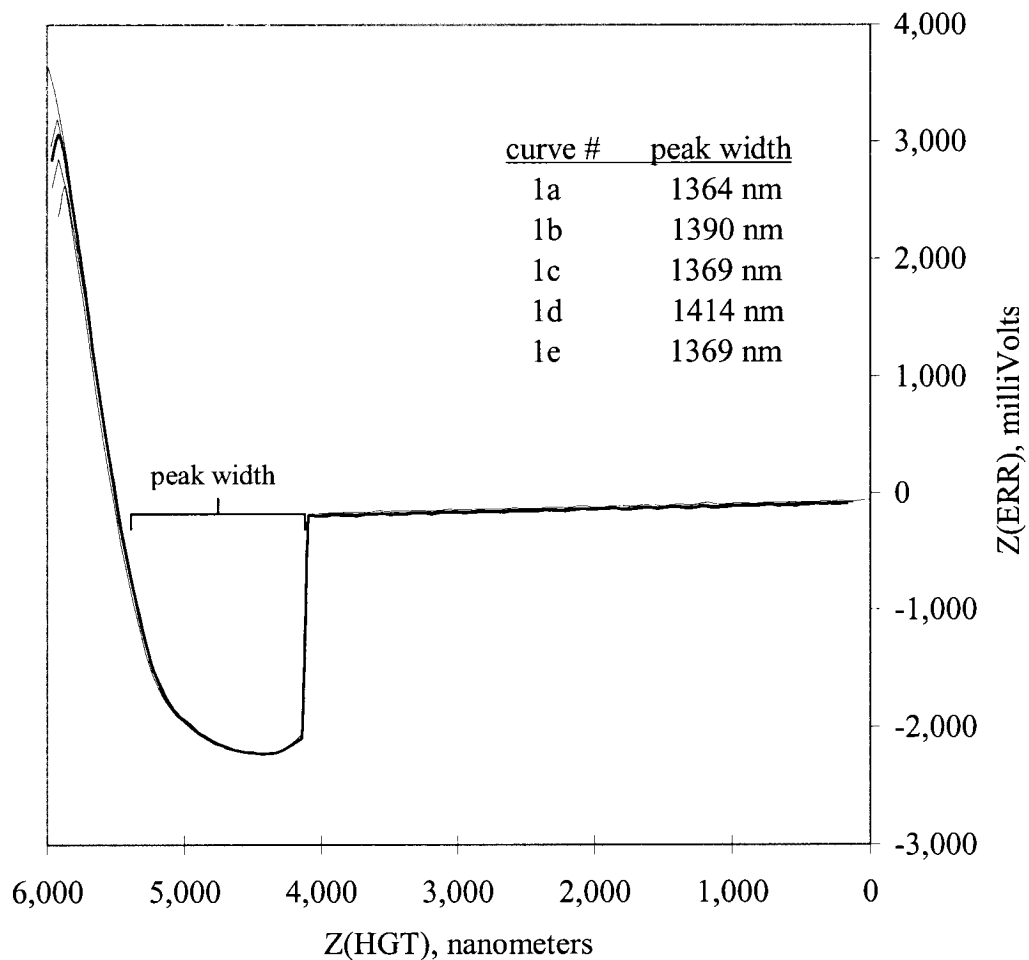


Figure 63. Force/distance retraction curves and corresponding peak-width values obtained between a colloidal probe silane-treated with EPPMS and a mica substrate coated with PMMA. The curves (1a to 1e) were obtained from the same location. The nominal force constant of the probe was 0.6 N/m; the nominal diameter of the borosilicate particle was five microns.

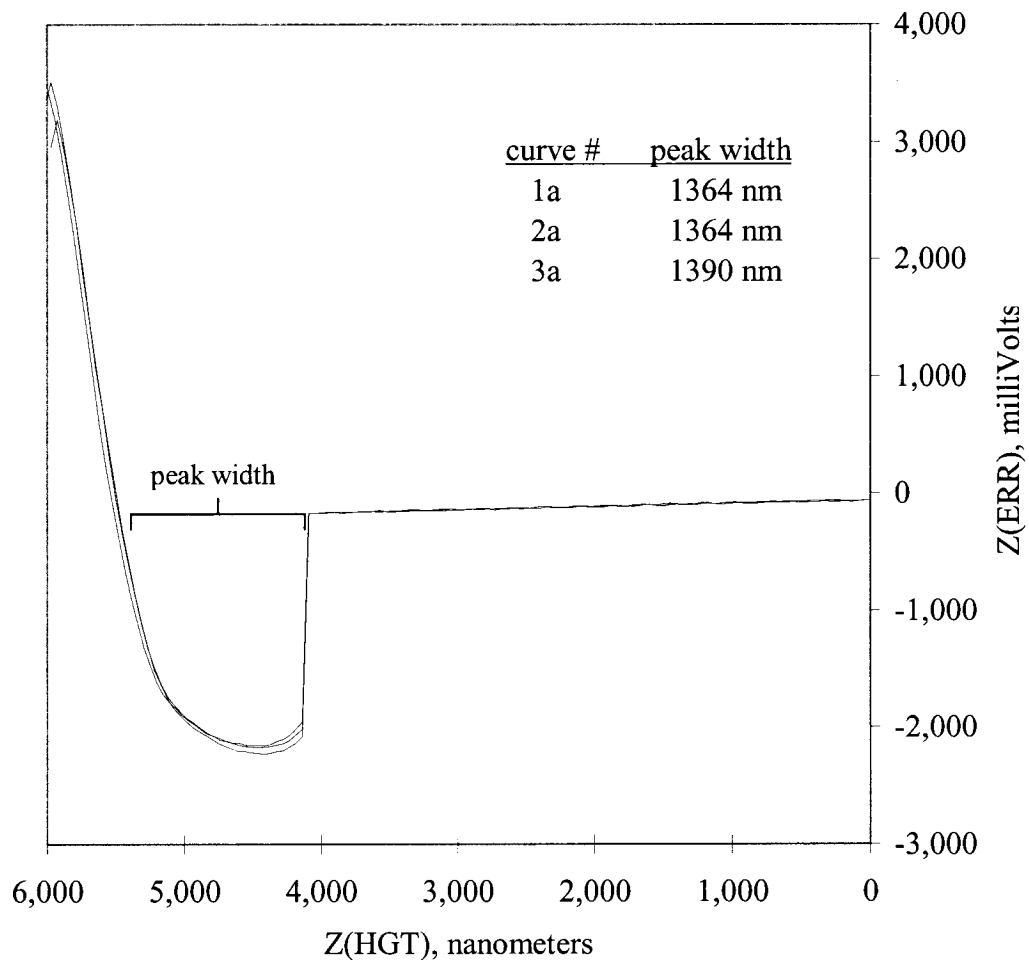


Figure 64. Force/distance retraction curves and corresponding peak-width values obtained between a colloidal probe silane-treated with EPPMS and a mica substrate coated with PMMA. The curves (1a, 2a, and 3a) were obtained in different locations. The nominal force constant of the probe was 0.6 N/m; the nominal diameter of the borosilicate particle was five microns.

The similarity of the peak-width values in Figure 63 and Figure 64 indicates that adhesive force measurements between the silane-treated probe and the PMMA-coated substrate were repeatable at the same location and at different locations on the PMMA coating. The median value of the peak-width from the five retraction curves obtained in

the first location was 1,369 nm, which corresponds to a normalized adhesive force of -328 mN/m.

A total of twenty-five force/distance curves were obtained using the probe that was dipped in the Cloisite®-25A solution. The curves were obtained at five locations. The quality of the force/distance curves was poor. In the initial curves, both the approach curve and retraction curve showed negative probe deflections. Also, the base line was poor. See Figure 65 for the first curve obtained in the first location.

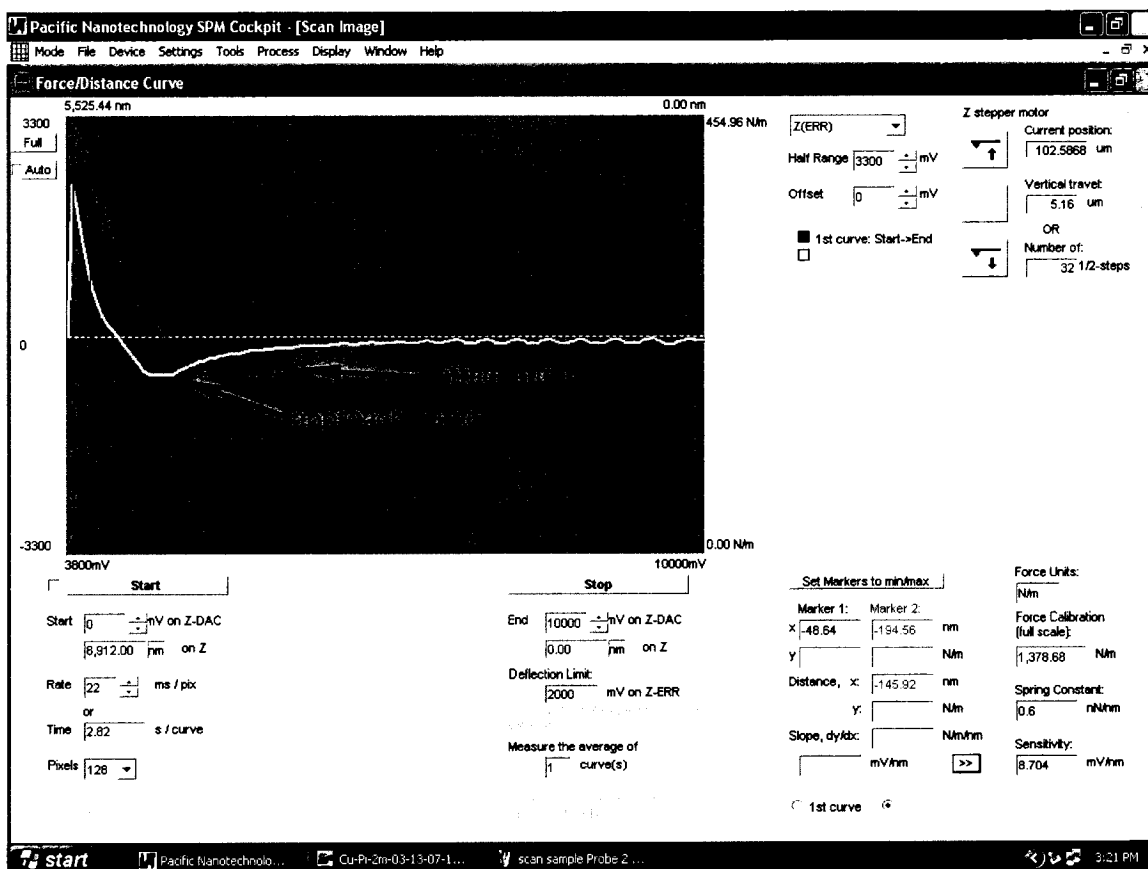


Figure 65. SPM Cockpit Force/Distance Curve window, showing a poor-quality force/distance curve.

The poor quality of the curves was attributed to specular reflections on the back of the probe cantilever. The specular reflections were caused by clusters of OMMT, which

were deposited on the cantilever when the probe was dip-coated. The position of the laser spot on the cantilever was adjusted for each set of five force/distance curves. The fifth set had the best quality curves. They were produced with the laser spot positioned in the middle of the cantilever's length. See Figure 66.

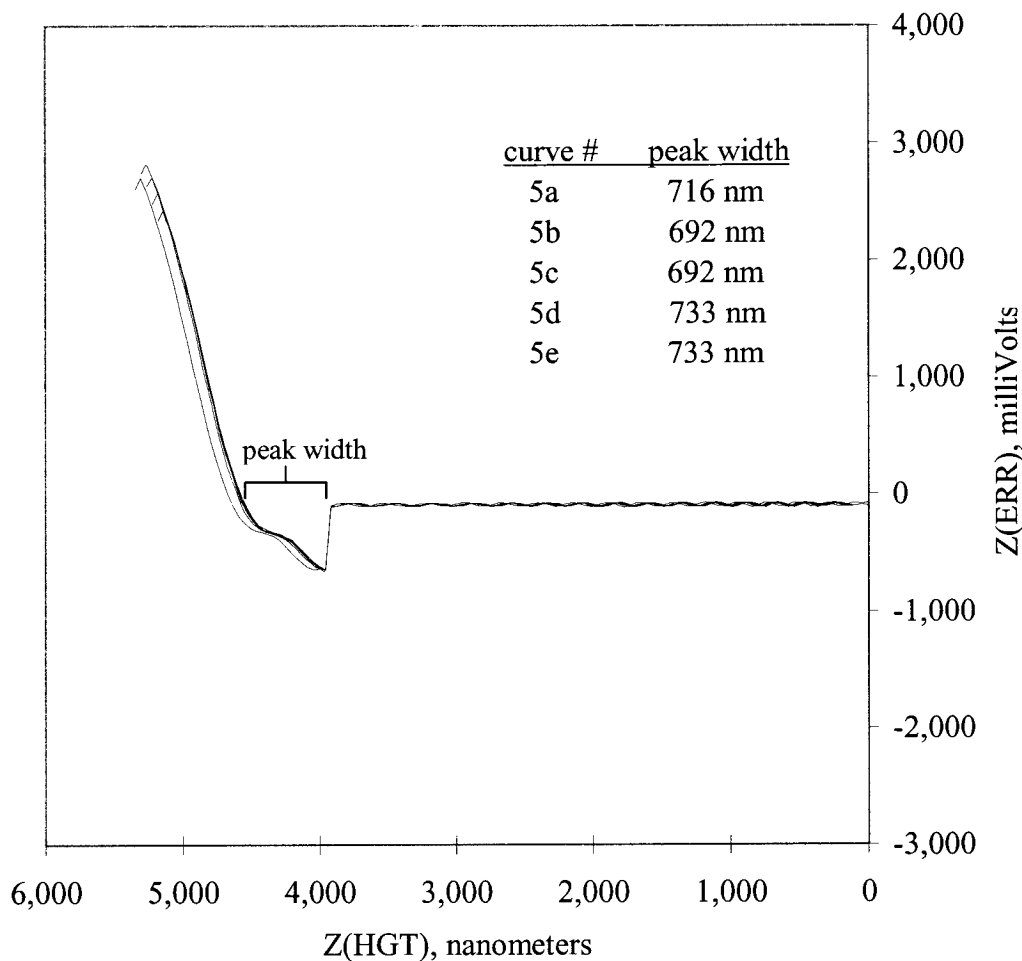


Figure 66. Force/distance retraction curves and corresponding peak-width values obtained between a colloidal probe silane-treated with EPPMS and coated with Cloisite® 25A and a mica substrate coated with PMMA. The curves (5a to 5e) were obtained from the same location.

For comparison, the Z(HGT) scale and Z(ERR) scale in Figure 66 are the same as Figure 65. The interaction of the Cloisite®-25A coated probe with the PMMA surface is

clearly less than the interaction of the probe that was only silane-treated and dipped in NMP. The peak-width values are about half. The median value is 716 nm. The normalized adhesive force is -170 mN/m. The value is nearly an order of magnitude higher than the -25 mN/m reported for a Cloisite®-20A-coated probe and PMMA in Subsection 5.7.1 Force/Distance-Curves Experiment with OMMT on the Probe. The value is more than double the -65 mN/m reported by Szücs *et al.* for a colloidal probe coated with a montmorillonite and a silicon wafer coated with polydiallyldimethylammonium chloride (PDDACl) [27]. It seems unlikely that the adhesive force between a moderately-hydrophobic organoclay and neutral polymer is greater than the adhesive force between a negatively-charged montmorillonite and a positively-charged polycation. The latter pair is expected to have some electrostatic interaction.

The two probes were scanned over the TGT1 tip characterization grating. A 10.25  $\mu\text{m}$  scan was performed with the first probe, which was silane-treated and dipped in NMP. It was the first scan done over the grating in this study. The diameter of the borosilicate particle was checked using Line Analysis in the NanoRule+ software; it was 5.4  $\mu\text{m}$ , which is slightly greater than the nominal diameter of 5  $\mu\text{m}$ . The Z(ERR) and Z(SEN) data were analyzed for evidence of asperities on the surface of the borosilicate particle; see Figure 67.

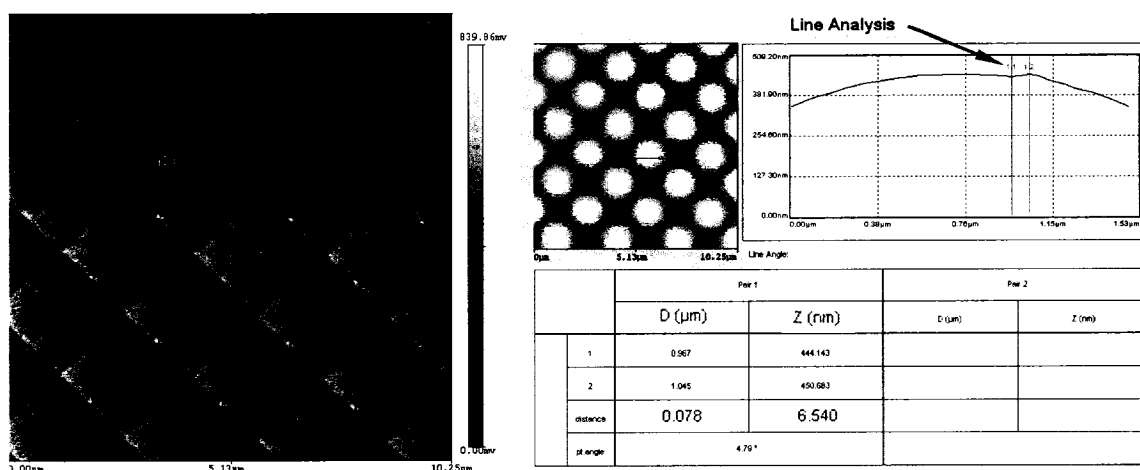


Figure 67. Contrast-brightness display of Z(ERR) on the left and line analysis of Z(SEN) on the right of a 10.2 μm scan of a colloidal probe silane-treated with EPPMS and dipped in NMP, and then used to obtain force/distance curves with a PMMA-coated substrate.

The contrast-brightness display shows asperities on the surface of the borosilicate particle. One of the larger asperities is indicated on the left side of Figure 67. Line analysis was performed on the Z(SEN) data in the location of the indicated asperity. The asperity was approximately 0.16 μm in diameter and 7 nm tall. The minimal height of the asperity means that it probably did not prevent the surrounding area from contacting the PMMA surface.

A 5.1 μm scan was performed on the second probe, which was silane-treated with EPPMS and dip-coated in 3,200 ppm Cloisite® 25A – NMP, and then used to obtain force/distance curves. The diameter was checked using Line Analysis in the NanoRule+ software; it was 4.9 μm, which is close to the nominal diameter of 5 μm. The Z(ERR) and Z(SEN) data were analyzed for evidence of a coating of Cloisite® 25A and roughness on the surface of the borosilicate particle; see Figure 68.



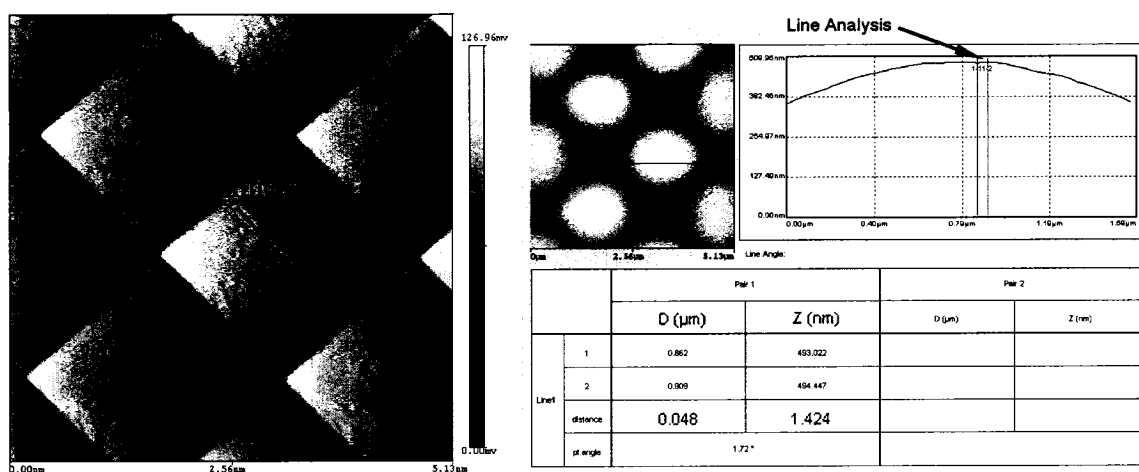


Figure 68. Contrast-brightness display of Z(ERR) on the left and line analysis of Z(SEN) on the right of a 5.1  $\mu\text{m}$  scan of a colloidal probe silane-treated with EPPMS and dip-coated in 3,200 ppm Cloisite® 25A, and then used to obtain force/distance curves with a PMMA-coated substrate.

Texture visible in the contrast-brightness display of Z(ERR) suggests that the borosilicate particle was at least partially coated with Cloisite® 25A. Line analysis was performed on the Z(SEN) data at the edge of an area of texture indicated by the arrow labeled “roughness” on the left side of Figure 68. The change in height from the edge of the rough area to 0.048  $\mu\text{m}$  to the right into the rough area was only 1.4 nm. The minimal change in height suggests that the higher rough area did not prevent the smoother area to the left of it from contacting the PMMA coating. Based on this analysis and the contrast-brightness display of Z(ERR), it appears that the good contact was achieved between the probe and the PMMA coating.

#### 5.9.4 Interpretation of Results

For comparison, a theoretical pull-off force (same as adhesive force) was calculated using the JKR model and Equation 1 described in Subsection 2.3.6 of Chapter Two. A normalized version Equation 1 with added subscripts is shown as Equation 4.

$$F/R = -(3/2)\pi W_{12} \quad \text{Equation 4}$$

R is the radius, and  $W_{12}$  is the adhesion work term between a material designated by subscript 1 and a material designated by subscript 2. According to Reitsma et al.,  $W_{12}$  is often calculated using surface-energy values using the equation shown in Equation 5 [33].

$$W_{12} = 2(\gamma_1\gamma_2)^{0.5} \quad \text{Equation 5}$$

A surface energy value was available for the surfaces treated with the silane coupling agent EPPMS; the value was 42.5 mN/m [46]. A surface energy value was available for PMMA; the value was 39.0 mN/m [58]. Calculating  $W_{12}$  from Equation 5 and substituting the value into Equation 4 yields the theoretical normalized adhesive force of -384 mN/m.

The normalized adhesive force reported in Subsection 5.9.3 Exploratory Experiment Three for the silane-treated probe and the PMMA-coated substrate was -328 mN/m; it is similar the theoretical value of -384 mN/m. The similarity between the values suggests that the later normalized adhesive-force measurement of -170 mN/m (obtained between the probe coated with Cloisite® 25A and the substrate coated with PMMA) is more correct than the normalized adhesive-force measurement of -25 mN/m obtained earlier (between the probe coated with Cloisite® 20A and the substrate coated

with PMMA). The similarity between the values also calls into question the accuracy of the value of  $-65 \text{ mN/m}$  reported by Szücs *et al.* (for a colloidal probe coated with a montmorillonite and a silicon wafer coated with polydiallyldimethylammonium chloride (PDDACl) [27]).

The result of the second exploratory experiment reported in Subsection 5.9.2 supports the interpretation that the  $-25 \text{ mN/m}$  value obtained earlier is inaccurate. In the experiment, a colloidal probe was coated with Cloisite® 25A. The nominal force constant of the probe was  $0.08 \text{ N/m}$  – the same as the probe used to measure the  $-25 \text{ mN/m}$  value; the nominal diameter of the borosilicate particle was five microns. The interaction between the probe and a PE-MA was too great to measure, which means that it was significantly greater than the  $-25 \text{ mN/m}$  value, which was obtained with a probe with the same nominal force constant but with a borosilicate particle that was ten microns in diameter. If the interaction in the experiment had been close to  $-25 \text{ mN/m}$ , then the smaller nominal diameter of the borosilicate particle on the colloidal probe would have reduced the deflections experienced by the probe to about half. Instead, the deflections were large – too large to measure with the probe.

The result of the first exploratory experiment reported in Subsection 5.9.1 also supports the interpretation that the  $-25 \text{ mN/m}$  value is inaccurate. The experiment was performed with the probe that was used to obtain the  $-25 \text{ mN/m}$  value. The probe was used to perform a scan of a PE-MA coating at the end of the experiment. The unexpectedly high resolution obtained in the scan indicated that an asperity was present on the probe. An asperity can significantly reduce the contact area between a probe and a

substrate, resulting in reduced interaction. An asperity that was sufficiently large to affect the resolution of a scan was sufficiently large to reduce the contact area between the probe and a substrate during interaction measurements. Thus, the -25 mN/m value is explained as being too low as a result of the presence of an asperity on the probe.

The conclusion of this analysis is that the colloidal probe technique can be used on an AFM to study the interfacial interactions between OMMTs and polymers. Reasonable agreement was obtained between the theoretical interaction and the measured interaction for EPPM and PMMA. The similarity in the values lent credibility to the technique that was used to measure adhesive force. The normalized adhesive force measured between Cloisite® 25A and PMMA was similar in magnitude to the value measured between EPPM and PMMA, and a subsequent scan of the probe verified the presence of a coating of Cloisite® 25A on the probe. The lack of significant asperities on the probe meant that good contact was achieved between the coating on the probe and the PMMA coating on the substrate. It can be concluded with reasonable confidence that the adhesive force between Cloisite® 25A and PMMA was measured.

#### 5.10 Suggestions for Future Work

This study created a foundation for future work. Future work might involve establishing reproducibility of adhesive force measurements between the three grades of Cloisite® and the three polymers. Future work might include the correlation experiment that was envisioned for this study. If accurate adhesive force measurements are a goal, then it is recommended that the diameter of borosilicate particles and force constants of colloidal probes be measured. It is also recommended that  $Z(HGT)$  on the AFM be

profiled using calibration gratings, and the tilt at which probes contact a substrate be taken into account.

Environmental effects can be studied, especially the effects introduced by the colloidal probe technique. For example, the minimum level of loading force to negate the effects of roughness of the coatings might be determined. Also, the sensitivity of adhesive force measurements to the rate at which force/distance curves are conducted might be measured.

Further development or improvement of the technique used to coat probes with OMMT is suggested. The dip-coating technique used in this study allowed clusters of OMMT to form on the back of probe cantilevers. The clusters caused specular reflections, which degraded the Z(ERR) signal from the light-lever system. For simplification of procedures, the solvent NMP and the silane coupling agent EPPM might be used with all three grades of Cloisite®. Also, cleaning colloidal probes in a plasma-cleaning system might replace silane treatment.

The methods used to confirm and characterize OMMT coatings on probes can be improved. EDX analysis might work better if aluminum could be used instead of magnesium to signal the presence of OMMT. EDX analysis can be performed after a probe is scanned over a TGT1 tip characterization grating; it might be interesting to compare the results from the two techniques. Also, perhaps there is an analytical technique available that was not tried in this study.

## CHAPTER SIX CONCLUSIONS

The overall conclusion of this study is that the colloidal probe technique can be used on an atomic force microscope (AFM) to study the interfacial interactions between organically-modified montmorillonites (OMMTs) and polymers. The objectives designed to test the hypothesis were largely met. Objectives that were met include developing techniques for coating three polymers onto mica substrates and coating three OMMTs onto colloidal probes, and measuring adhesive interaction between them. One objective was not completed; it required the measurement of adhesive forces between nine different OMMT-polymer pairs for the purpose of determining whether adhesive interactions correlate to the known compatibility of each pair for processing into nanocomposites.

In the initial experiments of the study, a colloidal probe was coated with the OMMT Cloisite® 20A, and a flat substrate was coated with the polymer poly(methyl methacrylate) (PMMA). Force/distance curves were obtained with the probe and substrate on an AFM. The curves could be repeated at the same location or in different locations on the PMMA coating. An average normalized adhesive force of -25 mN/m was calculated from the force/distance curves. In contrast, force/distance curves obtained with the opposite configuration – a colloidal probe coated with PMMA and a flat substrate coated with Cloisite® 20A – produced force/distance curves with significant scatter. The curves could not be repeated at the same or in different locations on the Cloisite® 20A coating. The scatter was attributed to the inability of a relatively thin

coating of PMMA on the probe to conform sufficiently to the relatively stiff and rough Cloisite® 20A coating on the substrate. An average normalized adhesive force was not calculated. For measuring adhesive force between an OMMT and polymer, placement of the OMMT on the colloidal probe and placement of the polymer on the flat substrate is the preferred configuration.

With regard to polymer coatings on substrates, it was found that coatings of PMMA and polyethylene-*graft*-maleic anhydride (PE-MA) with one nanometer roughness (determined by the root mean square (rms) method) were associated with a low amount of scatter in the measured interactions. In contrast, force/distance curves obtained with a PE-MA coating with 27 nm rms roughness varied considerably. Polymer coatings with low roughness appear to be a prerequisite for obtaining repeatable force/distance curves.

Force/distance curves obtained with a colloidal probe dip-coated in a Cloisite® 25A dispersion and a substrate coated with PMMA had a median normalized adhesive force of -170 mN/m – considerably higher than the -25 mN/m value obtained with a colloidal probe coated with Cloisite® 20A and a substrate coated with PMMA, and more than double the -65 mN/m value reported by Szücs *et al.* for a colloidal probe coated with a montmorillonite and a silicon wafer coated with polydiallyldimethylammonium chloride (PDDACl) [27]. An atomic-force-microscope scan performed on the colloidal probe showed evidence of a smooth coating of Cloisite® 25A. In contrast, the probe that was coated with Cloisite® 20A showed evidence of an asperity; an asperity can

significantly reduce the contact area between a probe and a substrate, resulting in reduced interaction.

Force/distance curves were obtained with a colloidal probe silane-treated with 3-(2,3-epoxypropoxy)propyltrimethoxysilane (EPPMS) and a substrate coated with PMMA. The median normalized adhesive force of -328 mN/m was calculated from the curves. The Johnson-Kendall-Roberts (JKR) model, which is applicable to the colloidal probe technique with elastic materials such as polymers, was used with reported surface energies of PMMA and cured EPPMS to calculate a normalized adhesive force; the value was -384 mN/m. The similarity in the experimental value and theoretical value lent credibility to the technique that was used to measure adhesive force between EPPMS and PMMA. It also lent credibility to the normalized adhesive force value of -170 mN/m measured between Cloisite® 25A and PMMA.



## REFERENCES

1. L. Betega de Paiva, A.R. Morales and T.R. Guimarães, “*Structural and Optical Properties of Polypropylene-Montmorillonite Nanocomposites*,” *Mat Sci Eng A-Struct*, **447**, 261-265 (2007).
2. E. Manius, A. Touny, L. Wu, K. Strawhecker, B. Lu and T.C. Chung, “*Polypropylene/Montmorillonite Nanocomposites. Review of the Synthetic Routes and Materials Properties*,” *Chem. Mater.*, **13**, 3516-3523 (2001).
3. Rossi, L. (2000). *Principia Partners Estimates 1 billion lb Demand Worldwide for Nanocomposite Over Next Decade* [Online]. Available at [http://www.principiaconsulting.com/publishing/PDF/brochure\\_nano.pdf](http://www.principiaconsulting.com/publishing/PDF/brochure_nano.pdf) (accessed 12 October 2007). Posted pdf file.
4. BCC Research (2006). *Nanocomposites, Nanoparticles, Nanoclays, and Nanotubes, Report Highlights* [Online]. Available at <http://marketresearch.com/product/display.asp?productid=1331812&g=1> (accessed 11 September 2007). WWW article.
5. N. Noda, Y. Lee, A.J. Bur, V.M. Prabhu, C.R. Snyder, S.C. Roth and M. McBrearty, “*Dielectric Properties of Nylon 6/Clay Nanocomposites from On-line Process Monitoring and Off-line Measurements*,” *Polymer*, **46**, 7201-7217 (2005).
6. W.D. Callister, Jr., *Materials Science and Engineering, An Introduction*, 7<sup>th</sup> ed. (John Wiley and Sons, Inc., New York, 2007), p. 429.
7. W.E. Worrall, *Clays and Ceramic Raw Materials*, 2nd ed. (Elsevier Applied Science Publishers, London and New York, 1986), pp. 29-39.
8. J.H. Park and S.C. Jana, “*Mechanism of Exfoliation of Nanoclay Particles in Epoxy-Clay Nanocomposites*,” *Macromolecules*, **36**, 2758-2768 (2003).
9. R. Chung, San Jose State University, *private communication (November 4, 2003)*.
10. H.D. Wagner and R.A. Vaia, “*Nanocomposites: Issues at the Interface*,” *Materials Today*, **7**, 38-42 (2004).
11. G.M. Kim, D.H. Lee, B. Hoffman, J. Kressler and G. Stöppelmann, “*Influence of Nanofillers on the Deformation Process in Layered Silicate/Polyamide-12 Nanocomposites*,” *Polymer*, **42**, 1095-1100 (2001).

12. H. Shi, T. Lan and T. Pinnavaia, "*Interfacial Effects on the Reinforcement Properties of Polymer-Organoclay Nanocomposites*," Chem. Mater., **8**, 1584-1587 (1996).
13. S.K. Lim, J.W. Kim, I. Chin, K. Kwon and H.J. Choi, "*Preparation and Intercalation Characteristics of Organically Modified Montmorillonite Nanocomposite with Miscible Polymer Blend of Poly(Ethylene Oxide) and Poly(Methyl Methacrylate)*" Chem. Mater., **14**, 1989-1994 (2002).
14. L.S. Loo and K.K. Gleason, "*Fourier Transform Infrared Investigation of the Deformation Behavior of Montmorillonite in Nylon-6/Nanoclay Nanocomposite*," Macromolecules, **36**, 2587-2590 (2003).
15. A. Usuki, A. Koiwai, Y. Kojima and M. Kawasumi, A. Okada, T. Karauchi and O. Kamigaito, "*Interaction of Nylon 6-Clay Surface and Mechanical Properties of Nylon 6-Clay Hybrid*," J Appl Polym Sci, **55**, 119-123 (1995).
16. Z. Wang and T.J. Pinnavaia, "*Hybrid Organic-Inorganic Nanocomposites: Exfoliation of Magadiite Nanolayers in an Elastomeric Epoxy Polymer*," Chem. Mater., **10**, 1820-1826 (1998).
17. T. Lan, P.D. Kaviratna and T.J. Pinnavaia, "*Epoxy Self-Polymerization in Smectite Clays*," J. Phys. Chem Solids, **57**, 1105-1010, (1996)
18. T.G. Gopakumar, J.A. Kontopoulou and J.S. Parent, "*Influence of Clay Exfoliation on the Physical Properties of Montmorillonite/Polyethylene Composites*," Polymer, **43**, 5483-5491 (2002).
19. G. Tanaka and L.A. Goettler, "*Predicting the Binding Energy for Nylon 6,6/Clay Nanocomposite by Molecular Modeling*," Polymer, **43**, 541-553 (2002).
20. M. Fermeglia, M. Ferrone and S. Pricl, "*Computer Simulation of Nylon-6/Organoclay Nanocomposites: Prediction of Binding Energy*," Fluid Phase Equilib, **212**, 315-329 (2003).
21. Southern Clay Products, Inc. (2007). *Cloisite® Selection Chart Based on Polymer/Monomer Chemistry* [Online]. Available at [http://www.nanoclay.com/selection\\_chart.asp](http://www.nanoclay.com/selection_chart.asp) (accessed 12 October 2007). WWW page.
22. R.A. Vaia and E.P. Giannelis, "*Lattice Model of Polymer Melt Intercalation in Organically-Modified Layered Silicates*," Macromolecules, **30**, 7990-7999 (1997).
23. L.A. Goettler, B.A. Lysek and C.E. Powell, Published PCT Patent Application W/O 99/41299 (19 August 1999), pp 51-52.

24. D.L. VanderHart and A. Asano, "NMR Measurements Related to Clay-Dispersion Quality and Organic-Modifier Stability in Nylon-6/Clay Nanocomposites," *Macromolecules*, **34**, 3819-3822 (2001).
25. R.D. Davis, J.W. Gilman and D.L VanderHart. "Processing Degradation of Polyamide 6/Montmorillonite Clay Nanocomposite and Clay Organic Modifier," *Polym Degrad Stabil*, **79**, 111-121 (2003).
26. R.H. Yoon, D.H. Flinn and Y.I. Rabinovich, "Hydrophobic Interactions between Dissimilar Surfaces," *J Colloid Interface Sci.*, **185**, 363-370 (1997).
27. A. Szücs, T. Haraszti, I. Dékány and J.H. Fendler, "Measurements of Interaction Forces between Polycations, between Clay Nanoplatelets, and between Polycations and Clay Nanoplatelets by Atomic Force Microscopy," *J. Phys. Chem. B*, **105**, 10579-10587 (2001).
28. D.L. Ho and C.J. Glinka, "Effects of Solvent Solubility Parameters on Organoclay Dispersions," *Chem. Mater.*, **15**, 1309-1312 (2003).
29. C.H. Lee, S.T. Lim, Y.H. Hyun, H.J. Choi, and J.S. Jhon, "Fabrication and Viscoelastic Properties of Biodegradable Polymer/Organophilic Clay Nanocomposites," *J of Mater Sci Lett*, **22**, 53-55 (2003).
30. J. Chang, Y.U. An and G.S. Sur, "Poly(lactic acid) Nanocomposites with Various Organoclays. I. Thermomechanical Properties, Morphology, and Gas Permeability." *J Polym Sci Pol Phys*, **41**, 94-103 (2003).
31. A. Bansal, H. Yang, C. Li, K. Cho, B.C. Benicewicz, S.K. Kumar and L.S. Schadler, "Quantitative Equivalence Between Polymer Nanocomposites and Thin Polymer Films," *Nat Mater*, **4**, 693-698 (2005).
32. A.S. Huguet and E. Barthel, "Surface Forces and the Adhesive Contact of Axisymmetric Elastic Bodies," in *Particle Adhesion: Applications and Advances*, edited by D.J Quesnel, D.S. Rimai and L.H. Sharpe (Taylor and Francis, New York, 2001) pp. 143-175.
33. M. Reitsma, S. Biggs and V.S.J. Craig, "Measurement of the Adhesion of a Viscoelastic Sphere to a Flat Non-Compliant Substrate," in *Particle Adhesion: Applications and Advances*, edited by D.J Quesnel, D.S. Rimai and L.H. Sharpe (Taylor and Francis, New York, 2001) pp. 125-142).
34. M. Kappl and H. Butt, "The Colloidal Probe Technique and its Application to Adhesion Force Measurements," *Part Part Syst Char*, **33**, 129-143 (2002).

35. S. Lee and M. Elimelech, "Relating Organic Fouling of Reverse Osmosis Membranes to Intermolecular Adhesion Forces," *Environ Sci Technol*, **40**, 980-987 (2006).
36. P.M. Young, M.J. Tobyn, R. Price, M. Buttrum and F. Dey, "The Use of Colloid Probe Microscopy to Predict Aerosilization Performance in Dry Powder Inhalers: AFM and In Vitro Correlation," *J Pharm Sci-US*, **95**, 1800-1809 (2006).
37. Southern Clay Products, Inc. (2007). *Product Selection* [Online]. Available at [http://www.nanoclay.com/selection\\_chart.asp](http://www.nanoclay.com/selection_chart.asp) (accessed 12 October 2007). Links to posted pdf files.
38. C.M. Koo, H.T. Ham, S.O. Kim, K.H. Wang and I.J. Chung, "Morphology Evolution and Anisotropic Phase Formation of the Maleated Polyethylene-Layered Silicate Nanocomposites," *Macromolecules*, **35**, 5116-5122 (2002).
39. S. Simper, Southern Clay Products, Inc., *private communication* (November 2003).
40. P. West and A. Ross, An Introduction to Atomic Force Microscopy Modes (Pacific Nanotechnology, Inc., Santa Clara, CA, 2006), p. 1.
41. Nano-R™ AFM User's Manual, revision 1.1 (Pacific Nanotechnology, Inc., Santa Clara, CA, 2004), p. 3.
42. Nano-R™ AFM User's Manual, revision 1.1 (Pacific Nanotechnology, Inc., Santa Clara, CA, 2004), p. 20.
43. Nano-R™ AFM User's Manual, revision 1.1 (Pacific Nanotechnology, Inc., Santa Clara, CA, 2004), p. 4.
44. C. Nieto and V.S.J. Craig, "Colloid Probe Characterization: Radius and Roughness Determination," *Langmuir*, **17**, 2097-2099 (2001).
45. L.O. Heim, M. Kappl and H.J. Butt, "Tilt of Atomic Force Microscope Cantilevers: Effect on Spring Constant and Adhesion Measurements," *Langmuir*, **20**, 2760-2764 (2004).
46. B. Arkles and G. Larson, eds., Silicon Compounds: Silanes & Silicones, (Gelest, Inc., Morrisville, PA, 2004), p. 173.
47. J.A. Dean, Lange's Handbook of Chemistry, 14<sup>th</sup> ed. (McGraw-Hill, Inc., New York, 1992), p. 5-97.
48. M-Pyrol® N-methyl-2-Pyrrolidone, (GAF Corporation, New York, 1972), p. 5.

49. Smithsonian/NASA ADS Physics Abstract Service (2004). *Investigation of Polymer Film Spin Casting: Solvent Properties that Create Optimal Film Quality and Use of Selective Solvents for Multilayered Films* [Online]. Available at <http://absabs.harvard.edu/abs/2004APS..MAR.R1020E> (accessed 19 November 2006). WWW page.
50. R.C. Weast, M.J Astle and W.H. Beyer, ed., CRC Handbook of Chemistry and Physics, 69<sup>th</sup> ed. (CRC Press, Boca Raton, Florida, 1988), p. C-406.
51. R.C. Weast, M.J Astle and W.H. Beyer, eds., CRC Handbook of Chemistry and Physics, 69<sup>th</sup> ed. (CRC Press, Boca Raton, Florida, 1988), p. C-267.
52. R.C. Weast, M.J Astle and W.H. Beyer, eds., CRC Handbook of Chemistry and Physics, 69<sup>th</sup> ed. (CRC Press, Boca Raton, Florida, 1988), p. C-518.
53. R.C. Weast, M.J Astle and W.H. Beyer, eds., CRC Handbook of Chemistry and Physics, 69<sup>th</sup> ed. (CRC Press, Boca Raton, Florida, 1988), p. C-529.
54. R.C. Weast, M.J Astle and W.H. Beyer, eds., CRC Handbook of Chemistry and Physics, 69<sup>th</sup> ed. (CRC Press, Boca Raton, Florida, 1988), p. C-224.
55. W.J. Roff, J.R. Scott and J. Pacitti, eds., Handbook of Common Polymers (CRC Press, Cleveland, Ohio, 1971), pp 216-217.
56. L. Sirghi, O. Kylián, D. Gilliland, G. Ceccone and F. Rossi, “*Cleaning and Hydrophilization of Atomic Force Microscopy Silicon Probes*,” *J. Phys. Chem. B*, **110(51)**, 25975-25981 (2006).
57. J. Drelich, “*Adhesion Forces Measured between Particles and Substrates with Nano-Roughness*,” *Miner Metall Proc*, **23**, 226-232 (2006).
58. J. Brandrup and E.H. Immergut, eds., Polymer Handbook, 2<sup>nd</sup> ed. (John Wiley & Sons, New York, 1975), p. III-222.

APPENDIX A  
MODIFIED SWELLING TEST RESULTS ON CLOISITE® 30B

Cloisite® 30B in the amount of 0.02 grams was placed in Kimble Solvent Saver® scintillation vials. One milliliter of solvent was added to each vial. The vials were closed and allowed to stand overnight. The vertical thickness of the swelled Cloisite® 30B at the bottom of each vial was estimated the next day.

Solvent	Swelled Thickness of Cloisite® 30B in Millimeters
1,1,2-Trichloroethylene	2.0
1,1,1-Trichloroethane	3.2
Acetone	2.7
Chloroform	2.8
1,1,2-Trichloroethane	2.3
Dichloromethane	3.7
Methyl Ethyl Ketone	3.3
Acetamide	3.0
Tetrahydrofuran	3.4
1,4-Dioxane	2.1
1,2-Dichloroethane	3.6
Phenol	2.1
Butyl cellosolve	2.7
Tetrachloroethylene	2.2
N-methyl-2-pyrrolidone	4.5
2,2,2-Trifluoroethanol	2.2
Pyridine	3.5
N-butanol	2.0
Dimethylacetamide	5.5
Furfuryl alcohol	2.0
Methyl acetate	3.3
1-Pentanol	2.0
3-Methyl-1-butanol	1.8
Dimethylsulfoxide	2.5
Toluene	2.2